

University of Alberta

**Stress-Free Ultra-Hard NEMS Cantilevers Fabricated from
Atomically-Smooth Ni-Mo Nanocomposite Thin Films**

by



Reza Mohammadi

A thesis submitted to the Faculty of Graduate Studies and Research
in partial fulfillment of the requirements for the degree of

Doctor of Philosophy

Department of Mechanical Engineering

**Edmonton, Alberta
Spring 2008**



Library and
Archives Canada

Published Heritage
Branch

395 Wellington Street
Ottawa ON K1A 0N4
Canada

Bibliothèque et
Archives Canada

Direction du
Patrimoine de l'édition

395, rue Wellington
Ottawa ON K1A 0N4
Canada

Your file *Votre référence*
ISBN: 978-0-494-45569-2
Our file *Notre référence*
ISBN: 978-0-494-45569-2

NOTICE:

The author has granted a non-exclusive license allowing Library and Archives Canada to reproduce, publish, archive, preserve, conserve, communicate to the public by telecommunication or on the Internet, loan, distribute and sell theses worldwide, for commercial or non-commercial purposes, in microform, paper, electronic and/or any other formats.

The author retains copyright ownership and moral rights in this thesis. Neither the thesis nor substantial extracts from it may be printed or otherwise reproduced without the author's permission.

AVIS:

L'auteur a accordé une licence non exclusive permettant à la Bibliothèque et Archives Canada de reproduire, publier, archiver, sauvegarder, conserver, transmettre au public par télécommunication ou par l'Internet, prêter, distribuer et vendre des thèses partout dans le monde, à des fins commerciales ou autres, sur support microforme, papier, électronique et/ou autres formats.

L'auteur conserve la propriété du droit d'auteur et des droits moraux qui protègent cette thèse. Ni la thèse ni des extraits substantiels de celle-ci ne doivent être imprimés ou autrement reproduits sans son autorisation.

In compliance with the Canadian Privacy Act some supporting forms may have been removed from this thesis.

Conformément à la loi canadienne sur la protection de la vie privée, quelques formulaires secondaires ont été enlevés de cette thèse.

While these forms may be included in the document page count, their removal does not represent any loss of content from the thesis.

Bien que ces formulaires aient inclus dans la pagination, il n'y aura aucun contenu manquant.

■*■
Canada

Abstract

The objective of this study was to design a microstructure that was metallic, atomically smooth, strong, stable at elevated temperatures and stress free. We picked nickel-molybdenum (Ni-Mo) and performed a systematic study of microstructure and properties of 1 μm thick films as a function of composition by using room temperature co-sputtering. This investigation resulted in an optimum film composition of Ni-44at.%Mo, with a unique nanocomposite microstructure of Mo-rich nanocrystallites randomly and densely dispersed in a Ni-rich amorphous matrix. This stress-free film showed a very high nanoindentation hardness of 11 GPa and an order of magnitude reduction in surface roughness (0.8 nm) compared to those of pure Ni (4.5 GPa and 10 nm) and pure Mo (7.5 GPa and 8 nm), while maintaining the resistivity in metallic range. The alloy is also stable at high temperatures of the order of 400°C. As a further step, we conducted a detailed study on the prediction of the composition range of amorphous formation according to the different existing models. Among these models, we found that the prediction range of Miedema's thermodynamic model of Ni-38at.%Mo to Ni-68at.%Mo was in a good agreement with the amorphous range obtained from our experimental data. As a proof-of-principle, we synthesized free-standing single-anchored cantilevers from Ni-44at.%Mo film that were 50 nm thick, 400 nm wide and ranged in length from 1-6 μm . The synthesized cantilevers have the potential to be used as sensors in atomic force microscopy, petroleum industry, microfluidics and biomedical chips, and generally wherever operations at elevated temperature and good conductivity are required.

Dedication

Dedicated with deepest divine thankfulness to my wife-the queen of my heart, Laleh,
dearest of my loving heart always.

And to my lovely parents and family for all their support and love over the years.

Acknowledgements

The support of the microscopy unit of the Lawrence Berkeley National Laboratory, especially Dr. Zonghoon Lee (for performing the nanoindentation test and preparing the TEM samples) and Dr. Velimir Radmilovic (for performing the TEM) is highly acknowledged. Also, we would like to thank Dr. Stephane Evoy's group, especially Mr. Nathan Nelson-Fitzpatrick, for their kind help with the fabrication of the cantilevers. The support of the National Institute for Nanotechnology (NINT) and the co-members of my research group: Mr. Babak Shalchi (for helping with DSC), Brian Olsen (helping with AFM experiments), Chris Gilkison (cleaning the wafers), Chris Harrower (for doing the AFM tests), Chris Holt, Colin Ophus (for helping with sputtering, TEM, XRD and measuring the physical properties), Erik Lubber (for helping with TEM), Jian Chen, Julian Haagsma (cleaning the wafers), Michael Brougham, Mohsen Danaie (helping with DSC) and Sean Murphy (for helping with XPS) is acknowledged as well. Also, I would like to sincerely thank my supervisors, Dr. Dave Mitlin and Dr. Larry Kostiuik for their kind pieces of advice on this project. My special and sincere thanks go to my dearest wife, Laleh, for all her support and help during this project. At the end, I would like to acknowledge the support of the administration and technical staff of the Department of Mechanical Engineering at the University of Alberta.

Table of Contents

CHAPTER ONE: INTRODUCTION	1
1.1 Overall Structure of the Thesis	4
CHAPTER TWO: THIN FILM GROWTH AND STRESSES	8
2.1 Thin Films Growth.....	8
2.1.1 Growth in Polycrystalline Thin Films	8
2.1.2 Growth in Amorphous Thin Films	11
2.2 Origins of Thin Film Stresses	13
2.2.1 Origin of Intrinsic Stresses in Polycrystalline Films	15
2.2.1.1 Intrinsic Stress Generation before Islands Coalescence	16
2.2.1.2 Intrinsic Stress Generation during Islands Coalescence	17
2.2.1.3 Intrinsic Stress Generation after Islands Coalescence	18
2.2.2 Origin of Intrinsic Stresses in Amorphous Films	21
2.3 Strengthening Mechanisms in Crystalline and Amorphous Materials.....	22
2.3.1 Strengthening Mechanisms in Crystalline Materials.....	23
2.3.1.1 Strengthening from Grain Boundaries	23
2.3.1.2 Solid Solution Hardening	24
2.3.1.3 Strengthening from Fine Particles.....	24
2.3.2 Mechanical Behaviour of Amorphous Materials.....	26
2.3.3 Motivation for Having Nanostructured Amorphous Materials	27
CHAPTER THREE: AMORPHIZATION CRITERIA.....	35
3.1 Atomic Size Ratio	36
3.2 Atomic Size Effect and Enthalpy of Mixing.....	36
3.3 Temperature-Composition (T-C) Model.....	37
3.4 A Thermodynamic Model.....	39
3.4.1 Free Energy of Solid Solutions.....	39
3.4.1.1 The Chemical Contribution.....	40
3.4.1.2 The Elastic Contribution	41
3.4.1.3 The Structural Contribution	42
3.4.2 Free Energy of Amorphous Phase	43
3.4.3 Free Energy of Intermetallics	44
CHAPTER FOUR: EXPERIMENTAL PROCEDURE	48
4.1 Fabrication of the Films	48
4.2 Material Characterization of the Films	49
4.3 Measurement of Physical Properties.....	51
4.4 Fabrication of Cantilevers.....	52
CHAPTER FIVE: RESULTS AND DISCUSSION.....	54
5.1 Prediction of the Composition Range of Amorphous Phase.....	54
5.2 Material Characterization of the Films	56

5.3 Physical Properties of the Films.....	62
5.4 Synthesized Cantilevers	66
CHAPTER SIX: CONCLUSIONS AND RECOMMENDATIONS.....	91
6.1 Summary and Conclusions.....	91
6.2 Future Work	92
APPENDIX A: APPLICATION AND COMMERCIALIZATION PLAN	95
A.1. Measurement of Liquid Properties Using the Cantilevers	95
A.1.1. Theory	100
A.2. Cost Estimate of Cantilever's Fabrication	104
REFERENCES.....	107

List of Tables

Table 4.1: Energy dispersive x-ray spectroscopy (EDS) results for the full range of composition of Ni-Mo films from pure Ni to pure Mo together with the Ni/Mo atomic ratios	50
Table 5.1: Calculated values for minimum concentration of solute, at which the amorphous formation begins in Ni-Mo system according to the atomic size model [14]	54
Table 5.2: The calculated values of x_{er} and T_{lr} for Ni-Mo system (Section 2.3) according to the temperature-composition (T-C) model.....	55
Table 5.3: The parameters used to model the formation range of metastable phases in Ni-Mo according to the Miedema's approach [14].....	56
Table 5.4: Predicted range of amorphous phase for Ni-Mo calculated using different models discussed in Chapter One (Chapter B). The experimental result of this study has been shown as well for comparison purposes.	59
Table 5.5: Oxygen content of the surface of pure Ni, Ni-44at.%Mo and pure Mo films. The concentrations are in atomic percent.	62
Table A.1: The details of cost estimate for the fabrication of a Ni-Mo single cantilever. If a stack of cantilevers is needed, the total cost should be considered. The analysis is based on the charge rates for industries. The prices are in Canadian Dollar.....	105

List of Figures and Illustrations

- Figure 1.1: Equilibrium phase diagram of Ni-Mo, based on [18, 19]. Different phases present at different temperatures are shown. Several intermetallics are available in Ni-Mo binary alloy due to the relatively high heat of mixing between these two elements. It is, therefore, supposed to see a large range of amorphous phase of this alloy under non-equilibrium conditions. 7
- Figure 2.1: Schematic of three basic modes of thin film growth, based on [1]. Island (Volmer-Weber) growth, layer (Frank-van der Merwe) growth and mixed (Stranski-Krastanov) growth. 28
- Figure 2.2: Young's equation for the wetting of a surface, based on [33, 34]. This equation relates liquid-vapour (γ_{lv}), vapour-solid (γ_{vp}) and liquid-solid (γ_{ls}) interfacial energies in terms of wetting angle (θ) as $\gamma_{sv} = \gamma_{sl} + \gamma_{lv} \cos \theta$ 28
- Figure 2.3: The competitive grain growth starting from randomly oriented nuclei on the substrate (bottom line) is shown (based on [40]). The grains that their fastest-growing orientation is normal to the substrate, overgrow other grains and win the competition. 29
- Figure 2.4: (a) Schematic illustration of stress versus thickness plot for a metal with relatively low adatom mobility. Three stages of stress can be observed in the growth of these materials: compressive stresses before coalescence, changing in the sign of stress during coalescence and the tensile stresses after coalescence. (b) Schematic illustration of stress versus thickness plot for a metal with relatively high adatom mobility. There is a three-stage stress evolution in the growth of these films too: compressive stresses before coalescence, a change in sign of stress during coalescence and compressive stresses after coalescence (based on [57]). 30
- Figure 2.5: Schematic illustration of the Nix zipping mechanism, based on [35, 36], at coalescence of the islands. This mechanism explains the origin of the tensile stresses developing in thin film growth. When the isolated islands grow (top schematic), they contact each other at the top (middle schematic) and suddenly snap together (the bottom schematic) due to the tendency to reduce the surface energy. The sign of the intrinsic stress in the film changes, then, from compressive to tensile as a result of the substrate constraint. 31
- Figure 2.6: Schematic of the model for the flow of the atoms into the grain boundaries during the film growth due to the chemical potential gradient. Addition of atoms to the grain boundary results in the relaxation of tensile stresses and compressive stresses develop (based on [64]). 32

Figure 2.7: Evolution of substrate curvature and roughness with film thickness for amorphous Zr-Al-Cu films. A three-stage development of stresses is observed in the amorphous film growth: a very thin tensile stress regime, a compressive stress regime and the last tensile stress regime. A convention of positive curvature for compressive stress has been used here (based on [51]).	33
Figure 2.8: Model for the tensile stress generation due to the dynamic coalescence of the columns. This results in energy minimization, based on [51].	34
Figure 3.1: Hypothetical phase diagram with a eutectic surrounded by a solid solution region and an intermetallic compound, based on [85].	46
Figure 3.2: The structural stability $E(Z)$ of paramagnetic transition metals for the BCC, FCC and HCP structures as a function of the number of valence electrons per atom, Z (based on [14]).	47
Figure 5.1: The modeled free energy curves of the metastable phases in Ni-Mo obtained using the Miedema's approach. The range of the amorphous formation can be predicted by drawing the tie-lines between the solid solution and amorphous phases showing an amorphous range of Ni-38at.%Mo to Ni-68at.%Mo.	68
Figure 5.2: High-resolution scanning electron microscopy (SEM) images of the films from pure Ni to Ni-23at.%Mo.	69
Figure 5.3: High-resolution scanning electron microscopy (SEM) micrographs of the films from Ni-34at.%Mo to Ni-69at.%Ni.	70
Figure 5.4: High-resolution scanning electron microscopy (SEM) images of the films from Ni-78at.%Mo to pure Mo.	71
Figure 5.5: High-resolution atomic force microscopy (AFM) images of the films from pure Ni to Ni-23at.%Mo. The roughness decreases generally with Mo content. It should be mentioned that the roughness values are for comparison purposes between our fabricated films only; the actual roughness values might be higher than the present RMS values due to the detection limit of the tip.	72
Figure 5.6: High-resolution AFM micrographs of the films from Ni-34at.%Mo to Ni-69at.%Ni. We can see that the surface of the films is very smooth (RMS<1 nm). It should be mentioned that the roughness values are for comparison purposes between our fabricated films only; the actual roughness values might be higher than the present RMS values due to the detection limit of the tip.	73

- Figure 5.7: High-resolution AFM micrographs of the films from Ni-78at.%Mo to pure Mo. It can be observed that the roughness of the films increases generally with increasing of the Mo content. It should be mentioned that the roughness values are for comparison purposes between our fabricated films only; the actual roughness values might be higher than the present RMS values due to the detection limit of the tip. 74
- Figure 5.8: (a) X-ray diffraction (XRD) spectra for the films from pure Ni to Ni-23at.%Mo together with the simulated indices using Desktop Microscopist commercial software, based on powder diffraction patterns (b). We can observe that for this composition range, the structure is fully FCC crystalline. 75
- Figure 5.9: Vegard's law plot for the films from pure Ni to Ni-23at.%Mo. A line can be best fitted to the data showing that the rule of mixture is almost dominant for the data from the Ni peaks in Fig. 3.8. This plot shows the presence of a solid solution having stress for this region..... 76
- Figure 5.10: XRD signals for the middle range of composition from Ni-23at.%Mo to Ni-69at.%Mo. The peak broadening could be due to either amorphous, or nanocrystalline phase or both. The size of possible nanocrystallites was estimated to be from 1.5 nm to 2.5 nm using Sherrer equation. 77
- Figure 5.11: (a) XRD spectra for the films from Ni-78at.%Mo to pure Mo together with the simulated indices, based on powder diffraction patterns (b). We can see for this range of composition that the structure is fully crystalline with a BCC structure. 78
- Figure 5.12: Vegard's law plot for the films from Ni-78at.%Mo to pure Mo. A line can be best fitted to the data showing that the rule of mixture is almost dominant. The difference between two lines can be due to the strain or lattice parameter difference in solid solution and pure elemental form..... 79
- Figure 5.13: Plan-view bright field (a), plan-view dark field (b) and diffraction pattern (c) of the Ni-44at.%Mo film. We can see that the BCC nanocrystallites are distributed in an amorphous matrix..... 80
- Figure 5.14: Cross-sectional dark field image of the Ni-44at.%Mo film. We can see from this image that the nanocrystallites are present and densely distributed through the thickness as well. 81
- Figure 5.15: High resolution dark field TEM images of the Ni-44at.%Mo film at both plan- (a) and cross-sectional (b) views. The nanocrystallites and lattice fringes are shown on the images. 82
- Figure 5.16: Schematic illustration of the results of different models for the prediction of the range of amorphous formation in Ni-Mo. The experimental

range has been shown as well for comparison purposes. It can be seen that the closest prediction model to our experimental results is Miedema's model.	83
Figure 5.17: Schematic illustration of the kinetic effects on the prediction range of amorphous formation for Ni-Mo using Miedema's model. We can see that the two phase regions (light-gray squares) are narrowed (dark-gray squared) and pushed toward the center due to kinetic of sputtering. Also, the intermetallic phases predicted by the model were not kinetically accessible.	84
Figure 5.18: High-angle cross-sectional SEM images of pure Ni (a) and Ni-44at.%Mo (b) films. We can observe the competitive grain growth in pure Ni only.	85
Figure 5.19: Nanoindentation results of Ni-Mo films: (a) nanohardness and (b) reduced modulus. We can see from these graphs that the hardness and modulus of the films are very high for the middle range of composition. Each datapoint is the average of 25 measurements. The lines are just to guide the eyes.	86
Figure 5.20: Physical properties of Ni-Mo films: (a) surface roughness and (b) intrinsic stress. We can see from these graphs that the surface of the films is very smooth and the films are almost free of stress for the middle range of composition (34at.%<Mo<69at.%). Each datapoint is the average of at least 3 measurements and the errorbars are in the size of symbols. The lines are just to guide the eyes.	87
Figure 5.21: Resistivity data for the Ni-Mo films. We can see from the data that the conductivity is lower for the middle range but still in the range for metals. Each datapoint is the average of at least 3 measurements and the errorbars are in the size of symbols. The lines are just to guide the eyes.	88
Figure 5.22: Effect of thickness on the intrinsic stress of Ni-44at.%Mo film. It can be observed that the stress is compressive for all of the thicknesses but showing a trend towards the positive stresses. Each datapoint is the average of at least 5 measurements and the errorbars are in the size of symbols. The line is just to guide the eyes.	88
Figure 5.23: High-angle SEM images of the 50 nm thick Ni-44at.%Mo cantilevers having different lengths (400 nm and 800 nm wide).	89
Figure 5.24: Differential scanning calorimetry (DSC) curve for the Ni-44at.%Mo film. We can see that the film is stable even at high temperatures in the order of 400 °C in argon atmosphere and used scanning rate (10 °C/min).	90

Figure A.1: Isometric projection of a NEMS cantilever of length a , width b , and thickness d illustrating the relative positions of the applied magnetic flux B , the direction of the current i through the coil A and the resulting force F creating a motion in the y plane detected by the Wheatstone bridge B [108]. 106

List of Symbols, Abbreviations and Nomenclature

Symbol	Definition
	Regular Symbols
a_0	Lattice spacing when islands nucleate
a_f	Lattice spacing when islands grow before coalescence
B	Full width at half maximum
C_{min}	Minimum solute concentration
D	Grain diameter
d	Nanocrystallites size
d_c	Crystallite size at coalescence
d_f	Film thickness
d_s	Substrate thickness
E	Young's modulus
f	Resonance frequency/Surface stress
G_A	Free energy of amorphous phase
G_I	Free energy of intermetallic phase
G_{SS}	Free energy of solid solution phase
H_{Ch}	Chemical contribution
H_{El}	Elastic mismatch contribution
H_{mix}	Enthalpy of mixing
H_A	Enthalpy of amorphous phase
H_I	Enthalpy of intermetallic phase
H_{SS}	Enthalpy of solid solution phase
H_{St}	Structural contribution
k	Locking parameter
L	Grain size
r	Atomic radius
R	Substrate curvature/ Dep. flux
S	Entropy of solid solution and amorphous
T	Temperature
T_0	Thickness of surface layer
T_g	Glass transition temperature
T_l	Liquidus temperature
T_{lr}	Reduced liquidus temperature
T_r	Operation temperature
T_{rg}	Reduced glass temperature
T_s	Substrate or deposition temperature
x	Composition
x_{er}	Reduced eutectic concentration
x_s	Minimum hypoeutectic composition

x_s

Minimum hypoeutectic composition

α

Δ

γ

λ

η_f

Θ

ρ_f

ν

σ_0

σ_i

σ_T

ν

AFM

DSC

EDS

Ga

MEMS

Mo

NEMS

Ni

SEM

Si

TEM

TGA

Ti

XPS

XRD

Greek Symbols

Coefficient of thermal expansion

Gap between adjacent crystals

Surface energy/Degree of short-range ordering

X-ray wavelength

Viscosity of fluid

Bragg's angle

Density of fluid

Poisson's ratio/Stress

Yield stress

Friction stress

Thermal stress

Poisson's ratio

Abbreviations

Atomic force microscopy

Differential scanning calorimetry

Energy dispersive x-ray spectroscopy

Gallium

Micro-electro-mechanical systems

Molybdenum

Nano-electro-mechanical systems

Nickel

Scanning electron microscopy

Silicon

Transmission electron microscopy

Thermogravimetry analysis

Titanium

X-ray photoelectron spectroscopy

X-ray diffraction

CHAPTER ONE: INTRODUCTION

Layers of materials with a thickness ranging from a fraction of nanometres to a few micrometers are called thin films. Thin film science and technology play a significant role in the high-tech industries that are involved in microelectronics, communications, optical electronics, coatings of all kinds and energy generation and conservation [1]. Many sophisticated instruments have been developed in the area of micro-electromechanical/nano-electromechanical systems (MEMS/NEMS) using thin films. MEMS/NEMS cantilever devices fabricated from thin film materials are the building block of many hi-tech systems [2] such as force sensing devices [3, 4], mass sensors [5] and separation membranes [6]. Most of the structural components in MEMS/NEMS are commonly fabricated out of single-crystal or poly-crystal silicon, or one of its compounds such as silicon nitride, silicon carbide and silicon oxide, with silicon being by far the most widely used [2, 7-9].

Although silicon is easy to etch, elastically stiff and very hard [10], its low fracture strength, ductility and wear resistance result in low reliability of this material for in-contact moving parts of the structures. Silicon is also poorly suitable for the applications where good electrical conductivity is a fundamental requirement. Therefore, metals have been proposed recently as potential substitutes for silicon and its compounds in MEMS/NEMS device applications since they offer higher electrical conductivity and better ductility [2, 6, 11, 12]. However, a few drawbacks of metal films such as low strength and hardness, high surface roughness and susceptibility to warping due to the intrinsic and thermal-mismatch stresses that develop during the fabrication process have precluded their application as potential substitutes for silicon.

To address the problems that exist with metallic thin films, it is useful to look at the different features of an ideal microstructure first. An ideal microstructure is strong,

hard, elastically stiff, atomically smooth, stress free, stable at elevated temperatures and can be conductive depending on its application. By comparing the characteristics and properties of two possible metallic microstructures, crystalline or amorphous, it is realized that the amorphous phase meets most of the above requirements [13]. To design such a microstructure, there are some certain criteria that have to be fulfilled. When making a bulk binary alloy of two metallic elements, it has been proven empirically that negative heat of mixing [14] and large atomic mismatch [15] between two alloying elements facilitate the formation of amorphous phase at non-equilibrium conditions. In the phase diagram of a binary alloy system, the number of intermetallic phases, which have complex crystal structures and can be formed under equilibrium conditions, is attributed to the heat of mixing of the two constituent elements. The more negative the heat of mixing, the higher the number of intermetallics that can be formed over the full range of composition. Under non-equilibrium conditions, however, as is the case for vapour deposition for instance, the formation of these equilibrium stable phases is kinetically hard to achieve. The atoms of the constituent elements, therefore, will tend to stay close to each other without forming any crystallographic structures and an amorphous phase will form. This is especially true when the percentage of the solute and atomic mismatch between the solute and solvent are relatively high. These two amorphization principles (large negative heat of mixing and large atomic mismatch) will be covered in more details in Chapter 3. An amorphous material with optimum properties, therefore, can be obtained by taking advantage of these two criteria and the sputter deposition, for instance, that makes the equilibrium phases kinetically difficult to access due to high deposition rate. In this way, the grain/columnar growth, which is mostly responsible for high surface roughness and stress gradients in polycrystalline metal thin films [16, 17], is precluded as well.

To obtain the amorphous microstructure, nickel-molybdenum (Ni-Mo) binary alloy system was selected since this alloy fits the amorphization criteria mentioned above. It

can be seen from Fig. 1.1 [18, 19] that Ni-Mo equilibrium phase diagram offers several intermetallic phases, such as NiMo, Ni₃Mo and Ni₄Mo, over the full range of composition. The existence of these intermetallics is due to the negative heat of mixing between Ni and Mo ($\Delta H_{mix(Ni-Mo)} = -7\text{KJ/mole}$ [14, 20]). In addition to the relatively large negative heat of mixing, there is a good atomic mismatch between these two elements ($r_{Ni}=1.28 \text{ \AA}$ and $r_{Mo}=1.39 \text{ \AA}$) [15]). Another reason for choosing Ni-Mo was the higher strength and hardness of pure Ni and Mo (refractory metal) compared to most of the metallic elements [21]. Therefore, we expect to see better mechanical properties from Ni-Mo compared to other available binary metallic systems that have been developed so far [2]. Also, these two elements are inexpensive and have been used quite extensively in micro/nanofabrication [2, 22-24].

Previous studies on Ni-Mo have been mainly focused on the electrocatalytic behaviour of this material, in both ball-milled and sputter-deposited conditions, for hydrogen evolution [25-28]. Binary Ni-Mo alloy coatings with good adhesion to nickel substrate have been prepared by sputter-deposition method [27]. The electrodes of this material, with the optimum composition of 10 at.% Mo, have been found to be active hydrogen evolution electrocatalyst in 1 M NaOH solution at 30 °C. The Ni-Mo alloy electrodes prepared by this method have shown an activity even higher than that of smooth platinum electrodes. Also, nanocrystalline metastable Ni-Mo solid solutions have been fabricated by high-energy mechanical alloying for the application of hydrogen evolution [26, 29]. This alloy can be formed by mechanically alloying of pure Ni and Mo elemental powders up to about 27wt.%Mo. If the average Mo content exceeds this limit, an amorphous phase is formed. The electroactive phase for the hydrogen evolution reaction in alkaline solutions has been found to be the nanocrystalline structure that must be prepared in an oxygen partial pressure in order to be active. Another branch of research on Ni-Mo has been focused on the possibility of amorphization in multilayers of pure Ni and pure Mo thin films prepared by ion-beam-

assisted deposition (IBAD) [30]. It has been shown that IBAD is a non-equilibrium process and, therefore, phase formation and evolution in this process is affected by the mobility of atoms. Ion-beam mixing (IBM) process has also been used to prepare Ni-Mo multilayer films. These films have shown an increased microhardness compared to pure Ni [31].

1.1 Overall Structure of the Thesis

The current chapter (Chapter 1) of the thesis outlines a background on MEMS/NEMS devices and use of thin films (especially silicon) in these devices, applications of metals for MEMS/NEMS, the problems with metal thin films, what an ideal microstructure is, how it can be designed, why we have used Ni-Mo, how this binary system fits all the criteria and what has been done in the past on the thin films of this binary alloy. Then, the different mechanisms of thin film growth and origins of both tensile and compressive stresses in polycrystalline and amorphous thin films will be studied in Chapter 2. The mechanical behaviour of thin films (crystalline, amorphous, and nanocomposite) and different strengthening mechanisms will be covered in details in the last section of this chapter. In Chapter 3, an extensively review will be provided of the different models proposed for the prediction of the range of amorphous phase formation: the atomic size ratio, enthalpy of mixing effect, relation with phase diagrams and eventually the most comprehensive model, the Miedema's approach.

Chapter 4 introduces the experimental procedure that was followed in this study. The deposition process for the fabrication of the films is considered first and then discussion regarding the different techniques employed to characterize the films will be made. These techniques include energy dispersive x-ray spectroscopy (EDS) for composition analysis, scanning electron microscopy (SEM) to image the surface, atomic force microscopy (AFM) to view the topography of the surface and measuring the surface roughness, x-ray diffraction (XRD) and transmission electron microscopy (TEM) for

phase identification, x-ray photoelectron spectroscopy (XPS) for the measurement of the oxygen contents and differential scanning calorimetry (DSC) for thermal stability testing of the films. Measurement methods of the physical properties of the films will be subsequently reviewed. These methods were used to measure the stress, hardness, modulus, surface roughness and conductivity of the films. The last section of Chapter 4 introduces the details of the fabrication of the cantilevers.

Chapter 5 is dedicated to the results and discussion. The composition range of amorphous formation is predicted first for Ni-Mo according to different existing models. Then, the characterization results including the SEM micrographs, AFM images, XRD spectra and TEM images will be presented and discussed. Next, a comparison will be made between the different models that are used to predict the range of amorphous phase formation in Ni-Mo. A discussion will be provided on why the most accurate and comprehensive one, the Miedema's semi-empirical model, predicts the experimental results the best. Emphasis will be changed then to look at the different measured physical properties of the films. The results of stress measurements, nanoindentation, surface roughness and conductivity of the films will be brought to the reader's attention and discussed. The effect of thickness on stress will be investigated next. In the last section of Chapter 5, the SEM images of synthesized cantilevers will be shown with a brief discussion on the thermal stability of the alloy.

The last Chapter, Chapter 6, is a summary and conclusions of the thesis, in which some recommendations will be proposed for future work. Finally, in Appendix A of the thesis, the different potential applications of the MEMS/NEMS devices, we fabricated from Ni-Mo nanocomposite thin films, will be discussed. From these applications, we will discuss in details the potential application of our synthesized cantilevers in petroleum industry for density and viscosity measurement in the frame of a

commercialization plan. The cost of fabrication of the cantilevers will be estimated in the last section of this Appendix.

Figures

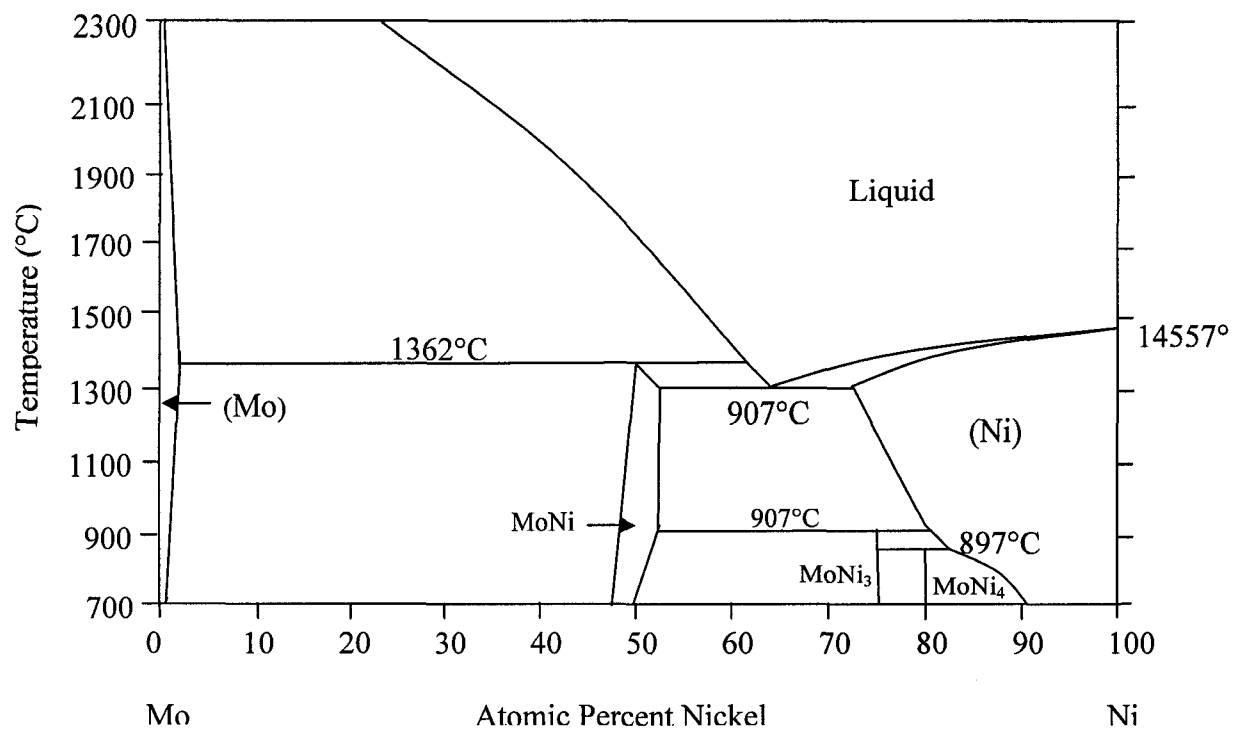


Figure 1.1: Equilibrium phase diagram of Ni-Mo, based on [18, 19]. Different phases present at different temperatures are shown. Several intermetallics are available in Ni-Mo binary alloy due to the relatively high heat of mixing between these two elements. It is, therefore, supposed to see a large range of amorphous phase of this alloy under non-equilibrium conditions.

CHAPTER TWO: THIN FILM GROWTH AND STRESSES

2.1 Thin Films Growth

2.1.1 Growth in Polycrystalline Thin Films

Growth stresses and surface roughness that exist with polycrystalline metallic thin films are the direct results of the conditions under which grain nucleation, growth, coarsening, coalescence and thickening occur. It is well-known that in polycrystalline films, growth techniques and conditions affect the shape, distribution, size and orientation of the grains [32]. An overview of structure evolution in polycrystalline films during deposition is shown in Fig. 2.1 [1]. It is generally accepted that there are three basic modes for thin film growth: (1) island (or Volmer-Weber) growth, (2) layer (or Frank-van der Merwe) growth and (3) mixed (or Stranski-Krastanov) growth. These three modes of growth can be best explained in terms of wetting and Young's equation [33, 34]. This equation relates the wetting of a solid surface to the interfacial energies as

$$\gamma_{sv} = \gamma_{sl} + \gamma_{lv} \cos \theta \quad (2.1)$$

where γ_{sv} , γ_{sl} and γ_{lv} represent solid-vapour, solid-liquid and liquid-vapour interfacial energies, respectively, and θ is the wetting or contact angle (Fig. 2.2). The growth modes are described in more details below considering the above equation.

Island growth happens when the small stable clusters nucleate on the substrate and grow in three dimensions to form islands. This type of growth occurs when the depositing atoms or molecules are more strongly bound to each other than to the substrate. In other words, the clusters of atoms do not wet the substrate and the contact angle in Eq. (2.1) and Fig. 2.2 is high. Deposition of many metallic thin films on insulators, alkali halide crystals, graphite and mica substrates follow this mode of growth. During the layer growth, however, the extension of the smallest stable nucleus

happens in two dimensions leading to the formation of planar layers. In this growth mode, the atoms are more strongly bound to the substrate than to each other and the clusters of atoms wet the surface with low contact angle. The first complete monolayer is then covered by a less tightly bound second layer. The layer growth mode is sustained as long as the decrease in bonding energy is continuous toward the bulk crystal. The most important example of this growth mode is the single-crystal epitaxial growth of semiconductor films. The layer-island or mixed (Stranski-Krastanov) growth mechanism is an intermediate combination of the first two modes, i.e., the layer growth and the island growth. In this case, after forming one or more monolayers subsequent layer growth becomes unfavourable and islands form. The transition from two-dimensional growth to three-dimensional growth has not been completely understood yet, but any factor that changes the wetting characteristics and binding properties of layer growth may be the cause. This growth mode has been observed in metal-metal and metal-semiconductor systems. Since the first growth mode, the island (or Volmer-Weber) growth, is the most common one occurring in thin films, it is discussed in more details below.

Nucleation stage of the film growth occurs when stable clusters of adatoms form and continue to grow. Once formed, the nuclei grow to the external phase as well as laterally in the plane of the interface [32]. The lateral growth results in impingement and coalescence of crystals and formation of grain boundaries, which in turn, defines the grain-structure characteristics of the newly formed film. The size of the Islands at impingement and coalescence is usually around 10 nm or less. It has been shown for island (or Volmer-Weber) growth that the energy per volume released from grain boundary formation during coalescence of islands in the size of 10 nm is sufficiently high enough to drive the development of stresses in the order of GPa in the film [35]. The grain boundary formation at coalescence provides a possible explanation for the high tensile stresses that often develop during the deposition of the materials with low

surface diffusivity [36-38]. Low diffusivity results in small grain size at coalescence and a little stress relief. The requirements for complete stress relief are dislocation generation and motion, diffusional relaxation, surface self-diffusion and sliding at the film-substrate interface [39]. If the surface self-diffusion is low compared to the deposition and coalescence rates, stresses will not be relieved.

Once a continuous film has formed (in Volmer-Weber mode) through nucleation, growth and coalescence, in most applications further thickening of the film is required. The development of grain structure occurs in two different regimes. If the grain boundaries formed through island impingement are mobile, the grain structure of the film develops during the coalescence and continues to evolve during film thickening process. This process often leads to a more equiaxed structure, in which the in-plane grain size is approximately the same as the initial one and scales with the film thickness. The average in-plane grain size is, therefore, uniform through the thickness of the film. If the grain boundaries are immobile, the grain structure resulting from the nucleation, growth and coalescence is retained at the base of the film. Usually, subsequent thickening occurs through epitaxial growth on these grains and columnar structure develops. Often though, as the grains at the base of the film grow, competitive growth leads to an increasing in-plane grain size at the top surface of the thickening film compared to the size at the interface [32]. The competitive grain growth is due to the well-known van der Drift growth mechanism (Fig. 2.3) [40]. This model represents a growth mechanism of continuous polycrystalline films from randomly oriented nuclei. According to the model, the crystallographic texture and the surface morphology of the continuous polycrystalline films resulting from growth competition between the nucleated crystals can be calculated. As the film thickness increases and a continuous film is formed, those crystals having their fastest growth direction perpendicular to the substrate surface will overgrow all other orientations and they represent the orientations of the crystals on the surface. It has been shown, for the case of competitive grain

growth (with immobile grain boundaries), that the surface roughness of thickening films can be increased under the conditions of limited adatom mobility. If adatoms arrive with a range of angles off the normal to the surface, as the case in sputter deposition, shadowing effect can occur [41, 42]. The kinetic roughening and shadowing effect result in competitive growth of columns with the structure similar to that illustrated in Fig. 2.3. In this case, the grain size scales with $t^{1/2}$ [43].

2.1.2 Growth in Amorphous Thin Films

Amorphous metallic alloys have attracted increased scientific interest during recent years. This interest is primarily due to their technologically attractive bulk and surface properties, which are often superior to those obtained from their crystalline counterparts. Wear resistance, strength, hardness, corrosion resistance and surface smoothness are some of those properties [44]. Generally these favourable properties, which can be traced back to the absence of grain boundaries and other defects and lack of long range order, make amorphous thin films also highly promising candidates for refinement of functional surfaces in science and technology. Tailoring the films thus requires a fundamental understanding of the underlying growth mechanisms and their impact on the properties of the film. These mechanisms, in turn, are directly linked to structure formation that depends on the processing parameters during thin film deposition [45].

The understanding of the growth properties of vapour-deposited amorphous thin films and the processing parameters is of increasing interest not only due to its technological importance mentioned above, but also because of its application to surface growth studies [46]. The absence of a structural long-range order with the lack of lattice constraints and the material isotropy enable a simplified data analysis and suggest the study of the effects of different growth mechanisms independent of system details. In

addition, the surface morphology is tightly linked to film stresses, which will be the topic of another section in this chapter.

The surface morphology of amorphous thin films is the result of a balance between the roughening mechanisms due to shadowing or other flux anisotropies of the depositing particles and smoothing due to the surface diffusion [47]. On the microscopic level, these mechanisms are governed by a very complex and only partly-understood interaction between the depositing particles and the already deposited surface atoms. Experiments, on the other hand, exhibit some regularities of the surface morphology (mound-like structure) in amorphous films [48]. This, in turn, indicates that the continuum models can be used for the understanding and interpretation of the growth mechanisms. In particular, amorphous thin film growth represents an attractive system for the validation of such models. This is mainly due to the isotropic nature of the amorphous structure and the lack of long-range ordering [49].

The most systematic and pioneering studies on the growth of amorphous thin films, both experimental and modeling, have been carried out by Samwer and co-workers [44-49]. In the early work done by Reiker *et al.* [50], they studied the surface topography of vapour-quenched amorphous $Zr_{65}Al_{7.5}Cu_{27.5}$ films *in situ* with scanning tunnelling microscopy. They analyzed the development of surface morphology in terms of an increasing film thickness. With film thickness of less than 30 nm, they showed that the surface roughness increases with a growth exponent of approximately 0.2. Above a film thickness of 30 nm, however, they observed a roughening transition at which the surface roughness converges to a maximum value. In addition, they found that surface diffusion is the governing mechanism in the growth of amorphous films at elevated substrate temperatures. They also used a Monte Carlo model for numerical simulation of their results [46]. In another study, Raible *et al.* [49] derived a nonlinear growth equation for the amorphous films and studied the surface roughness of these

films. The most comprehensive model for the growth of amorphous thin films and its relationship with morphology and intrinsic stress has been recently proposed by Samwer and colleagues [51]. In this model, the growth of amorphous phase has been divided into three stages depending on the film thickness. The first stage is attributed to the nucleation and growth of single islands at a very low film thickness. In this regime, the three-dimensional islands nucleate on the substrate and local energy minimization is the dominant mechanism. In the second stage (medium film thicknesses), surface reconstruction will be present and change in surface packing density will be resulted. The driving force for the surface reconstruction is the difference between surface stress and surface energy and is independent of surface morphology. In third stage, local energy minimization is present by viscous coalescence in a dynamic equilibrium of stress generation and surface energy minimization. In this stage, a cluster-like growth is observed due to growth instabilities such as self-shadowing. This rough cluster-like surface is observed in high film thickness regime and the energy can be reduced by processes joining the cusp walls together in this regime.

2.2 Origins of Thin Film Stresses

The stresses in deposited thin films have become one of the most important challenges in the modern technology. The fields of microelectronics, integrated optoelectronics, data storage technologies and micro-electromechanical/nano-electromechanical systems (MEMS/NEMS) all depend critically on the properties, behaviour and reliable performance of thin films. Residual stresses that develop in such films and coatings can lead to film cracking and peeling in the case of tension, and delamination and blistering in the case of compression. Understanding the origins of such stresses and controlling the affecting parameters is, therefore, of great importance to the reliable fabrication of thin films [35].

In general, film stresses are divided into two main categories. One category is growth stresses, which are usually called intrinsic stresses. They are present in films following the growth on the substrate. The second category of film stresses represents those stress conditions that arise from changes in the physical environment of the film material following its growth. Such externally induced stresses are usually called extrinsic stresses [52]. This category of stresses includes thermal and surface stresses. Thermal stresses appear in the films bonded to substrates having different thermal expansion coefficients at a temperature, T_r , higher or lower than the substrate or deposition temperature, T_s . Without any plastic deformation in the film-substrate structure during temperature changes, the thermal stress, σ_T , is directly related to the elastic strain, ε , in the film through Hooke's law [53]:

$$\sigma_T = \left(\frac{E_f}{1-\nu_f} \right) \varepsilon = \left(\frac{E_f}{1-\nu_f} \right) (\alpha_s - \alpha_f)(T_r - T_s) \quad (2.2)$$

where E_f , ν_f and α_f are the Young's modulus, Poisson's ratio and coefficient of thermal expansion of the film, respectively, and α_s is the coefficient of thermal expansion of the substrate.

In addition to thermal stress, another stress term named surface stress can be distinguished in the category of extrinsic stresses. Various molecules can penetrate into the open voids or pores present in not fully-dense films and adsorb to the pore walls. The interaction forces between adsorbed species such as water molecules can cause residual stresses in the film. These stresses, in turn, can deform the film (and devices made out of them) due to the differences in surface energy.

Among the different types of stresses discussed above, the intrinsic stresses are the most important ones. In the following section, therefore, our attention will be focused on these stresses and their origins.

2.2.1 Origin of Intrinsic Stresses in Polycrystalline Films

Stress evolution during the growth of polycrystalline thin films, particularly metallic films on insulating substrates, has been studied experimentally during the past two decades [54]. In these studies, film stress is usually estimated by measuring the curvature of the substrate while depositing the thin film material on it. The change in curvature is then related to an average in-plane stress in the film, σ_f , through the Stoney equation as [1]

$$\sigma_f = \frac{1}{6R} \frac{E_s d_s^2}{(1-\nu_s) d_f} \quad (2.3)$$

where R is the substrate's average curvature, E_s is the Young's modulus of the substrate, ν_s is the Poisson's ratio of the substrate, and d_s and d_f are the thickness of the substrate and film, respectively. In the island growth mode at microscopic scale, the earliest stages of film growth occur through nucleation and growth of individual crystallites on the substrate. As the crystallites grow to a certain size, they start impinging on each other and eventually forming a continuous polycrystalline film [35]. Compressive stresses commonly develop during the early stage of metallic film growth, before the film becomes continuous. This compressive stress can become very large in magnitude. For example, a stress of about -1 GPa was measured in a sputtered Mo film with a nominal thickness of 3.3 nm that was deposited onto the silicon surface. During island coalescence, the intrinsic stress generally displays a very rapid increase that results in the intrinsic stress becoming tensile. If the depositing metal has a low adatom mobility at the deposition temperature, the intrinsic stress generally remains tensile after the coalescence and during the growth as can be seen in Fig. 2.4a [38, 55-57]. These metals are characterized by their high melting temperatures such as Fe, Si, Cr, Ti, etc. If the metal that is deposited has a high adatom mobility at the deposition temperature, the intrinsic stress after coalescence may decrease with further film growth. In many cases, particularly face-centered-cubic (FCC) metals with lower melting temperatures such as Ag, Cu, Al and Au, the stress eventually becomes

compressive (see Fig. 2.4b). A number of physical mechanisms have been proposed so far to describe the different stages of stress evolution behaviour for the two types of materials (low and high adatom mobility), some of which are reviewed below.

2.2.1.1 Intrinsic Stress Generation before Islands Coalescence

The initial compressive stress, when the film is in the form of isolated islands, can be best explained in terms of surface stress effects [57]. Since the nature of the bonding between the atoms at the surface and in the bulk is different in a solid, surface atoms have an equilibrium interatomic spacing different from that of the atoms in the bulk. This difference in equilibrium spacing results in a force per unit length acting on a solid surface, referred to as the surface stress. The surface stress can also be considered as a pressure, called the Laplace pressure, exerting on a finite size solid body equal to the difference between the pressure inside the solid and the pressure of the surrounding vapour. Now if a growing island is considered, the magnitude of the stress within the island can be determined by how strongly it is attached to the substrate. If a very small island is weakly bound to a flat substrate, it will be able to respond to the applied forces by migration and/or changing its structure. One example of such a change in structure is to adjust its lattice spacing in response to volume stresses, such as those that arise from surface stresses. As the island gets larger, it becomes increasingly difficult for it to change its in-plane lattice spacing in response to a change in stress. This is due to the fact that such a change involves an increasingly change in a large number of bonds at the island–substrate interface. Eventually, there will be a critical size at which the island in-plane lattice spacing will be effectively frozen. Since the island is constrained by the substrate, the substrate must impose an in-plane biaxial stress to keep the island from attaining its equilibrium spacing as thickness and diameter of the island increase. As a result, an intrinsic stress is generated in the constrained island due to surface stress effects. If the net surface stress (the summation of surface stress at the top and bottom of the island) is positive, the intrinsic stress will be compressive. Therefore, this

contribution can explain compressive intrinsic stresses often observed during the early stages of polycrystalline metallic film growth (before coalescence).

2.2.1.2 Intrinsic Stress Generation during Islands Coalescence

The mechanism behind the intrinsic stress generation during island coalescence has been successfully explained by Hoffman [36], Nix and Clemens [35], and Freund and Chason [58]. The most well-known mechanism for this stage is called zipping mechanism as illustrated schematically in Fig. 2.5. The growing islands remain separated until the space between them becomes smaller than a critical gap, Δ . At this separation gap, the lateral surfaces of the islands zip together to form a grain boundary as a result of a reduction in surface energy equal to $\gamma_{gb}/2 - \gamma_{sv}$ [36, 57] where γ_{gb} and γ_{sv} are the grain boundary energy and island surface energy, respectively. This reduction in surface energy can drive two neighbouring islands to coalesce at the expense of some elastic deformation due to the constraint of substrate. This mechanism can be used to explain the large increase in the intrinsic stress during coalescence as shown in Figs. 2.4a and 2.4b. The development of these tensile stresses in the early stages of polycrystalline film growth has been confirmed experimentally by many researchers [37, 55, 56, 59, 60]. The amount of the tensile stresses at the coalescence of two adjacent crystals can be calculated using atomic size considerations as [61]

$$\sigma = \frac{E\Delta}{(1-\nu)L} \quad (2.4)$$

where E and ν are the Young's modulus and Poisson's ratio of the film, respectively, and L is the grain size. A recent analysis by Nix and Clemens [35] applied the Griffith criteria for crack extension [62] to the grain boundary junction between two crystallites. This model gave the following expression for the estimation of the average film stress, σ , generated by the surface-energy-driven mechanism as

$$\sigma = [2(2\gamma_{sv} - \gamma_{gb})E(1+\nu)/(1-\nu)d_c]^{1/2} \quad (2.5)$$

where d_c is the diameter of impinging hemispherical islands. Unlike the Hoffman's original model (Eq. 2.4), it is not necessary to use atomic size arguments to estimate the size of the gap at the point of crystallite coalescence in this model [35]. In addition to a change in surface energy, island coalescence leads to a change in surface stress. This change in surface stress will result in an instantaneous change in the intrinsic stress in the film [57]. Although the contribution due to the change in surface stress is significantly smaller than that for the surface-energy-driven mechanism, in cases where the pre-coalescence compressive stress is not too large in magnitude, a change in surface stress at coalescence may lead to a significant contribution that needs to be taken into account in a complete treatment of the problem. It should be noted that once such intrinsic stresses develop in a film, they can be maintained during subsequent growth [63] (Fig. 2.4a).

2.2.1.3 Intrinsic Stress Generation after Islands Coalescence

A physical mechanism for the post-coalescence compressive stresses that can explain the complex experimental observations have been recently proposed based on the following information [64, 65] (i) In the case of metals deposited with relatively low adatom mobility (Fig. 2.4a), when the film becomes continuous and a net tensile intrinsic stress associated with the surface-energy-driven mechanism is generated, the intrinsic stress generally remains tensile during further growth. On the other hand, the tensile intrinsic stress in metals deposited with relatively high adatom mobility (such as deposition at elevated temperatures or of low melting point metals) can significantly decrease after island coalescence. This generated intrinsic stress eventually becomes compressive in some cases (Fig. 2.4b) [54, 57]. This two different behaviour observed for the two types of materials imply that the reduction in tensile stress after coalescence is associated with one or more temperature-dependent relaxation mechanisms. (ii) It has been observed that generation of compressive stress is directly related to deposition flux [60]. The compressive stress is seen in the film only during deposition. When

deposition is stopped, stress is relaxed and when deposition is resumed, film reverses to the pre-interrupt compressive stress state. Such a reversible behaviour suggests that the deposition process provides the driving force for compressive stress generation as a result of ion implantation, introducing the interstitials and shot peening effects. This suggestion is further strengthened by the observation that the development of compressive stress during deposition depends on the growth rate [64]. (iii) Another important clue for the physical origins of the compressive stress comes from the experimental observations of deposited palladium by sputtering [54]. It has been found that when the film is epitaxial with no grain boundaries, the residual stress is tensile (Fig. 2.4a). However, when the sputtering conditions are such that the film is polycrystalline with grain boundaries, the stress evolution shows compressive stresses (Fig. 2.4b). These observations clearly demonstrate the role of grain boundaries in compressive stress generation.

Based on these three experimental observations, a model has been proposed for compressive stress generation in the third stage of stress evolution [64]. According to this model, initially when the system is in thermodynamic equilibrium, the chemical potentials of the free surface and the grain boundaries are the same. During the deposition, however, the free surface is at a non-equilibrium state with a supersaturation of adatoms. Due to the presence of growth flux, therefore, the free surface has an excess chemical potential. By taking the equilibrium chemical potential of the surface to be zero, the excess chemical potential can be treated as the surface chemical potential. The chemical potential of atoms at grain boundaries, on the other hand, is proportional to the normal stress acting on them. When island coalescence is complete, the grain boundaries are under a tensile stress and hence the chemical potential is negative. The higher chemical potential on the surface drives adatoms into the grain boundaries. Addition of extra atoms into the grain boundaries leads to tensile stress relaxation and possibly to compressive stress (Fig. 2.6). This mechanism is reversible. When

deposition is interrupted, the surface chemical potential returns to its lower equilibrium value as there is no adatoms coming to the surface. This results in a reverse situation where the chemical potential on the grain boundaries is higher than that on the free surface. This chemical potential difference drives the atoms from grain boundary onto the free surface and relaxes the grain boundary compressive stress. In this simple model, which is based on the atom exchange between the free surface and the grain boundary, the surface and grain boundary diffusion is neglected. Therefore, a more comprehensive model has been presented for compressive stress evolution by taking grain boundary diffusion into consideration [54]. In this model, however, the surface diffusion has been ignored because of the fact that surface diffusivity is usually much higher than grain boundary diffusivity and, therefore, grain boundary diffusion is expected to be the controlling process in the stress evolution.

The development of intrinsic stress after coalescence can also be explained in terms of surface stress effect [57]. It has been shown that the compressive stress resulting from the surface stress (discussed in previous section) continuously increases in magnitude as the thickness increases. During coalescence, the effect of surface stress is masked by the sudden increase in stress associated with the surface-energy-driven mechanism. If a relaxation occurs after coalescence that significantly relieves the tensile stress generated during island impingement, the contribution from surface stress effects can lead to a compressive stress at large film thicknesses (Fig. 2.4b). It should be noted that when grains grow, there is a reduction in grain boundary area. Since the density of grain boundaries is less than that of the grain, elimination of grain boundaries by grain growth can result in a densification of the film [66]. Therefore, in films that are firmly attached to the substrate, grain growth can result in the generation of a compressive intrinsic stress. Thus, if grain growth occurs, the contribution of this mechanism is of the same order as those for the surface stress and surface-energy-driven mechanisms. The mechanism that is expected to dominate at the different stages of growth depends

on the values of the various thermodynamic and kinetic parameters as well as the critical island size and the grain size at coalescence.

2.2.2 Origin of Intrinsic Stresses in Amorphous Films

Contrary to polycrystalline films, there is no long-range atomic order in amorphous films and the grain boundaries are absent. Therefore, a completely different stress behaviour and mechanism is expected in amorphous films [67]. As was discussed in Section 2.1.2, the thin film growth and stress evolution in amorphous films is generally divided into three stages (Fig. 2.7) [51]: a very thin film tensile region, a compressive regime for medium film thicknesses and tensile stresses for high film thicknesses. An island-type growth is assumed for the growth of amorphous films in the early stages of film formation [67]. The tensile stress in the early stage of film growth is attributed to the nucleation and growth of three-dimensional individual islands. The local minimization of energy due to dynamic coalescence of islands is the governing mechanism in this stage. The independency of morphology and stresses of the details of the surface, except for the very early stages of film growth, is based on kinetic-induced growth instabilities and energy minimization. Morphology independent energy reduction at a surface can arise from surface reconstruction resulting in changing the surface packing density [68]. The difference with the biaxial strain ε

$$\frac{\partial \gamma}{\partial \varepsilon} = 2(f - \gamma) \quad (2.6)$$

is the driving force for the modification of surface packing density, known to cause surface reconstruction in crystal systems [69, 70]. In these systems, the elastic energy per area and the misfit energy to the bulk counteract. In above equation, f and γ are surface stress and surface energy, respectively, as discussed in earlier sections. In amorphous materials, however, with a very high energetically equivalent and almost randomly distributed positions on the surface, the misfit energy in the case of surface reconstruction should be negligible. In the case of sufficient low adatom mobility, the

modified adatom density can be extended to the bulk of the film and lead to biaxial film stresses

$$\sigma = -2(f - \gamma)/t_0 \quad (2.7)$$

In most metal systems, $f - \gamma$ is positive [70] leading to compressive stresses, the characteristic of the second growth regime in amorphous films. Atomic roughness observable in a typical amorphous film can be a good estimate for t_0 .

In the third stage, three dimensional columns growth generates tensile stresses in amorphous films due to local energy minimization by viscous coalescence in a dynamic equilibrium of stress generation and surface energy reduction (Fig. 2.8) [51]. In this case, the columnar structure may originate from cluster-like growth due to growth instabilities. In the very high film thickness regime, the energy is reduced by processes joining the walls of the columns together generating strain. The last stage of amorphous film growth does not depend on the history of growth at early stages of growth [71].

2.3 Strengthening Mechanisms in Crystalline and Amorphous Materials

The macroscopic mechanical behaviour of amorphous and crystalline materials is similar. For example, increase in strain rate and decrease in temperature result in more rigid material in both classes. The micromechanics of flow due to stress, however, differ substantially between the amorphous and crystalline solids. In crystalline materials, plastic deformation can be related to the clearly identified defects such as vacancies and dislocations within the crystal lattice. Although any plastic deformation happening in noncrystalline solids is attributed to the defects in these materials, these defects are not similar to those in crystalline materials. The difference in microstructure and atomic arrangement of amorphous and crystalline solids causes different mechanical behaviour in these materials under the applied stress. The dominant mechanisms for the mechanical behaviour of these materials will be reviewed below [72, 73].

2.3.1 Strengthening Mechanisms in Crystalline Materials

The required stress to make permanent deformation is an important issue in the mechanical behaviour of materials. In crystalline materials, this plastic flow is related to the presence of certain crystallographic defects called dislocations and their response to the applied stress [73]. In this section, different mechanisms by which flow strength increases in crystalline materials by restricting the motion of dislocations will be briefly discussed.

2.3.1.1 Strengthening from Grain Boundaries

A general relationship has been proposed between yield stress (and other mechanical properties) and grain size, which is known as Hall-Petch equation [72, 73]

$$\sigma_0 = \sigma_i + kD^{-1/2} \quad (2.8)$$

where σ_0 is the yield stress, σ_i is the friction stress representing the overall resistance of the crystal to dislocation movement, k is the locking parameter which measures the relative hardening contribution of the grain boundaries and D is the grain diameter.

Although the Hall-Petch equation was originally based on yield-point measurements in low-carbon steel, it has been found to be valid for the grain-size dependence of the flow stress at any materials. This equation has also been found to apply not only to grain boundaries but to other kinds of boundaries such as mechanical twins and martensite plates. The original dislocation model for this relationship was based on the concept that grain boundaries act as barriers to dislocation motion. This model has been modified and the new model is based on the effect of grain size on the dislocation density and, therefore, on the yield or flow stress [72, 74].

2.3.1.2 Solid Solution Hardening

The introduction of solute atoms into the solvent atom lattice in solid solution produces an alloy which is stronger than the constituent elements. There are two major types of solid solutions [72]: If the solute and solvent atoms are similar in size, the solute atoms occupy the lattice points in the crystal structure of solvent atoms. This is called substitution solid solution. When the size of the solute atoms is much smaller than the size of solvent atoms, they occupy the interstitial positions in the solvent lattice and the interstitial solid solution is resulted. To form a solid solution, the difference in atomic size between solute and solvent should be less than 15 percent, their electronegativity should be close and they should have the same crystal structure. It is well-known that solute atoms have more influence on the frictional resistance to dislocation motion than on the static locking of dislocations. Solute atoms fall into two broad categories in terms of their strengthening effect. Those atoms that produce non-spherical distortion, such as most interstitial atoms, have a relative strengthening effect per unit concentration of about three times their shear modulus. On the other hand, solute atoms that produce spherical distortion have a relative strengthening of about one-tenth of their shear modulus. Solute atoms can interact with dislocations by: elastic interaction, modulus interaction, stacking fault interaction, electrical interaction, short-range order interaction and long-range order interaction. Of these mechanisms, the elastic interaction, modulus interaction and long-range order interaction are relatively insensitive to temperature and continue to act up to $0.6T_m$. The other three mechanisms only contribute strongly to the flow stress at lower temperatures [72-75].

2.3.1.3 Strengthening from Fine Particles

Small second phase particles distributed in a ductile matrix are commonly used as a strengthening mechanism in alloys. In dispersion hardening, the hard particles are mixed with matrix powder, compacted and processed using powder metallurgy

techniques. However, very many alloy systems can be hardened by precipitation reactions in the solid state [72].

Precipitation hardening or age hardening is produced in an alloy in which a second phase is in solid solution with the matrix at elevated temperature but precipitates when the alloy is quenched and aged at a lower temperature. The age-hardening aluminum alloy and copper-beryllium alloy are the examples of this strengthening mechanism. For precipitation hardening, the second phase must be completely soluble in the matrix at elevated temperatures and shows decreasing solubility with decreasing temperature. In dispersion hardening, however, the second phase has very little solubility in the matrix even at elevated temperatures. Usually there is atomic matching or coherency between the lattices of the precipitate and the matrix phases, while in dispersion-hardened systems there is generally no coherency between the second phase particles and the matrix.

The degree of strengthening obtained from the second-phase particles depends on the distribution of particles in the matrix. In addition to shape, the second-phase distribution can be defined by specifying the volume fraction, average particle diameter and interparticle spacing. There are several ways in which fine particles can act as barriers to dislocations and their motion, which result in strengthening. They can act as impenetrable particles through which the dislocations can move only by sharp changes in the curvature of the dislocation line. In another scenario, they can act as coherent particles through which the dislocations can pass only at stress levels much above those required to move the dislocations through the matrix phase. Second-phase particles, therefore, act in two different ways to make the motion of dislocations difficult. The particles either may be cut by the dislocations or the particles resist cutting and the dislocations are forced to bypass them. Both of these mechanisms are energy consuming and result in increased strength [72, 73, 75].

2.3.2 Mechanical Behaviour of Amorphous Materials

Regardless of whether the amorphous material is a metallic glass, a silica-based glass or an organic glass (i.e., polymer), its structure shows no long-range order. The basic units of these three types of amorphous solids are, however, different in their short-range order. For metallic glasses, the basic units are simple, i.e., single atoms. For silicate glasses, the units are the more complicated SiO_4 tetrahedra, whereas for the polymers the basic units are the long-chain molecules [73]. This structural difference has no effect on the behaviour of these materials at high temperatures and all three types of amorphous materials behave like viscous fluid. This means that localized slip processes are associated with the permanent displacements of the basic units. As temperature is decreased, however, the macroscopic and microscopic flow behaviour change and the material becomes stiffer. In silicate glasses, plastic flow is completely impossible at low temperature and the glass is brittle (linear elastic solid). Low-temperature flow can still occur in metallic and organic glasses, but it becomes macroscopically heterogeneous. In metallic glasses, the heterogeneous flow is associated with localized and concentrated displacements of many atoms. In the case of long-range organic polymers, the flow is attributed to the molecular chain segments [73, 76]. The deformation in metallic glasses is discussed in more details below.

Metallic glasses are characterized by some excellent mechanical properties and deformation behaviour. Tensile modulus of metallic glasses is typically 30 percent lower than the modulus of these materials in crystalline form while their Poisson's ratio is higher. The higher Poisson's ratio shows that the amorphous metal is slightly less compressible compared to their crystalline form [73]. Of special interest is the high value of tensile strength for metallic glasses. These materials are inherently strong and their tensile strength to modulus ratio of about 0.02 is considered close to the theoretical strength of a material. Viscous flow, in which strain rate scales linearly with stress, is considered as dominant deformation mechanism in metallic glasses at temperatures

down to somewhat below glass transition temperature, T_g . At low temperatures, however, the linear elastic deformation is the dominant mechanism. Generally, two flow regimes are considered for the deformation of metallic glasses: (i) homogeneous deformation occurring at low stress levels and independent of temperature and (ii) inhomogeneous flow happening at high stress levels and low temperatures. In the former case, deformation takes place uniformly throughout the material. In the latter case, however, the permanent deformation is limited to small shear bands. This is mainly because of the fact that there is almost no strengthening mechanism in amorphous materials. Generally, there is no dislocation generation and motion in these materials compared to their crystalline form because of the lack of slip planes and directions. Even if there are some local dislocations in the short-range domains, they are not able to move and cause plastic deformation in metallic glasses [77-79].

2.3.3 Motivation for Having Nanostructured Amorphous Materials

The nanostructured bulk amorphous alloys can be obtained by annealing-induced partial crystallization in the supercooled liquid region followed by water quenching. This can be done by heating them to temperatures between T_g and T_c (T_c is the temperature at which rapid crystallization happens on heating). Alternatively, controlled intermediate cooling rates during crystallization can produce a mixed crystalline-amorphous structure. The crystalline particles obtained by this method are much smaller than those for the nanostructured amorphous alloys obtained by annealing (former method) and, hence, the structure obtained by the controlling process (the latter method) is named as a clustered amorphous alloy. When the amorphous phase contains a fine dispersion of the crystalline particles, the structures achieved from either method are supposed to show higher strength and ductility compared to those of metallic glasses although the reason for their higher ductility is not clear yet [80, 81].

Figures

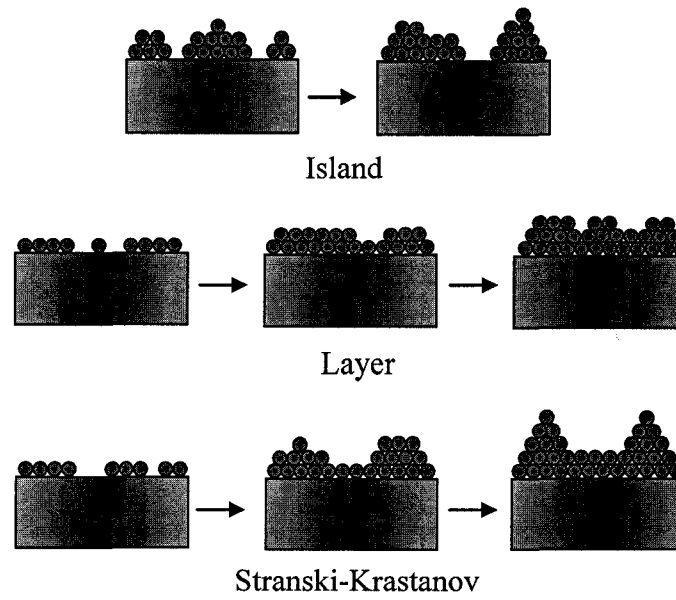


Figure 2.1: Schematic of three basic modes of thin film growth, based on [1]. Island (Volmer-Weber) growth, layer (Frank-van der Merwe) growth and mixed (Stranski-Krastanov) growth.

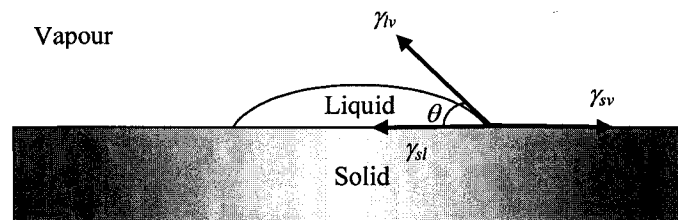


Figure 2.2: Young's equation for the wetting of a surface, based on [33, 34]. This equation relates liquid-vapour (γ_{lv}), vapour-solid (γ_{sv}) and liquid-solid (γ_{sl}) interfacial energies in terms of wetting angle (θ) as $\gamma_{sv} = \gamma_{sl} + \gamma_{lv} \cos \theta$.

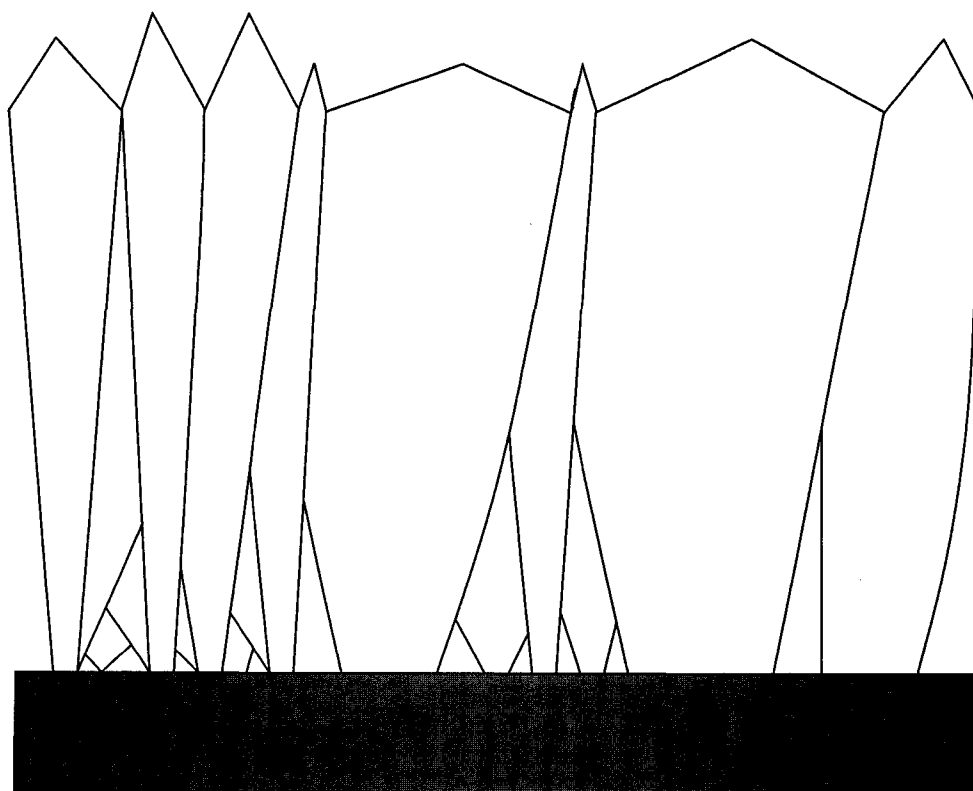
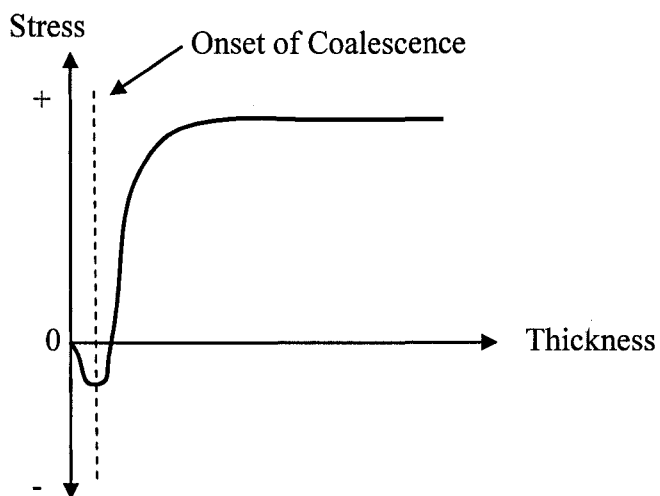
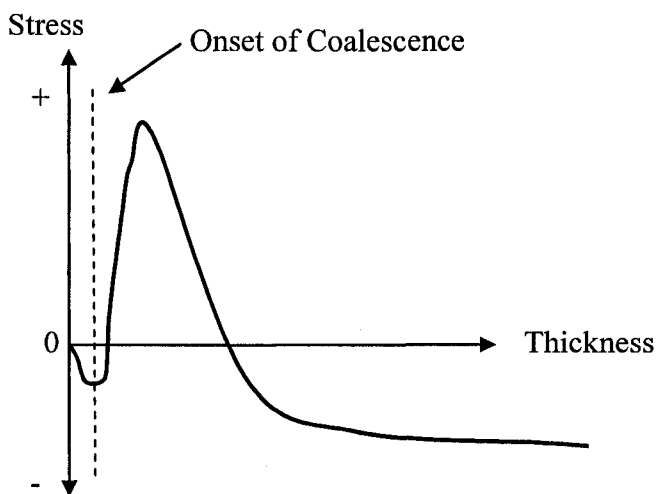


Figure 2.3: The competitive grain growth starting from randomly oriented nuclei on the substrate (bottom line) is shown (based on [40]). The grains that their fastest-growing orientation is normal to the substrate, overgrow other grains and win the competition.



(a)



(b)

Figure 2.4: (a) Schematic illustration of stress versus thickness plot for a metal with relatively low adatom mobility. Three stages of stress can be observed in the growth of these materials: compressive stresses before coalescence, changing in the sign of stress during coalescence and the tensile stresses after coalescence. (b) Schematic illustration of stress versus thickness plot for a metal with relatively high adatom mobility. There is a three-stage stress evolution in the growth of these films too: compressive stresses before coalescence, a change in sign of stress during coalescence and compressive stresses after coalescence (based on [57]).

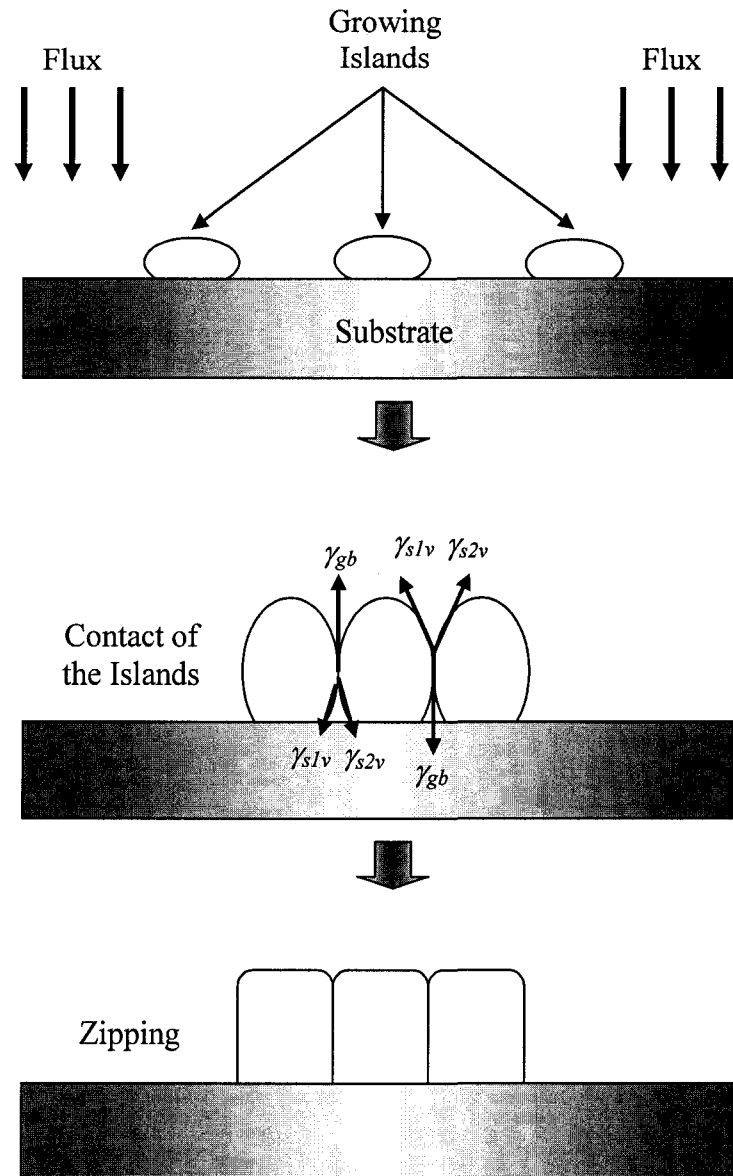


Figure 2.5: Schematic illustration of the Nix zipping mechanism, based on [35, 36], at coalescence of the islands. This mechanism explains the origin of the tensile stresses developing in thin film growth. When the isolated islands grow (top schematic), they contact each other at the top (middle schematic) and suddenly snap together (the bottom schematic) due to the tendency to reduce the surface energy. The sign of the intrinsic stress in the film changes, then, from compressive to tensile as a result of the substrate constraint.

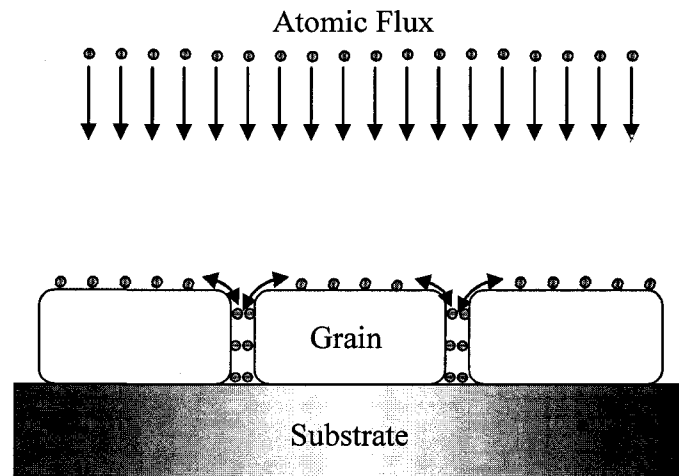


Figure 2.6: Schematic of the model for the flow of the atoms into the grain boundaries during the film growth due to the chemical potential gradient. Addition of atoms to the grain boundary results in the relaxation of tensile stresses and compressive stresses develop (based on [64]).

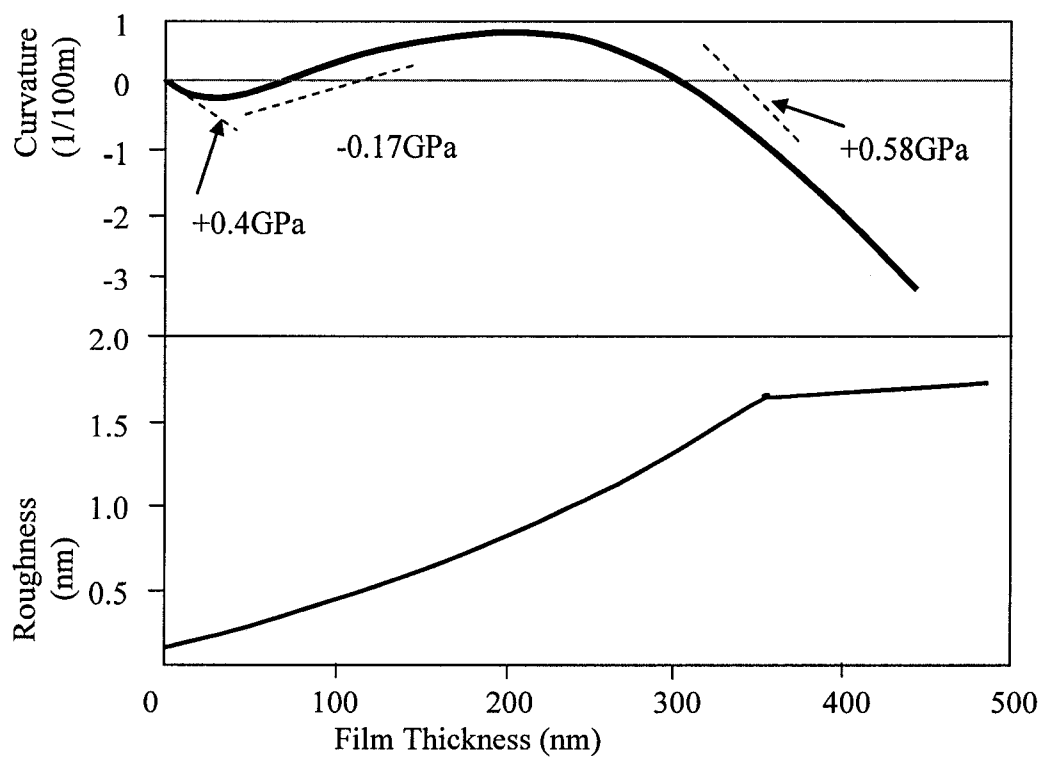


Figure 2.7: Evolution of substrate curvature and roughness with film thickness for amorphous Zr-Al-Cu films. A three-stage development of stresses is observed in the amorphous film growth: a very thin tensile stress regime, a compressive stress regime and the last tensile stress regime. A convention of positive curvature for compressive stress has been used here (based on [51]).

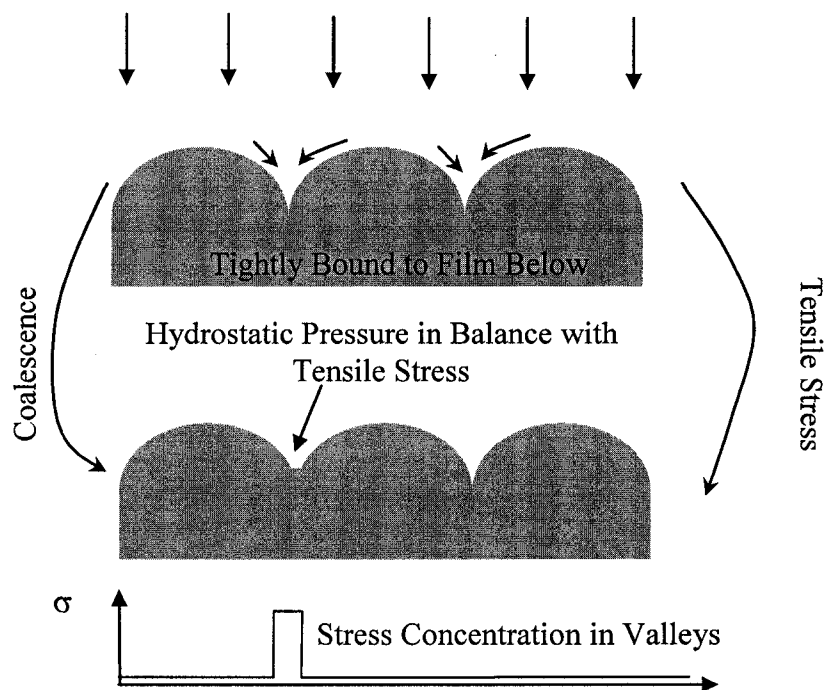


Figure 2.8: Model for the tensile stress generation due to the dynamic coalescence of the columns. This results in energy minimization, based on [51].

CHAPTER THREE: AMORPHIZATION CRITERIA

Various models have been proposed so far for the prediction of the composition range of the amorphous phase formation. These models are reviewed in this section briefly and discussed in more details in next sections. The interest in the formation of amorphous phase of two transition metals was stimulated by Schwarz and Johnson [82]. They showed that the amorphous phase could be obtained by solid-state reaction of multilayers of two transition metals. A review of the formation of amorphous phases by solid-state reaction has been published by Samwer [83]. The occurrence of the solid-state reaction implies that there is a thermodynamic driving force for amorphization; i.e., the amorphous phase has a lower Gibbs free energy than any other possible phases in multilayers. This free-energy insight has had an impact on the models that have been developed for the prediction of the composition range of amorphous formation. Traditionally, models were based on the information extracted from phase diagrams (Whang [84, 85]). This approach is inherently based on thermodynamic information for equilibrium states rather than any kinetic considerations. Another approach is based on differences in atomic size of the constituent elements [15, 86]. For a large number of alloys, the atomic size approach is successful. However, amorphous phase formation has also been observed for metal combinations where the differences in size are small. Therefore, a two-parameter method has been presented to address the deficiencies of the existing models [14, 87]. The new model was based on the atomic size ratio and the heat of formation of constituent elements. This scheme does not lead to an overall prediction of the composition range of amorphous phase formation. Tendency to form an amorphous phase can only be estimated from the two-parameter plot. In a method, developed by Miedema and co-workers [14], the relative position of the enthalpy curves of the solid solution and amorphous phase plays a central role in the prediction of the range of amorphous formation. In this approach, the effect of size is taken into account as well by considering an elastic mismatch energy. Furthermore, the structural stability

contribution to the enthalpy is estimated. Difference in atomic size and average number of valence electrons are the parameters that characterize the amorphous phase in this model. The different methods, mentioned briefly above, and their limitations in prediction of the composition range of amorphous formation are discussed in more details below. We will make a comparison then between these models and the experimental data obtained for Ni-Mo by us is analyzed and compared with the models in next chapters.

3.1 Atomic Size Ratio

It has been established empirically that easy glass formation is resulted when the atom radii of the constituent elements of the binary alloy differ by more than 10%. Generally, in such systems there is only a slight tendency for the formation of solid solution [88]. Egami and Waseda [15] correlated the atomic volume mismatch with the minimum solute concentration necessary to obtain an amorphous phase by rapid quenching. They found the following relationship between the minimum concentration (x_{min}) of solute B in solvent A, at which the amorphous phase starts to form, and the volume mismatch as

$$x_{min} \approx 0.1 \times \frac{V_A}{V_B - V_A} \approx 0.1 \times \left(\frac{r_A^3}{r_B^3 - r_A^3} \right) \quad (3.1)$$

where V_A and V_B are the atomic volume of the solvent and solute, respectively. Also, r_A and r_B represent the atomic radius of atoms A and B, respectively. As was demonstrated by Egami and Waseda, the relation holds well for a large number of binary alloys. However, a model only based on the atomic size ratio seems simplistic and other parameters should be considered as well.

3.2 Atomic Size Effect and Enthalpy of Mixing

Giessen and co-workers [14] proposed a two-parameter model for the prediction of the amorphous forming tendency of binary transition metal alloys. The parameters were the heat of formation and the atomic size ratio. Metallic glasses formed by melt spinning

had atomic size ratios between 0.85 and 1.15. Furthermore, various experimentalists have found a correlation between the glass-forming tendency and the heat of formation. Therefore, Giessen proposed a plot for the prediction of glass-forming ability. To make the plot, the atomic ratios and heats of formation were taken from Egami and Waseda [15] and Niessen *et al.* [89]. In the plot of heat of formation versus atomic ratio in this model, two distinct regions are present for each element in combination with other elements. A separating line between these two regions can be drawn, then, under which the alloys tend to form amorphous phase. The two-parameter model is, therefore, capable of prediction the tendency to form amorphous phase only and does not propose the range of amorphization.

3.3 Temperature-Composition (T-C) Model

It is well-known that the position of the liquidus and solidus lines in the phase diagram of the binary alloys provides a useful tool for the prediction of glass-forming ability [14, 84, 85]. Deep eutectic regions favour glass formation. In general, glass formation is achieved when by rapid cooling the temperature drops below the glass transition temperature, T_g , before crystallization can take place. The glass transition temperature is supposed to vary slowly with composition. When the liquidus temperature (T_l) varies steeply with concentration, there will be a composition range where there is only a small difference between T_g and T_l . Glass formation is especially favoured in this region. The reduced glass temperature, T_{rg} , which is defined as $T_{rg} = T_g / T_l$, can be a good parameter to estimate the glass-forming ability. Values of T_{rg} of 0.6 or higher indicate good glass-forming properties [14]. Whang *et al.* [84, 85] attempted to derive a more quantitative model essentially based on the principle that deep eutectics favour glass formation. The eutectic region is characterized not only by some reduced temperature parameters but also by a reduced composition parameter. In the hypothetical phase diagram of Fig. 3.1, for the composition region at the left of the eutectic point there is a reduced eutectic concentration defined as

$$x_{er} = \frac{x - x_s}{x_s} \quad (3.2)$$

In this equation, x_s denotes the minimum hypoeutectic composition and x is the nominal composition. Parameter x_{er} can take values between 0 and 1. For a value of $x_{er} = 0$, the composition is at the hypoeutectic point and a solid solution can form. Consequently, low x_{er} values prohibit easy glass formation. At the hypereutectic composition A_mB_n (Fig. 3.1), x_{er} equals unity by definition. Since at this composition no solid solution can form, glass formation should be relatively easy.

The second parameter is the reduced liquidus temperature, T_{lr} , which is defined as [90]

$$T_{lr} = \frac{\Delta T_l}{T_{0,l}} \quad (3.3)$$

where $T_{0,l}$ is obtained by linear interpolation between the melting temperatures of the two pure elements. ΔT_l is the difference between $T_{0,l}$ and the actual liquidus temperature at composition x . A two-parameter plot is obtained in this model (T_{lr} versus x_{er}), in which two regions can be distinguished. The region of easy glass formation is obtained at higher values of both x_{er} and T_{lr} (deep eutectic) [14, 84, 85, 87]. For the 3d-4d and 5d-5d alloys, predicted ranges of glass formation are lower than the experimentally observed ones.

A more simplistic approach, which also yields fairly reasonable results, has been proposed by Coehoorn *et al.* [91]. In their model, amorphous formation is possible for all those compositions for which no stable solid solution exists at any temperatures. In terms of Whang's model, the x_{er} parameter is allowed to approach zero whereas T_{lr} is neglected. This method shows promising agreement with the experimental results, especially for the 5d-5d binary alloys.

3.4 A Thermodynamic Model

Saunders and Miodownik [92, 93] and Bormann *et al.* [94] used an approach in which concentration-weighted lattice stabilities are applied to construct the enthalpies of different solid solution phases and liquid alloys. Excellent agreement was achieved between predictions and experiments for the occurrence of metastable solid solutions obtained by vapour deposition for a number of systems. The prediction of the formation of amorphous phases is less straightforward though. Since the heat of formation of the amorphous phase is lower than that of the liquid phase, amorphous alloys will form at least at those compositions where the heat of formation of the liquid is lower than that of the solid solutions. This idea has been confirmed by experiments. Saunders and Miodownik also derived the heat of formation of amorphous Cu-Zr and Co-Zr alloys by adding the heat of crystallization to the heat of formation for stoichiometric compounds. Unfortunately, their model has to rely on experimental information for a specific alloy system before quantitative predictions can be made.

Lopez *et al.* [95] and Miedema and co-workers [14, 87] proposed another model to predict the occurrence of amorphous phase formation based on the thermodynamic considerations. In this model, the enthalpies of formation of solid solutions are compared with the enthalpy of formation of the amorphous phase. The theory is dealt with in details below.

3.4.1 Free Energy of Solid Solutions

The free energy of solid solution (ΔG_{SS}) can be calculated from [14]

$$\Delta G_{SS} = \Delta H_{SS} - T\Delta S \quad (3.4)$$

where T is the temperature in Kelvin and the enthalpy of solid solution is obtained from the following equation

$$\Delta H_{SS} = \Delta H_{Ch} + \Delta H_{El} + \Delta H_{St} \quad (3.5)$$

In this equation, ΔH_{Ch} represents the chemical contribution to the total enthalpy and is the same for liquid and solid solutions. The ΔH_{El} term is the elastic mismatch energy, which appears in solid solutions. The third term on the right-hand side of the Eq. (3.5) represents the lattice stability, which varies continuously with the average number of valence electrons. It is assumed that the main entropy effect is the configurational entropy, which is considered the same for amorphous and solid solution phases and can be simply taken as that of ideal solid solution as [96]

$$\Delta S = -R(x_A \ln x_A + x_B \ln x_B) \text{ in KJ/mol.K} \quad (3.6)$$

where R is the ideal gas constant (8.314 J/mole.K) and x_A and x_B are the atomic concentrations of element A and B, respectively. The three terms in Eq. (3.5) are separately discussed below.

3.4.1.1 The Chemical Contribution

A semi-empirical model that can predict the enthalpy of formation of liquid and solid solutions of binary transition metal alloys has been constructed in Ref. 89. The chemical contribution, which is due to the electron redistribution generated at the contact between dissimilar atomic cells, depends on both the electronegativity difference and the difference in electron density. We can calculate the chemical contribution to the enthalpy of solid solution (in KJ/mol) from [14, 20]

$$\Delta H_{Ch} = x_A f_{AB} \Delta H_{Amp} \quad (3.7)$$

where ΔH_{Amp} is the amplitude concerning the magnitude of the electron redistribution interaction and is given by

$$\Delta H_{Amp} = \frac{V_A^{2/3}}{(n_{WS}^{-1/3})_{Ave}} \times \left(-P(\Delta\phi^*)^2 + Q(\Delta n_{WS}^{1/3})^2 \right) \quad (3.8)$$

In this equation, $((n_{WS}^{-1/3})_{Ave})$ is the mean value of the electron density in (density unit)^{1/3} at the boundary of the interacting atomic cells (it is also called Wigner-Seitz cell) for

the pure elements A and B in the metallic state. $(\Delta\phi^*)$ is the difference between the chemical potential of the electronic charge (ω) of atoms A and B in volt. P and Q are two empirical constants equal to $14.2 \text{ KJ/mol.cm}^2.\text{volt}^2$ (density unit) and $133.48 \text{ KJ/mol.cm}^2$ (density unit)^{1/3}, respectively. V_A is the atomic volume of component A in the alloy (in cm^3) and is defined as

$$V_A^{2/3})_{\text{Alloy}} = V_A^{2/3})_{\text{Pure}} [1 + \beta f_{AB} (\phi_A^* - \phi_B^*)] \quad (3.9)$$

where β is a constant equal to 0.04 volt^{-1} for most of the binary alloys. f_{AB} is a function accounting for the degree, to which atoms of type A are surrounded by atoms of type B and is given by [97]:

$$f_{AB} = X_B^S [1 + \gamma (X_A^S X_B^S)^2] \quad (3.10)$$

In this equation

$$X_A^S = \frac{x_A V_A^{2/3}}{x_A V_A^{2/3} + x_B V_B^{2/3}} \quad (3.11)$$

and

$$X_B^S = \frac{x_B V_B^{2/3}}{x_A V_A^{2/3} + x_B V_B^{2/3}} \quad (3.12)$$

are called surface concentration and $X_A^S + X_B^S = 1$. The parameter γ is used to describe the degree of chemical short-range order and is zero for solid solutions [98].

3.4.1.2 The Elastic Contribution

In metallic solid solutions, there is an elastic energy that is much larger than that for liquid and amorphous phases. The contribution of the elastic energy to the enthalpy of formation is estimated using the sphere-in-hole model as given in 14. In the sphere-in-hole model, a spherical hole of volume V_A (A is the matrix or solvent atom) is partly filled by a solute atom with spherical volume V_B . The missing volume or overlapping

volume will disappear by deformation of both solvent and solute. The pressure on the solute atom is related to its bulk modulus K_B and the pressure on the hole is determined by the shear modulus of the matrix, G_A . Since the changes in the volumes V_A and V_B are coupled, the elastic energy can be expressed in terms of the undisturbed volumes. The elastic energy $\Delta E_{El}^{A \text{ in } B}$ (in KJ/mol) is then given by [14, 99]

$$\Delta E_{El}^{A \text{ in } B} = \frac{2K_A G_B (V_B - V_A)^2}{3K_A V_B + 4G_B V_A} \quad (3.13)$$

Also,

$$\Delta E_{El}^{B \text{ in } A} = \frac{2K_B G_A (V_A - V_B)^2}{3K_B V_A + 4G_A V_B} \quad (3.14)$$

In this equation, V is related to the molar volume in cm^3/mol and K and G in GPa. On alloying, however, the volumes of the metal atoms change. By prediction of the net volume effect in combination with the elastic theory and assuming that the elastic parameters of individual atoms remain the same as for larger pieces of metal, the contribution of the elastic mismatch to the formation enthalpy can be calculated by

$$\Delta H_{El} = x_A x_B (x_B \Delta E_{El}^{A \text{ in } B} + x_A \Delta E_{El}^{B \text{ in } A}) \quad (3.15)$$

It should be noted that the elastic contribution has to do with alloying two transition metals and is absent when alloying a transition metal with a non-transition element [14].

3.4.1.3 The Structural Contribution

The structural contribution reflects the fact that transition metals of the 4d series, for example, show a preference to crystallize in one of the three simple crystallographic phases: BCC, FCC or HCP depending on the number of valence electrons Z (the d electrons). If it is assumed that the rigid-band model is applicable to binary solid solutions, the structural stability will vary systematically with the average number of valence electrons per atom. This assumption is justifiable for metals, in which the

valences do not differ greatly. The structural stability of solid solutions will, therefore, depend on the average number of valence electrons, \bar{Z} , in a similar way to the structural stability of the 4d elements.

An empirical curve of the variation in the stability of the three main crystal structure types with respect to the number of valence electrons, Z , has been constructed elsewhere [14] using data of solid solubilities (Fig. 3.2). The curves are plotted relative to a reference state, which is defined as the average enthalpy of the two close-packed structures and the looser packed BCC lattice

$$\frac{E_{HCP}(Z) + E_{FCC}(Z)}{2} + E_{BCC}(Z) = 0 \quad (3.16)$$

The structural contribution for solid solutions can be determined graphically from Fig. 3.2 and available tables in Ref. 14. It should be noted that the structural contribution to the total enthalpy is zero when alloying a transition metal with a non-transition metal.

3.4.2 Free Energy of Amorphous Phase

For an amorphous phase of binary alloys, the entropy is assumed the same as the entropy of ideal solutions and can be calculated from Eq. (3.6). The free energy of an amorphous phase can be calculated then by

$$\Delta G_A = \Delta H_A - T\Delta S \quad (3.17)$$

Both the elastic energy due to size mismatch and the structural stability can be neglected for amorphous phases and the enthalpy of the amorphous phase can be obtained from [14, 87]

$$\Delta H_A = \Delta H_{Ch} + \Delta H_{Fuse} \quad (3.18)$$

The ΔH_{Ch} term in the above equation can be calculated from Eq. (3.7) with the same ΔH_{Amp} as solid solutions (Eq. 3.8). The γ term in Eq. (3.10) for amorphous phases is different, however, from that of solid solutions and we have

$$f_{AB} = X_B^S [1 + 5(X_A^S X_B^S)^2] \quad (3.19)$$

In comparing the stabilities of solid solutions and amorphous phase, the contribution of the chemical term to the total enthalpy does not play a significant role. The term that plays a significant role is the enthalpy difference of the pure metal in the crystalline and amorphous states. Assuming that the enthalpy for amorphous pure metals is the same as that for liquid pure metals, the difference in enthalpy between the crystalline and amorphous states is given by ΔH_{Fuse} [95] as

$$\Delta H_{Fuse} = \alpha \bar{T}_{Fuse} \quad (3.20)$$

As an approximate best fit, α is given the value of 3.5 J/mol.K. In the above equation,

\bar{T}_{Fuse} is the concentration-averaged of the melting points and is expressed as [92, 93]

$$\bar{T}_{Fuse} = x_A T_{mA} + x_B T_{mB} \quad (3.21)$$

where T_{mA} and T_{mB} are the melting points of elements A and B, respectively.

3.4.3 Free Energy of Intermetallics

The free energy of the intermetallic phases is calculated by [14]

$$\Delta G_I = \Delta H_I - T\Delta S \quad (3.22)$$

The entropy changes (ΔS) in the above equation can be neglected in the ordered compounds because of its secondary role. The enthalpy term can be obtained from the following equation

$$\Delta H_I = \Delta H_{Ch} + \Delta H_{El} + \Delta H_{St} \quad (3.23)$$

The ΔH_{Ch} term can be calculated from Eq. (3.7) with the same ΔH_{Amp} as solid solutions (Eq. 3.8). The γ term in Eq. (3.10) for intermetallics is, however, different from that of solid solutions and has the value of 8 as

$$f_{AB} = X_B^S [1 + 8(X_A^S X_B^S)^2] \quad (3.24)$$

The elastic term, ΔH_{El} , of an intermetallic phase is related to the lattice distortion caused by size mismatch between the constituent elements. The ΔH_{El} term of different phases should be calculated in different ways according to their structural characteristics [87]. For phases at a composition near the eutectic point, where no intermetallics exist, the elastic term can be neglected due to the fact that an ordered arrangement of atoms can relax the lattice distortion caused by the size mismatch of the constituent elements. For the phases in the vicinity of the ordered compounds, however, the elastic term caused by the structural difference cannot be relaxed and can be calculated by Eqs. (3.13-3.15).

As has been discussed by Miedema and co-workers [14, 87], the structure of an ordered phase is different from the constituent elements and the difference in structure contributes to the free energy (or enthalpy). The ΔH_{St} term in Eq. (3.23) is, therefore, calculated by [87, 89]

$$\Delta H_{St} = E(Z) - x_A E(Z_B) - x_B E(Z_A) \quad (3.25)$$

where $E(Z)$, $E(Z_A)$ and $E(Z_B)$ are the structural stability factors of the intermetallic phase, element A and element B, respectively. Z , Z_A and Z_B are the mean number of valence electrons of the binary alloy phase and number of valence electrons of pure A and B. The dependence of the lattice stability on the number of valence electrons for paramagnetic transition metals in the three main crystallographic systems, i.e.: BCC, FCC and HCP has been calculated by Niessen *et al.* (Fig. 3.2) [99].

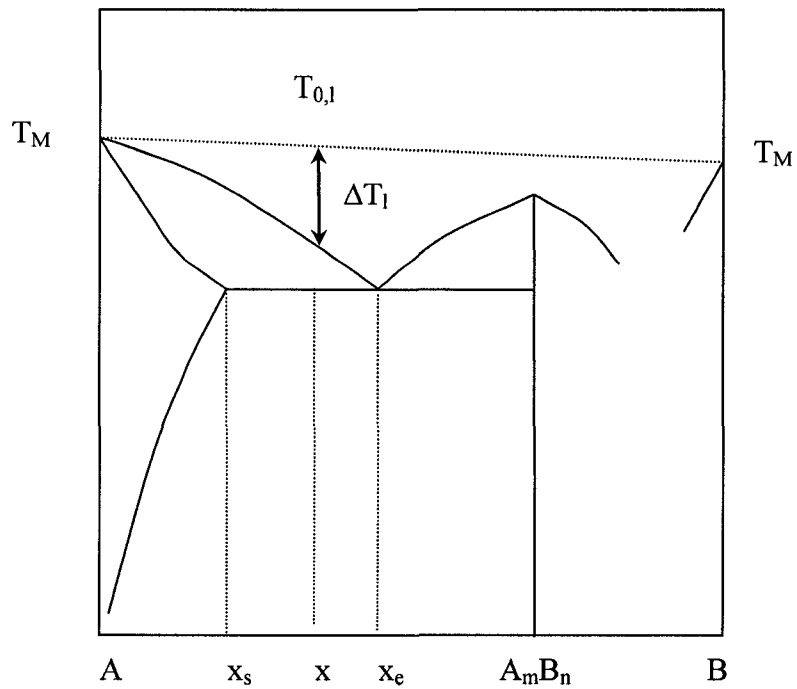
Figures

Figure 3.1: Hypothetical phase diagram with a eutectic surrounded by a solid solution region and an intermetallic compound, based on [85].

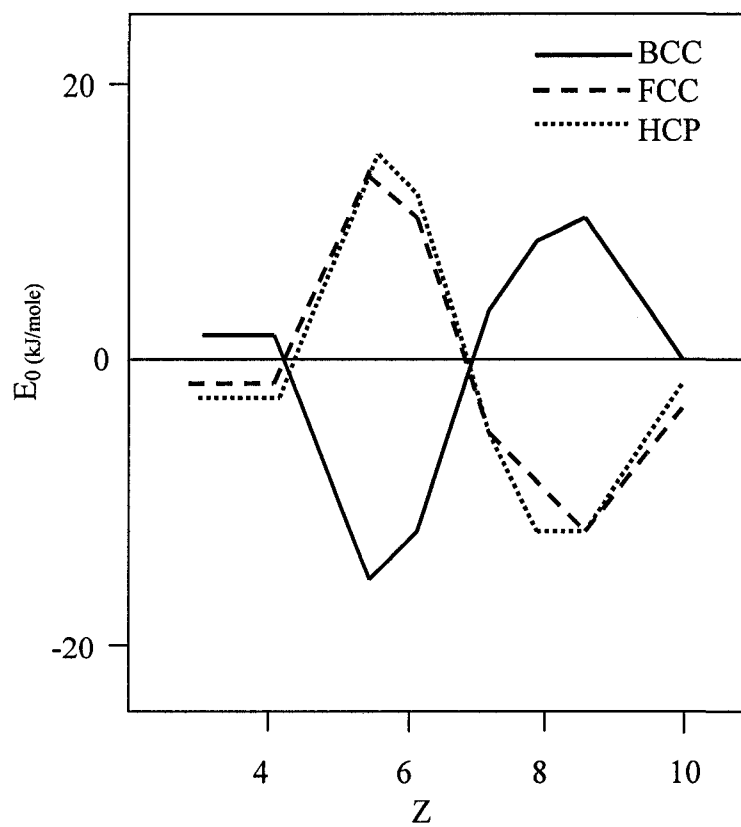


Figure 3.2: The structural stability $E(Z)$ of paramagnetic transition metals for the BCC, FCC and HCP structures as a function of the number of valence electrons per atom, Z (based on [14]).

CHAPTER FOUR: EXPERIMENTAL PROCEDURE

4.1 Fabrication of the Films

One micrometer thick nickel-molybdenum (Ni-Mo) films were deposited onto 4-inch standard silicon wafers (Silicon Valley Microelectronics, Santa Clara, USA) using a computer-controlled DC-magnetron co-sputtering system (AJA International, N. Scituate, USA). The wafers were cleaned before sputtering by using the piranha cleaning solution consisting of 3:1 mixture of 51% H₂SO₄ and 30% H₂O₂.

The films were synthesized by co-sputtering from pure Ni and pure Mo targets. Before the fabrication of the films, we carefully performed a calibration process to make sure that the composition and thickness of the films were consistent, uniform and reproducible. The deposition rates of Ni, Mo and Ti (as underlayer) were measured first at five different powers using a crystal monitor placed exactly where the wafer was going to be. These measurements were done by knowing the materials properties of each element such as atomic number, atomic weight and molar densities as input to the instrument. For each element, then, power of sputtering was graphed versus the deposition rate. This plot is almost linear for most of the materials. Next, the deposition of one element (say Ni) was kept fixed (at 1.42 Å/s for 100 watts) and using the molar densities of Ni and Mo, the deposition rate of the other element (say Mo) was calculated at each favourite composition (Ni-44at.%Mo, for instance). This deposition rate was plugged in then into the linear regression equation obtained from the graph of deposition power vs. rate, resulted above, and the required power was obtained for the second element. Finally, the time required for sputtering was calculated by dividing the total required film thickness (1 μm) by the sum of the deposition rates of the two constituent elements (Ni and Mo). These calculations were carried out for all of the favourite compositions and the results were used as input to the sputtering software. The vacuum base pressure and argon sputtering pressure were $\sim 5 \times 10^{-8}$ Torr and 4.0

mTorr, respectively, at all times (during calibration and sputtering). Dry argon gas with a purity of 99.99999 % was obtained from a tank connected to the sputtering system; however, the gas was not purified more at the point of use.

Deposition was done in a sputter-up configuration while substrate was rotating during the deposition process to ensure the uniformity in the film [1]. The sputtering temperature was allowed to float during deposition (substrate was unheated and uncontrolled). To study the microstructures and physical properties of the Ni-Mo binary alloy films, the films were synthesized for a full range of composition from pure Ni to pure Mo. As mentioned earlier, the Ni deposition rate, therefore, was kept constant at 1.42 Å/s and the Mo deposition rate was altered to make the adjustments to reach the desired stoichiometry. Also, a Ti film (5-20 nm) was used as an underlayer to provide better adhesion of the films to the substrate. The thickness of the Ni-Mo deposited films was measured using chemical etching (a hot mixture of HCl and HNO₃) and a contact profilometer (Tencor Alphastep) and it was confirmed to be 1000nm ± 5nm.

4.2 Material Characterization of the Films

The composition and purity of the films were confirmed by energy dispersive x-ray spectroscopy (EDS) mounted on a Hitachi S3000N scanning electron microscope (SEM). The composition of different fabricated films (1 μm thick) has been shown in Table 4.1. The atomic ratio of Ni/Mo has been shown in this table as well. The EDS results show that the films are metallic binary alloys with Ni and Mo as constituent elements and they are very low in metallic impurities. It is clear that these compositions are within the accuracy of EDS, i.e., 0.05-0.26 wt% of elements [100]. Also, the whole range of composition was covered from pure Ni to pure Mo, by addition of Mo to Ni, to make sure that we were not going to miss any changes in microstructure of the films. These results together with the thickness measurements show that the fabrication process of the films has been quite accurate, consistent and reproducible. The purity and

thickness of the films (in the order of $1000 \text{ nm} \pm 5 \text{ nm}$) show that the reliability of the process and fabricated films, as an important issue in thin film science and technology, has been quite good [101].

Table 4.1: Energy dispersive x-ray spectroscopy (EDS) results for the full range of composition of Ni-Mo films from pure Ni to pure Mo together with the Ni/Mo atomic ratios

EDS Results (Atomic %)		Atomic Ratio
Ni	Mo	Ni/Mo
100.0	0.0	-
94.2	5.8	16.12
87.6	12.4	7.07
76.9	23.1	3.32
66.4	33.6	1.97
56.1	43.9	1.27
45.9	54.1	0.85
30.6	69.4	0.44
22.1	77.9	0.28
13.4	86.6	0.15
6.0	94.0	0.06
3.3	96.7	0.03
0.0	100.0	0.0

A Hitachi S4800 high-resolution SEM was employed together with a Multimode Digital Instruments Dimension 3100 atomic force microscope (AFM) to examine the surface topography of the films. Depending on grain size, the AFM scan size was in the range of $5 \mu\text{m} \times 5 \mu\text{m}$ to $1 \mu\text{m} \times 1 \mu\text{m}$ to roughly keep the number of observed grains at different images constant (for better image processing). The AFM was used in tapping (non-contact) mode with Budget Sensors aluminum-coated tapping mode probes. Then, the AFM data was processed using Scanning Probe Image Processor (SPIP™) commercial software to measure the root mean square (RMS) roughness. It should be noted here that the resolution of the AFM with the above-mentioned tips (with a radius of $\sim 10 \text{ nm}$) strongly depends on the geometry and size of the surface features [102]. Therefore, any RMS value presented in this study is only an indication of surface

roughness; the actual surface roughness values must be obtained using much smaller tips. It is clear, however, that since we used the same tip's geometry and size for all of the films, any present artifacts and their associated errors will enter all of the images. Thus, the presented AFM results and RMS roughness values are for comparison purposes between the fabricated films only.

A conventional x-ray diffraction, XRD, (Bruker AXS Inc., Madison, USA) was used together with a conventional JEOL 200CX transmission electron microscope (TEM) operating at 200 kV for phase identification and detailed microstructural studies. Selected area diffraction (SAD) patterns, obtained in TEM studies, were employed for phase identification. High-resolution transmission microscopy (HREM) was used at 200 kV in a Philips CM200-FEG and at 150 kV using a CM300-FEG TEM. The cross-sectional TEM specimens were prepared by a tripod polisher followed by cryogenic ion milling. To measure the oxygen content on the surface of the films, x-ray photoelectron spectroscopy (XPS) was used. It should be noted that this surface characterization technique has an interaction volume of <5 nm and has a detection limit of 0.1 at.%. Hydrogen and helium cannot be detected by this method [103]. Also, the thermal stability of the films was tested using differential scanning calorimetry, DSC, (SDTQ600, TA Instruments, USA). The heating rate for this experiment was 10 °C/min in an argon environment.

4.3 Measurement of Physical Properties

Nanoindentation test was performed (in collaboration with the LBNL National Laboratory, Berkeley, USA) to measure nanohardness and modulus of elasticity of the Ni-Mo films at different compositions using a commercial load-depth sensing instrument (Hysitron TriboIndenter, Minneapolis, USA) equipped with an AFM. All of the tests were performed using a Berkovich indenter tip and an applied load of 2500 μ N. Each data point represents 25 measurements with a nanoindentation separation

distance of at least 25 μm . Hardness and elastic modulus were measured from unloading part of the load-depth curve using Oliver and Pharr method [104]. The stress on the films was measured by means of a KLA Tencor Flexus thin film stress measurement system. This system works according to the difference in the wafer curvature before and after deposition. The curvature was examined by the reflection of a laser from the surface. Electrical resistivity of the films was measured as well using a standard 4-wire probe measurement technique.

4.4 Fabrication of Cantilevers

Single-clamped cantilevers were fabricated (in collaboration with the Dr. Stephane Evoy's group, Department of Electrical and Computer Engineering) to a thickness of 50 nm at the widths of 400 nm and 800 nm with different lengths from 1 μm to 6 μm using the following nano-fabrication process. This fabrication method is similar to one reported elsewhere [2].

A silicon prime wafer was obtained for the structural base for the cantilevers. The wafer was cleaned in a hot piranha solution, then was rinsed with de-ionized water and was cleaned in a spin-rinse dryer. A 400 nm layer of SiO_2 was grown on the wafer by wet oxidation. We cleaved the oxidized wafer into small dies for use in the electron beam lithography system. Then, a layer of PMMA 495 was spun onto the die and it was baked on a hotplate. A layer of PMMA 950 was spun onto the die as well and we baked it then on the hotplate for 30 minutes at 235°C. The photoresist was patterned afterwards with the RAITH150 electron beam lithography system using standard settings. The resist was developed in a solution of one part methyl isobutyl ketone (MIBK) and three parts of isopropyl alcohol (IPA), then was immersed in an etch stop solution of IPA and was rinsed in a beaker of de-ionized (DI) water. The developed die was then subjected to a plasma to etch the first few nanometres of the resist surface. A reactive ion etching (RIE) system was pumped down and the die was subjected to an O_2

plasma. A 50 nm thick layer of Ni-44at.%Mo (that had the optimum properties as we would see later) was deposited on the die using a magnetron sputter system. Then, the die was immersed in a buffered oxide etching (BOE) solution, in order to release the cantilever devices, and was rinsed in two different water baths before being immersed in an IPA beaker for transferring to the critical point dryer. The die was then dried in a critical point drying machine. These Ni-Mo cantilevers were then used for SEM imaging. High-angle images were taken of the cantilevers using the high-resolution SEM to make sure that the cantilevers are fully-released, clean and not deformed as a result of stresses.

CHAPTER FIVE: RESULTS AND DISCUSSION

5.1 Prediction of the Composition Range of Amorphous Phase

In Chapter 3, we discussed the various proposed methods for the prediction of the formation range of amorphous and other metastable phases. In this section, the results of modeling according to those approaches are presented and in next section these results will be compared with the experimental data we obtained for Ni-Mo in this study.

In Table 5.1, the composition range of amorphous phase formation calculated using the atomic size ratio model (Eq. 3.1) is given for Ni-Mo. This model, which is simply based on the atomic size difference, predicts the range of amorphous formation of 36at.%<Mo<54at.% for Ni-Mo binary alloy. As mentioned earlier, however, prediction of the amorphous range based on atomic size difference only seems simplistic and other parameters such as heat of formation should be taken into account as well.

Table 5.1: Calculated values for minimum concentration of solute, at which the amorphous formation begins in Ni-Mo system according to the atomic size model [14]

Element	Atomic Size (Å)	$x_{min}(\text{Ni-Mo})$	$x_{min}(\text{Mo-Ni})$
Ni	1.28	0.36	0.46
Mo	1.39		

The “atomic ratio and heat of formation” model (Section 3.2), on the other hand, is only capable of prediction the tendency to form an amorphous phase and it does not give any composition range. According to the available data in the literature based on this approach for Ni-Mo [14, 87], this binary system is not able to form any amorphous phase. Deviations from this model have been reported, however, for many alloys and

this model has been proven not to be very accurate in predictions because of inaccuracy in the experimental data that the method is based on [14].

The values of x_{er} and T_{lr} according to the temperature-composition (T-C) model (Section 3.3) are shown in Table 5.2. The results of this model for the Ni-Mo system shows starting ranges of the amorphous formation of about 43at.% and 5at.% in the Ni and Mo sides, respectively. It has been shown that this model does not give very accurate ranges for amorphous formation due to the fact that it has been based on the equilibrium diagrams to predict non-equilibrium phases [14].

Table 5.2: The calculated values of x_{er} and T_{lr} for Ni-Mo system (Section 2.3) according to the temperature-composition (T-C) model

Ni Side			Mo Side		
x	x_{er}	T_{lr}	x	x_{er}	T_{lr}
0	-1	0	0	-1	0
5	-0.82	0.05	5	1.17	0.05
10	-0.64	0.09	10	3.35	0.05
15	-0.46	0.13	15	5.52	0.03
20	-0.28	0.17	20	7.69	0.05
25	-0.11	0.22	25	9.87	0.07
30	0.07	0.27	30	12.04	0.06
35	0.25	0.31	35	14.22	0.31
40	0.43	0.28	40	16.39	0.28
45	0.61	0.23	45	18.56	0.23
50	0.78	0.20	50	20.74	0.20
55	-1	0.16	55	22.91	0.16

The values for the parameters used in Miedema's model (Section 3.4), are given in Table 5.3 for Ni-Mo binary alloy. The free energy curves of the possible phases, obtained for this system using the Miedema's model, have been shown in Fig. 5.1. Different calculated curves for solid solution, amorphous and intermetallic phases are shown in this figure. At any desired composition, the phase associated with the lower free energy curve is thermodynamically stable. For the compositions between two

curves (such as solid solution and amorphous), stable phases can be found by drawing a tie-line between those two. The Miedema's model considers most of the parameters involved in alloying of two transition metals and is the most comprehensive method proposed so far for the prediction of the formation range of amorphous and other metastable phases. This thermodynamic model predicts a formation range of 38at.%<Mo<68at.% for the amorphous phase.

Table 5.3: The parameters used to model the formation range of metastable phases in Ni-Mo according to the Miedema's approach [14]

Parameter	Ni	Mo
V (cm ³)	6.60	9.4
ϕ^* (volt)	5.20	4.65
$n_{ws}^{1/3}$ (density unit) ^{1/3}	1.75	1.77
K (GPa)	177.3	261.2
G (GPa)	76.0	125.6
P (KJ/mol.cm ² .volt ²) (density unit)	14.20	
Q (KJ/mol.cm ²) (density unit) ^{1/3})	133.48	

5.2 Material Characterization of the Films

After confirming the composition and purity of the films by energy dispersive x-ray spectroscopy (EDS), scanning electron microscopy (SEM) and atomic force microscopy (AFM) were performed on the samples to examine and analyze their surface topography. These results are shown in Figs. 5.2-5.7. It can be observed from the SEM results (Figs. 5.2-5.4) that as the Mo content increases from 0at.% to 100at.%, surface topography of the films changes showing a qualitatively change in surface roughness. In these images, three distinct microstructural regions can be found: rough surfaces from pure Ni to Ni-23at.%Mo (Fig. 5.2), smooth surfaces from Ni-34at.%Mo to Ni-69at.%Mo (Fig. 5.3) and rough surfaces from Ni-78at.% Mo to pure Mo (Fig. 5.4). To measure the surface roughness of these films quantitatively, their AFM

micrographs shown in Figs. 5.5-5.7 were used. We can see from these images that the RMS roughness generally decreases from 11 nm to 5.5 nm for the first region (Fig. 5.5), stays atomically smooth in the middle composition range with a RMS of less than 1 nm (Fig. 5.6) and increases again to 8.1 nm for pure Mo in the third region (Fig. 5.7).

To identify the phases present in the films in these three regions of composition and microstructure, x-ray diffraction (XRD) was employed the results of which are shown in Figs. 5.8-5.12. It can be seen from the XRD spectra that for the first region of microstructure, associated with the images of Figs. 5.2 and 5.5, a fully crystalline face-centered cubic (FCC) structure is present based on the simulations using Desktop Microscopist™ software (Fig.5.8). The Vegard's law plot for these films is depicted in Fig. 5.9 showing that surprisingly the rule of mixture is valid for this part of composition range and a solid solution phase exists. Vegard's law is a plot of lattice parameter versus composition and is based on the experimental data for substitutional solid solutions of two metallic elements with the same crystal structures. In Fig. 5.9, the top line is the rule of mixture from the equilibrium lattice parameters of pure Ni and pure Mo versus composition. The bottom line, however, is the plot according to the lattice parameters obtained from FCC <111> peaks of Fig. 5.8. The small difference between these two lines can be due to the presence of stresses and/or the difference between the atomic radii of Ni and Mo in their pure crystal structures and in solid solution. The XRD signals for the middle range of composition (34at.%<Mo<69at.%), attributed to Figs. 5.3 and 5.6, are given in Fig. 5.10. These results show that either amorphous phase, or nanocrystalline phase or both can be present in these films because of the peak broadening [105]. Assuming the broadening is due to spherical nanocrystallites, their size was estimated to be in the range of 1.5 nm - 2.5 nm by simulation using the well-known Sherrer Equation [106]

$$d = \frac{0.9\lambda}{B \cos \theta} \quad (5.1)$$

In this equation, λ is the wavelength of the x-ray, B is the full width of the broadened peak at half maximum and θ is the Bragg's angle. It was discussed earlier that the Vegard's rule is valid for solid solutions only and clearly does not apply to this composition range. For the third region of composition (Figs. 5.4 and 5.7), on the other hand, the XRD peaks show that a body-centered cubic (BCC) crystal structure is present (Fig. 5.11). The films in this composition range follow the Vegard's law as well (Fig. 5.12); the small difference between the two lines can be due to the intrinsic stresses present in the films or change in lattice parameter in solid solution compared to the unmixed form of elements.

To identify the phase/phases present in the middle range of composition (Ni-34at.%Mo to Ni-69at.%Mo) and to see if they are amorphous or nanocrystalline or both (Fig. 5.10), transmission electron microscopy (TEM) was employed as a powerful tool for phase recognition. We chose the Ni-44at.%Mo film (with optimum properties), as a representative of this composition range, for phase identification using TEM. The results are shown in Figs. 5.13 and 5.14. Fig. 5.13 shows the bright field (BF) and dark field (DF) plan-view images of Ni-44at.%Mo together with its selected area diffraction pattern (SAD). The cross-sectional view of the film is shown in Fig. 5.14 as well. These two figures show that the microstructure of this film consists of nanocrystallites randomly and densely dispersed in an amorphous Ni-rich matrix (the diffuse background in Fig. 5.13c). We call this structure ``nanocomposite microstructure``. By further investigation and simulation of the diffraction pattern (Fig. 5.13c) using Desktop Microscopist™ commercial software, it was deduced that the nanocrystallites had a BCC crystal structure. High resolution transmission electron microscopy (HREM) was used as well to image this sample and the results are shown in Fig. 5.15. In these images, the nanocrystallites (less than 5 nm in size) and lattice fringes can be observed.

From the above experimental results discussed in details, the amorphous composition range of 34at.%<Mo<69at.% was found in Ni-Mo binary alloy films. The results of the prediction of the amorphous formation range, obtained for Ni-Mo in the previous section according to different existing models, are summarized in Table 5.4 and shown schematically in Fig. 5.16 together with our experimental data.

Table 5.4: Predicted range of amorphous phase for Ni-Mo calculated using different models discussed in Chapter One (Chapter B). The experimental result of this study has been shown as well for comparison purposes.

Method	Prediction (Ni Side)	Prediction (Mo Side)	Difference with Experiment (%)	
			Ni Side	Mo Side
Atomic Size Ratio	0.36	0.46	5.8	48.4
Atomic Size and Enthalpy	Not Forming	Not Forming	-	-
Temperature-Composition (T-C) Model	0.43	0.05	26.5	83.9
Miedema	0.38	0.32	11.7	3.1
Experiment	0.34	0.31		

It can be seen from above table and Fig. 5.16 that although the “atomic size and enthalpy of mixing” model is only capable of predicting the ability of the alloys to form an amorphous phase, its prediction for Ni-Mo binary alloy does not match at all with our experimental results. It has been seen by other researchers as well that a number of alloys form amorphous phase although they do not follow this model [14, 87]. On the other hand, the “temperature-composition (T-C)” approach is able to predict the range of amorphous phase; however, the results are far from our experimental data that can be due to the fundamental assumptions of this model, which are based on phase diagram and equilibrium states. It can be observed from the above table, however, that the “atomic size ratio” method proposed by Egami and Waseda is quite successful in the prediction of the amorphous phase formation in the Ni side but it fails in the prediction of the amorphous phase starting range from the Mo side. It has been proven that for

some of the vapour-deposited alloys, the size rule does not hold since this model has been originally proposed for the binary alloys prepared by liquid quenching [14, 15, 87]. Moreover, the prediction of amorphous phase formation based only on the atomic size difference seems simplistic. The best match between the experimental and modeling results is obtained using the Miedema's approach; the difference between the prediction and experimental data is relatively low. The reason for this close match is that the Miedema's model is the most comprehensive model proposed so far for the prediction of amorphous range and it considers most of the parameters involved in amorphization. This model is able to predict the presence of both metastable and intermetallic phases as can be seen in Fig. 5.1. The intermetallic phases, predicted by Ni-Mo phase diagram (Fig.1.1), will be present only when the special requirement of equilibrium conditions such as long-range diffusion is met. These phases, however, were not kinetically accessible because of our experimental conditions (kinetics of sputtering) and were not traced in our XRD and TEM results. Also, according to Miedema's model prediction (Fig. 5.1) there are two-phase regions in which a mixture of solid solution and amorphous phase can be obtained (tie-lines and light-gray squares in Fig. 5.17). Due to the kinetics of sputter deposition, however, these two regions can shrink and be pushed toward the center (dark-gray squares in Fig. 5.17). In this way, we expect to have a mixed microstructure of amorphous-crystalline phases as observed from our experimental results (Figs. 5.10 and 5.13-5.15). It should be mentioned that according to our knowledge, this nanocomposite microstructure consisting of amorphous and nanocrystalline phases obtained by sputtering is entirely new. The only comparable microstructure to what we obtained from our design and experiments is the one resulting from the annealing of a 100%-amorphous bulk material. In this way, as discussed in Section 2.3.3, nanoparticles crystallize in the amorphous matrix [28, 80]. Since there is no explanation for the formation and growth of our nanocomposite films in literature, we consider two possibilities here for this process:

1. Since there is an elevated temperature at the growth front, there is a possibility that the amorphous phase partially crystallizes in this region as the film grows. This transformation at the growth front can result in nanocomposite microstructure consisting of nanocrystallites in an amorphous matrix.
2. Alternatively, what may be happening is that there is a super-saturated amorphous phase forming at the growth front at elevated temperature. As the film cools down to the room temperature, however, the Mo nanocrystallites segregate due to the reduced solubility of amorphous phase. This process can be assumed to be similar to clustering (or precipitation) of the metastable phases in some aluminum-based alloys such as Guinier-Preston (GP) zones in aluminum-copper alloys [34, 72, 73].

Also, to identify the growth mode of the films and view their topography across the thickness, high-angle high-resolution cross-sectional SEM was used. The images of cross section of pure Ni (as representative of polycrystalline films) and Ni-44at.%Mo (as representative of nanocomposite films) are shown in Fig. 5.18. The micrograph of Fig. 5.18a clearly illustrates the competitive grain (column) growth, as a result of van der Drift growth mechanism explained in Chapter 2, for polycrystalline films. This type of growth is responsible for the high surface roughness observed for the crystalline films (Figs. 5.5 and 5.7). Also, the difference in surface topography of the films between Fig. 5.2 (Ni side) and Fig. 5.4 (Mo side) can be attributed to the difference in the fastest-growing directions in FCC and BCC films, respectively, that affect the shape of the grains winning the competition in the competitive grain growth. No grain growth was found, though, in the Ni-44at.%Mo film (Fig. 5.18b) showing that a combination of amorphous growth mechanism (Sections 2.1.2 and 2.2.2) and one of the two possibilities discussed above might be the dominant mechanism in the formation of our nanocomposite films.

At the end, it is worth mentioning that the oxygen content at the surface of the films was examined using x-ray photoelectron spectroscopy (XPS) the results of which show that the oxygen content is close for the three films we tested, i.e., pure Ni, Ni-44at.%Mo and pure Mo (Table 5.5).

Table 5.5: Oxygen content of the surface of pure Ni, Ni-44at.%Mo and pure Mo films. The concentrations are in atomic percent.

Material	Oxygen Content (at.%)
Pure Ni	44.45
Ni-44at.%Mo	39.52
Pure Mo	38.82

5.3 Physical Properties of the Films

Measured physical properties of the Ni-Mo films are shown in Figs. 5.19 to 5.21 for the complete range of composition from pure Ni to pure Mo. Figure 5.19 shows the results of nanohardness and Young's modulus from nanoindentation test. Also, surface roughness and intrinsic stress values are graphed in Fig. 5.20. Moreover, the resistivity of the films was tested, the results of which have been shown in Fig. 5.21.

Generally, three distinct regions can be distinguished in the physical properties of the films in terms of composition. These three composition ranges are attributed to those obtained in the characterization results discussed in the previous section; i.e., for the compositions below 23at.%Mo the films are polycrystalline FCC with competitive grain growth. From 34at.%Mo to 69at.%Mo, however, a nanocomposite microstructure is present in the films. For the films with the Mo content of more than 78at.%, on the other hand, a BCC crystal structure and competitive growth are dominant. It can be seen from the nanoindentation results of the films that the hardness and modulus for pure Ni and pure Mo (Fig. 5.19) are close to what have been reported in the literature [2, 21, 107]. Also, for the first region of composition range the nanohardness (Fig.

5.19a) generally increases by the addition of Mo to pure Ni which can be due to the solid solution hardening and reduced grain size (Hall-Petch) effects. As discussed in Section 2.3.1 [72, 73], by introducing the Mo atoms to Ni crystal structure, the motion of dislocations becomes difficult leading to increased hardness and strength. In addition to this effect, when the Mo content increases, the grain size generally decreases (Figs. 5.2 and 5.5). The reason for obtaining the lower grain size with increasing the Mo content can be due to the low mobility of Mo atoms compared to Ni that can avoid the grains from further lateral growth during the deposition. The decreased grain size results in increased strength and hardness according to Hall-Petch equation (Eq. 2.8). Also, the modulus values for this region (Fig. 5.19b) follow almost the same trend as hardness although the discrepancy in data is high. The off datapoints in Fig. 5.19 might be possibly because of the high sensitivity of measurements and analyses in nanoindentation test to porosity of the films that introduces some errors to the data [104] or the formation of stacking faults. It can be seen in Fig. 5.20a that, for below 23at.%Mo, the roughness decreases generally by the addition of Mo to Ni which can be attributed to the reduced grain size in this region (Figs. 5.2 and 5.5) as discussed above. As a result of competitive grain growth and van der Drift mechanism, therefore, the grain size at the end of the growth process is a function of Mo content and decreases generally with increasing Mo. This, in turn, can cause reduced roughness in the films for the first crystalline composition range. The stress-state for this composition range (below 23 at.%), on the other hand, is tensile which can be because of the development of tensile stresses initiate at zipping process of the islands. It was discussed in Section 2.2.1 [35, 57] that this tensile stress remains tensile and increases with thickness for the materials possessing low adatom mobility such as Ni and Mo (Fig. 2.4a). The reason for decrease in tensile stress with Mo content, however, might be due to the increase in the deposition rate with increasing Mo that can cause implantation and peening phenomena. These two phenomena, in turn, can relax and reduce the tensile stresses in the films (Section 2.2.1). In addition, the resistivity of the films increases with Mo

content for the first region (Fig. 5.21) that can be due to the introducing the Mo atoms (considered as defects) to Ni lattice and reduced grain size.

By adding more Mo to Ni, however, we enter the second region of composition in which the increased hardness and modulus, reduced roughness and intrinsic stress, and increased resistivity are mainly because of the presence of nanocomposite microstructure. In addition, these properties remain almost constant in this composition range (34at.%Mo-69at.%Mo). It was seen in Section 2.3 that amorphous materials have higher mechanical properties than their crystalline counterparts due to the absence of or limitation in plastic deformation (no dislocation motion). Also, introducing a second phase enhances the mechanical properties of amorphous materials [73, 80]. Therefore, we expect to see higher hardness and modulus for the middle range of composition as observed in Fig. 5.19. The average hardness and modulus of about 11 GPa and 200 GPa are considered high in thin films [1, 2, 73]. The reason for obtaining ultra-smooth surfaces for this region (Fig. 5.20a), on the other hand, can be attributed to the absence of (competitive) grain growth and also to the different mode of growth for amorphous films. As mentioned earlier (Section 2.2.2), the growth of amorphous phases consists of three stages: nucleation of the islands on the substrate, growing of these islands as thickness increases and coalescence of the so-called domains walls together. It is, therefore, expected to see a very smooth surface in amorphous films (Figs. 5.4 and 5.7) as a result of dynamic smoothening process that happens in their growth [44, 46, 51]. The very low (compressive) stresses observed for these films (Fig. 5.20b) can be resulted from two phenomena: growth and stress relaxation. It was noted above and in Section 2.2.2 that the stress evolution in amorphous phases starts with a very thin film tensile stress state followed by compressive stresses in medium thicknesses and eventually becomes tensile at very high film thicknesses (Fig. 2.7) [51]. The observed compressive stresses for these amorphous films, therefore, show that the final stage of growth associated with the tensile stresses has not been reached yet for these films and

the deposition has been stopped in the second stage of growth. To confirm this explanation and further investigate the stress evolution in our nanocomposite films, the stress was measured versus thickness for Ni-44at.%Mo film the results of which have been shown in Fig. 5.22. It can be observed from this figure that stress starts from a tensile state (the extrapolation trendline) for low film thicknesses, goes to compressive at the medium thicknesses and eventually becomes tensile when the thickness is high. This data is in a good agreement with the trend proposed for amorphous films in the literature [51]. It should be noted that the measurement of stress for the low thicknesses was not possible due to the limitations of the measurement technique. Another possibility for the observed compressive stresses in nanocomposite films in the middle range of composition (Fig. 5.20b) is that the crystallization of the amorphous phase at the growth front and/or clustering of nanocrystallites from the amorphous matrix (explained above) can relax the developed stresses in the films. The conductivity data (Fig. 5.21) for the middle composition range shows an order of magnitude decrease compared to pure Ni and pure Mo while it is still in the metallic range. This decrease can be because of the reduced mean free path length in the amorphous phases and the existence of the atoms second element (solute scattering).

For the third region of composition range, on the other hand, the trend in physical properties is similar to that observed in the first crystalline region with some minor differences due to the BCC crystal structure rather than FCC. It can be seen from the right-hand side of Fig. 5.19a that the hardness of the films decreases with increasing Mo content (from 78at.%Mo to pure Mo) that can be due to the increase in grain size and decrease in Mo atoms in Ni structure (solid solution hardening and Hall-Petch effects). These effects are opposite to those explained at the beginning of this section for the first region of composition since the Mo content is decreasing. Almost the same trend is observed for modulus as well (Fig. 5.19b). Also, the surface roughness for this range increases as a result of competitive grain growth which becomes dominant in

these polycrystalline films again. However, the surface roughness for the films in this composition range is generally lower than that observed in the first composition range (left-hand side of Fig. 5.20a). This can be due to the difference in fastest-growing directions in BCC films and FCC films (Figs. 5.2 and 5.4). Moreover, the stress state is tensile again in this zone (Fig. 5.20b) since the Mo content (with low adatom mobility) increases and the films are in the tensile stress regime developing after coalescence and zipping of the islands (Fig. 2.4). In addition, a decrease in the resistivity data is seen in the right-hand side of Fig. 5.21 which can be because of the decrease in Ni content (defects) and increase in grain size (mean free path length) in the films. It should be noted again that the errors exist with some datapoints, especially in nanoindentation results, can be due to porosity of those films that affects the results and/or solute scattering. These faulty datapoints will be regenerated in future to clarify any ambiguity.

5.4 Synthesized Cantilevers

According to the results discussed earlier in details, it is clear that if one wants to synthesize MEMS/NEMS devices from Ni-Mo binary alloy, films with compositions in the range of (34at.%-69at.%)Mo are desirable with Ni-44at.%Mo having the optimum properties. Using this nanocomposite film for the fabrication of devices helps us to avoid any deformation, due to the differential stresses in release steps of fabrication, and to keep the optimum mechanical properties at the same time. As a proof-of-principle, therefore, we synthesized 50 nm thick single-anchored cantilevers having 400 nm and 800 nm width and different lengths (1-6 μm) out of Ni-44at.%Mo, the images of which are shown in Fig. 5.23. These devices have potential applications in cantilever-based sensors. These images show that there is almost no deformation in the cantilevers and their surfaces are very smooth.

To test the thermal stability of the cantilevers, differential scanning calorimetry (DSC) was performed on Ni-44at.%Mo films in an argon environment. The DSC result is given in Fig. 5.24. This result shows that the amorphous/nanocrystalline films are quite stable at temperatures below 400°C (in an argon atmosphere), after which phase transformation will take place inducing different stresses in the film. These results suggest the employment of this film, and any MEMS/NEMS devices fabricated of them, at high-temperature applications in vacuum or other neutral environments. It is clear that more experiments are needed to test the stability of the films and cantilevers when Oxygen and humidity are present.

Figures

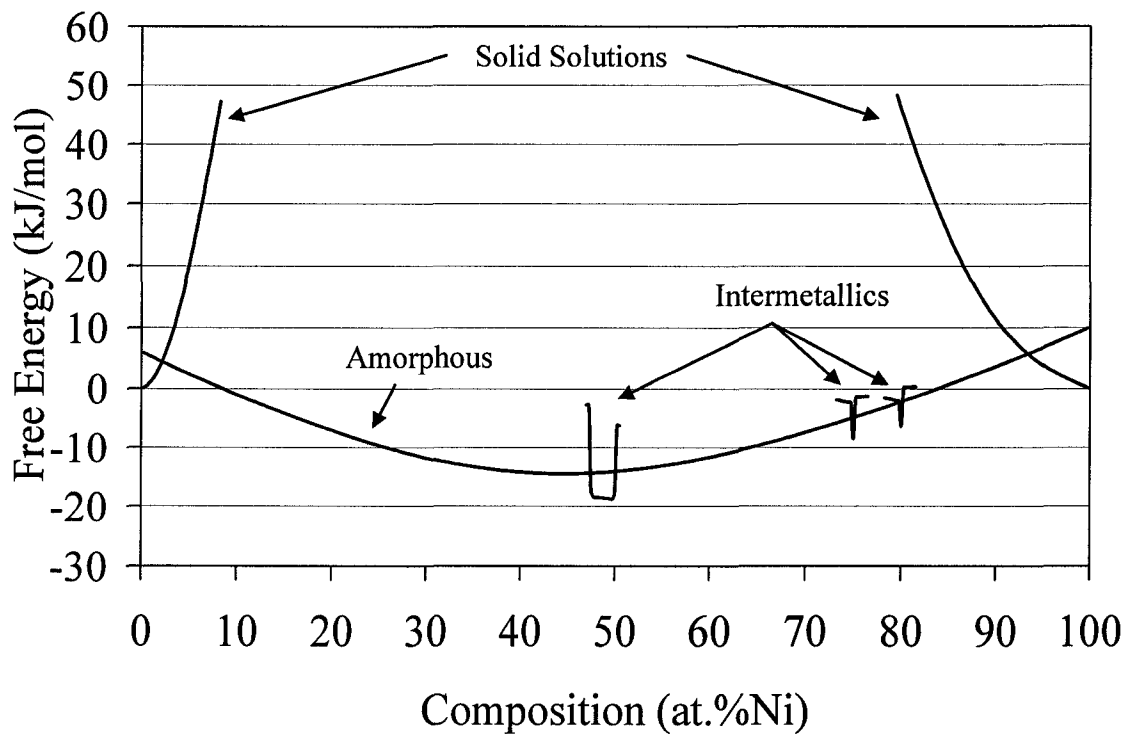


Figure 5.1: The modeled free energy curves of the metastable phases in Ni-Mo obtained using the Miedema's approach. The range of the amorphous formation can be predicted by drawing the tie-lines between the solid solution and amorphous phases showing an amorphous range of Ni-38at.%Mo to Ni-68at.%Mo.

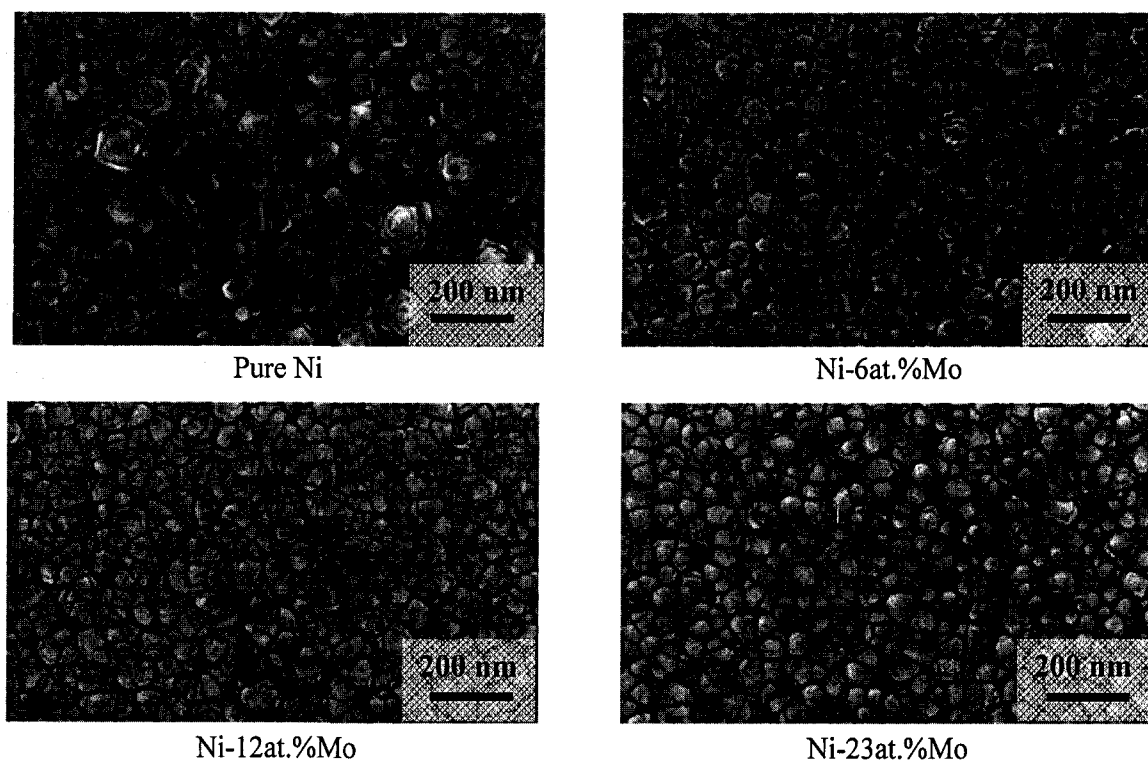


Figure 5.2: High-resolution scanning electron microscopy (SEM) images of the films from pure Ni to Ni-23at.%Mo.

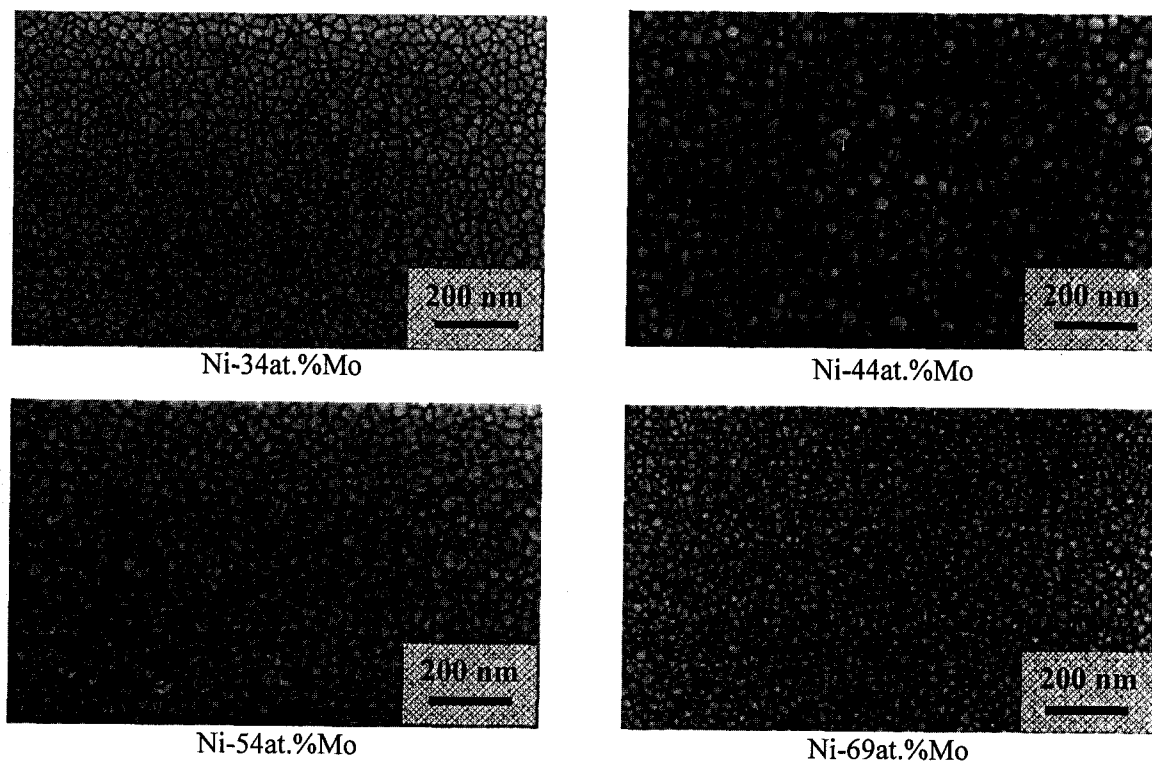
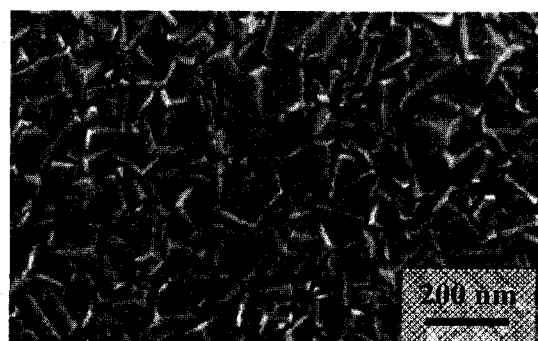


Figure 5.3: High-resolution scanning electron microscopy (SEM) micrographs of the films from Ni-34at.%Mo to Ni-69at.%Ni.



Ni-78at.%Mo



Ni-87at.%Mo



Ni-94at.%Mo



Pure Mo

Figure 5.4: High-resolution scanning electron microscopy (SEM) images of the films from Ni-78at.%Mo to pure Mo.

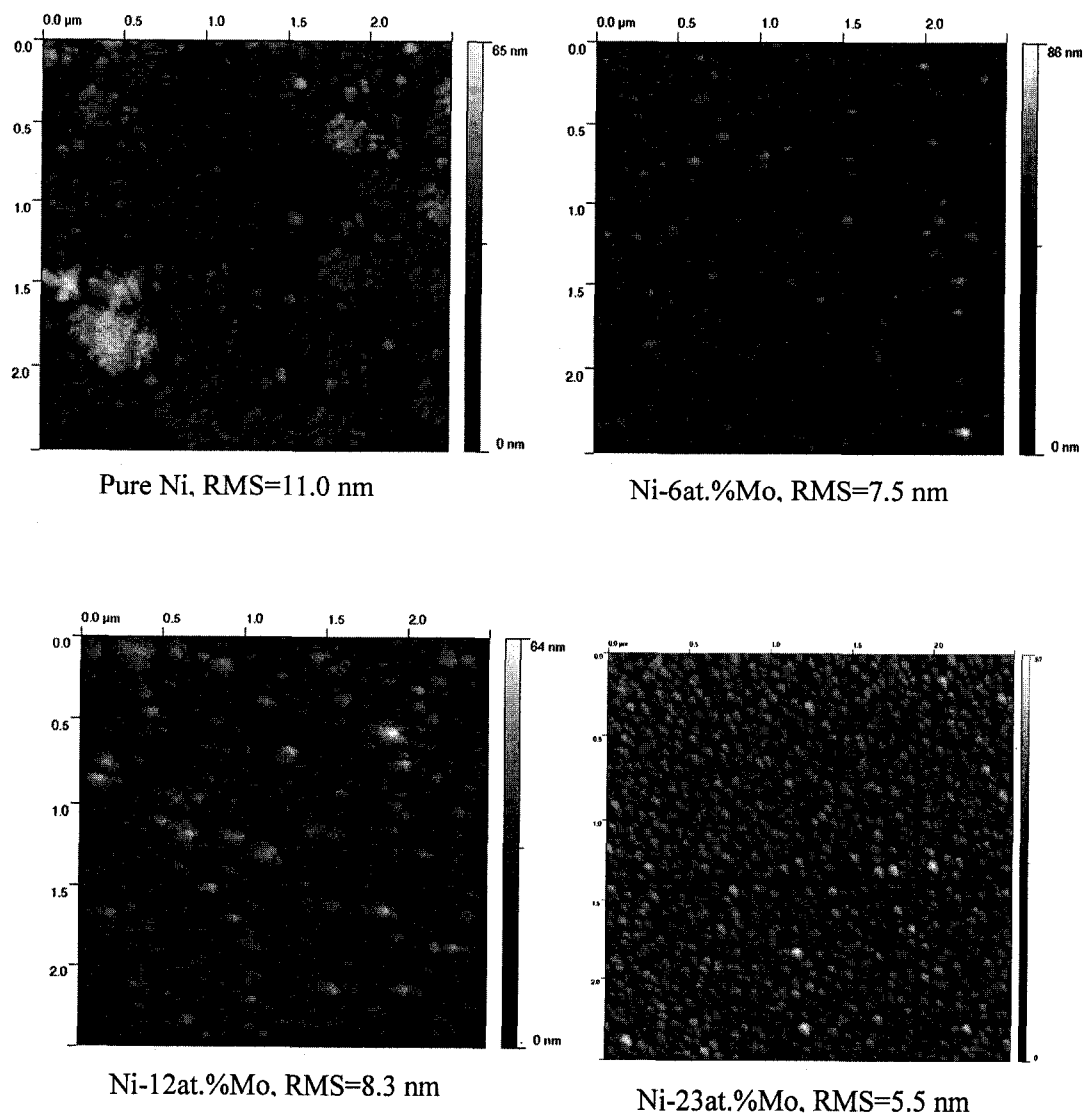


Figure 5.5: High-resolution atomic force microscopy (AFM) images of the films from pure Ni to Ni-23at.%Mo. The roughness decreases generally with Mo content. It should be mentioned that the roughness values are for comparison purposes between our fabricated films only; the actual roughness values might be higher than the present RMS values due to the detection limit of the tip.

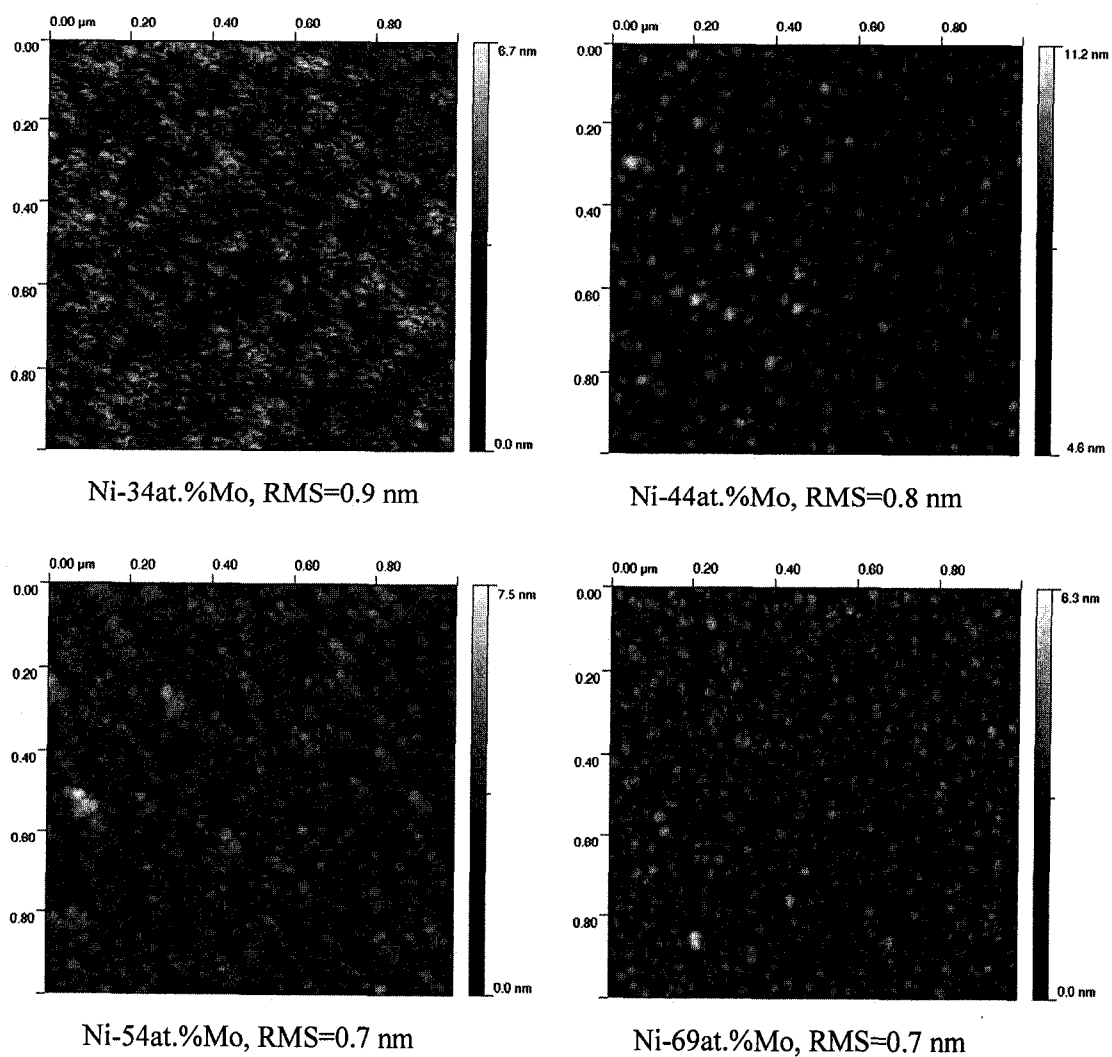


Figure 5.6: High-resolution AFM micrographs of the films from Ni-34at.%Mo to Ni-69at.%Ni. We can see that the surface of the films is very smooth (RMS<1 nm). It should be mentioned that the roughness values are for comparison purposes between our fabricated films only; the actual roughness values might be higher than the present RMS values due to the detection limit of the tip.

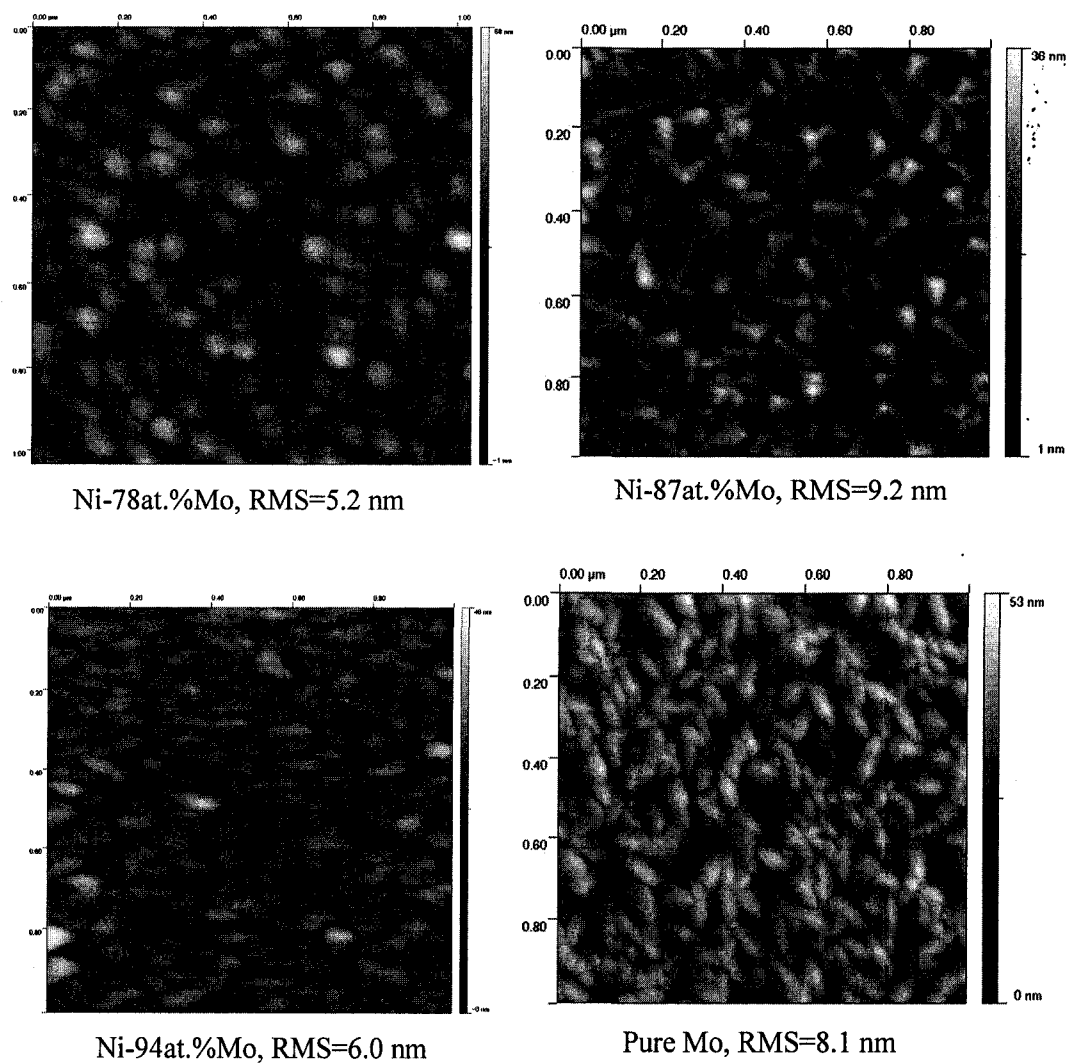
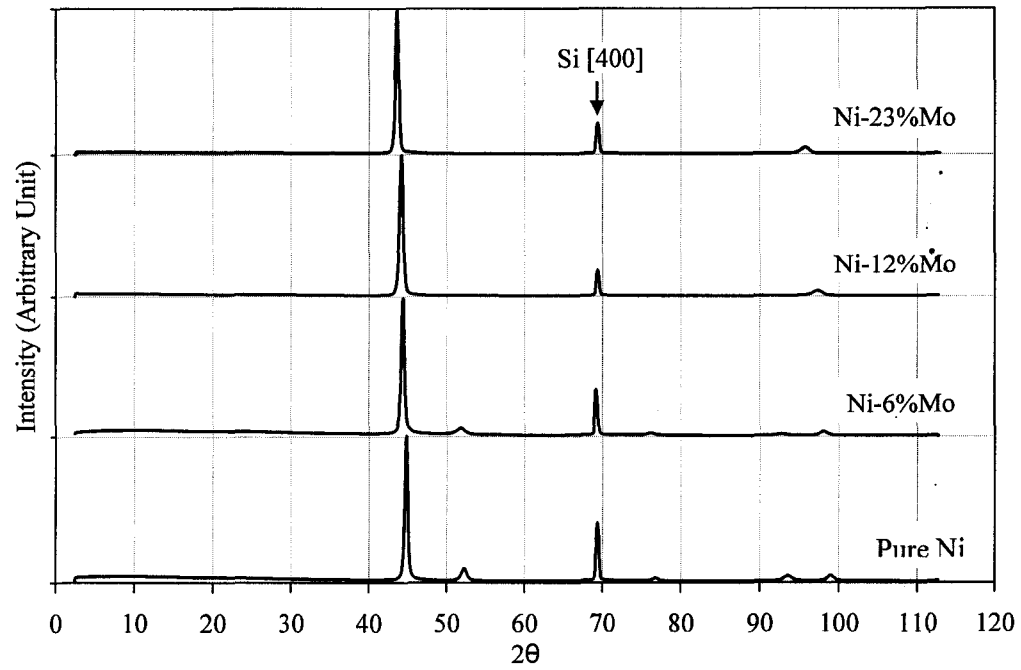
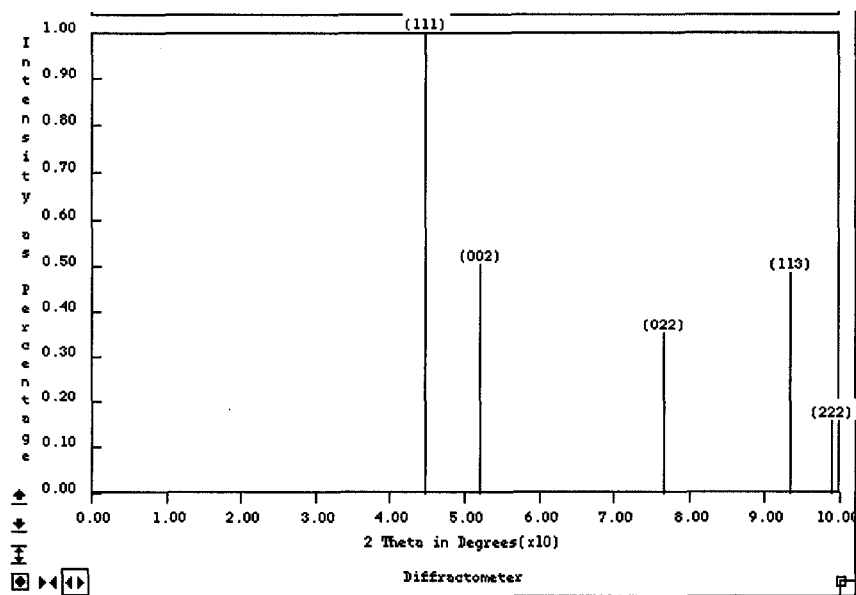


Figure 5.7: High-resolution AFM micrographs of the films from Ni-78at.%Mo to pure Mo. It can be observed that the roughness of the films increases generally with increasing of the Mo content. It should be mentioned that the roughness values are for comparison purposes between our fabricated films only; the actual roughness values might be higher than the present RMS values due to the detection limit of the tip.



(a)



(b)

Figure 5.8: (a) X-ray diffraction (XRD) spectra for the films from pure Ni to Ni-23at.%Mo together with the simulated indices using Desktop Microscopist commercial software, based on powder diffraction patterns (b). We can observe that for this composition range, the structure is fully FCC crystalline.

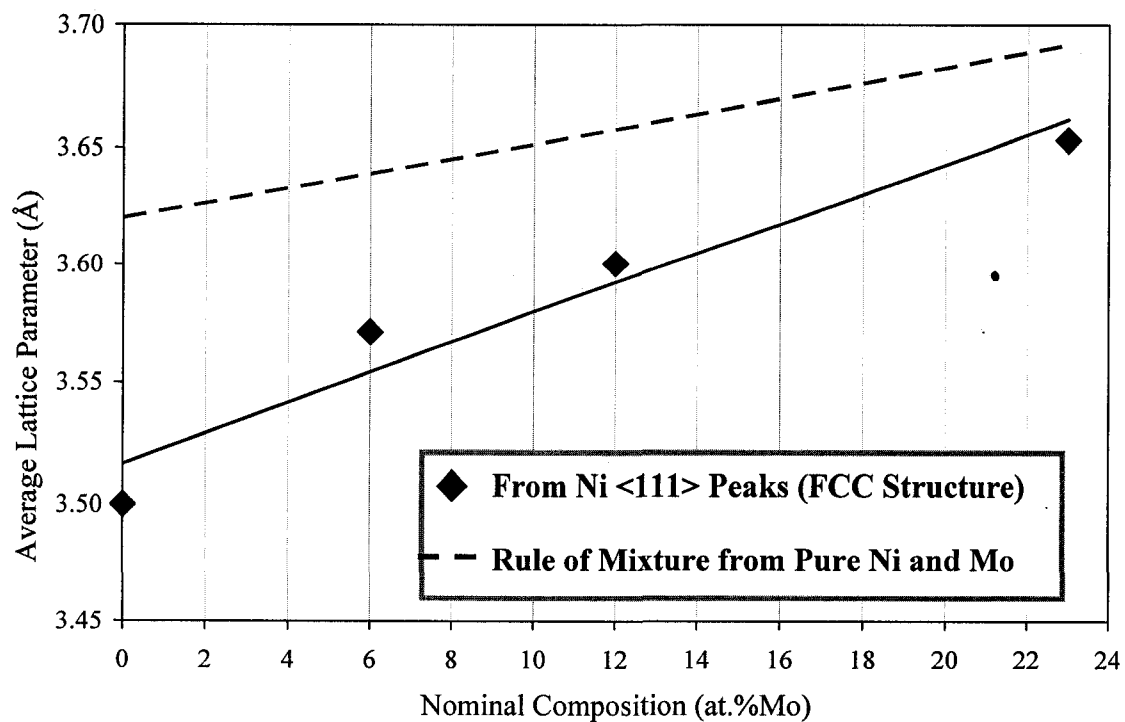


Figure 5.9: Vegard's law plot for the films from pure Ni to Ni-23at.%Mo. A line can be best fitted to the data showing that the rule of mixture is almost dominant for the data from the Ni peaks in Fig. 3.8. This plot shows the presence of a solid solution having stress for this region.

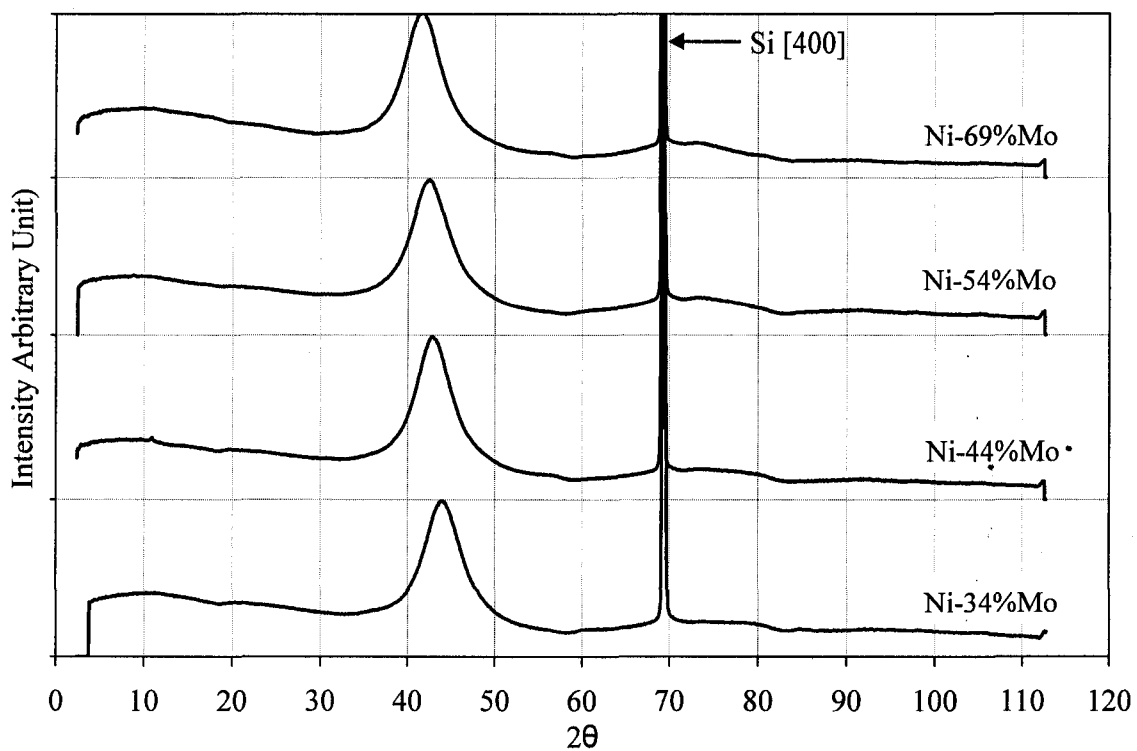
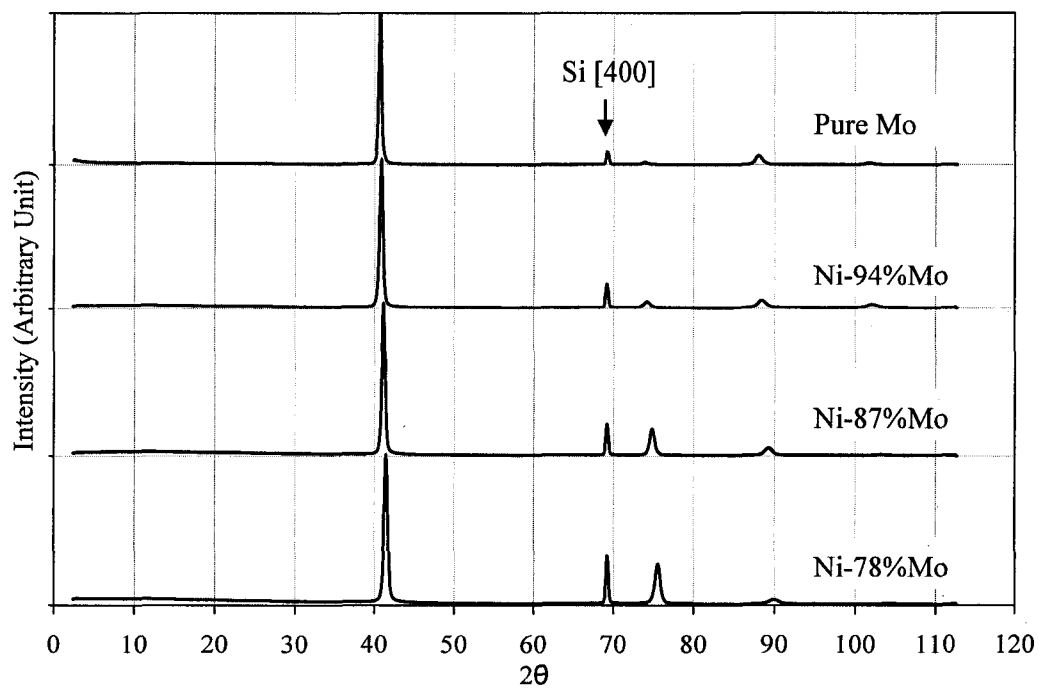
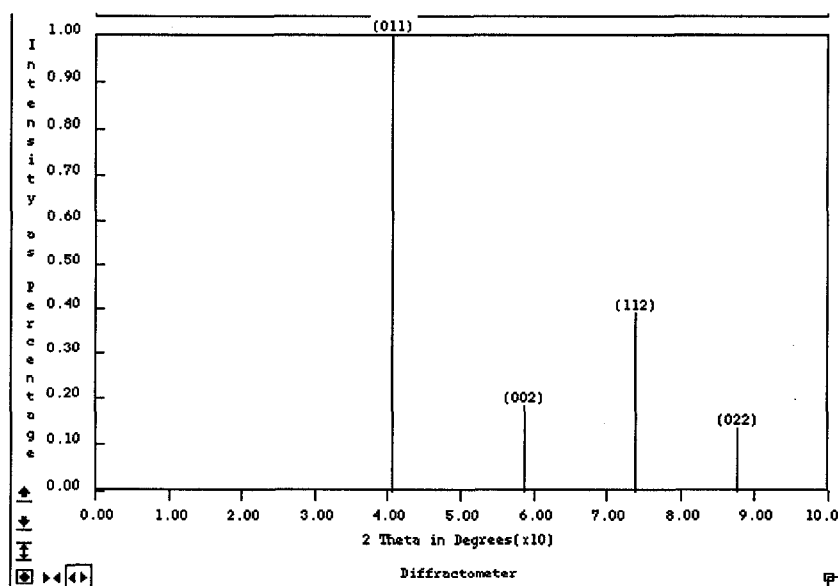


Figure 5.10: XRD signals for the middle range of composition from Ni-23at.%Mo to Ni-69at.%Mo. The peak broadening could be due to either amorphous, or nanocrystalline phase or both. The size of possible nanocrystallites was estimated to be from 1.5 nm to 2.5 nm using Sherrer equation.



(a)



(b)

Figure 5.11: (a) XRD spectra for the films from Ni-78at.%Mo to pure Mo together with the simulated indices, based on powder diffraction patterns (b). We can see for this range of composition that the structure is fully crystalline with a BCC structure.

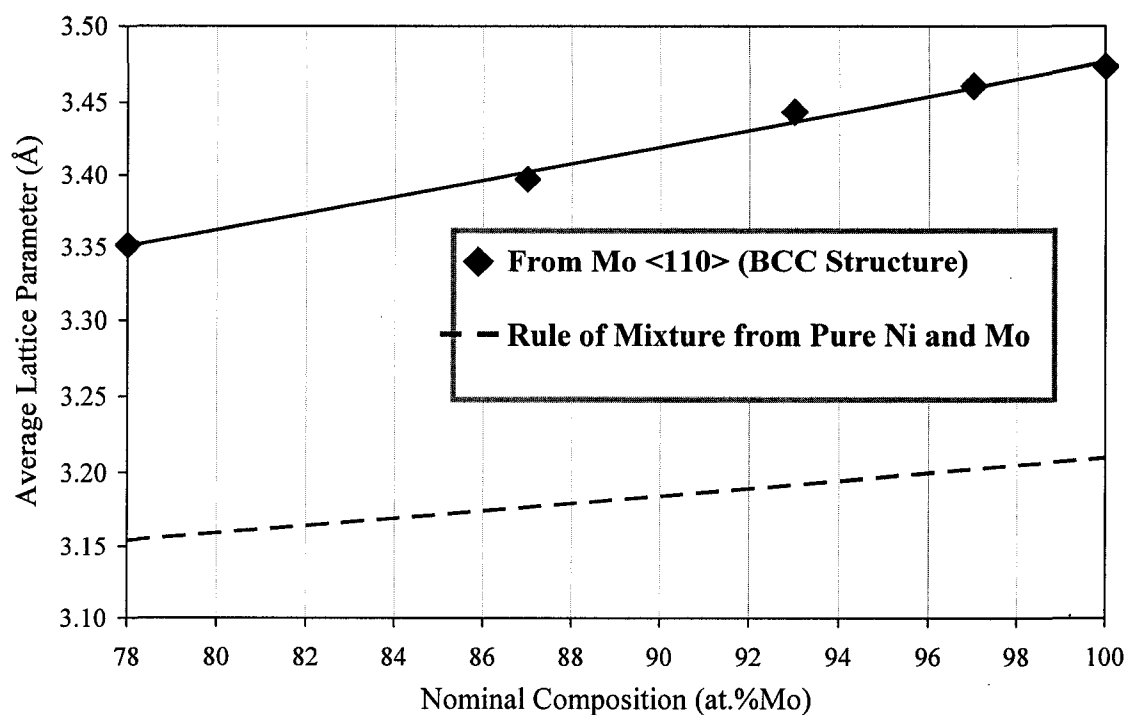


Figure 5.12: Vegard's law plot for the films from Ni-78at.%Mo to pure Mo. A line can be best fitted to the data showing that the rule of mixture is almost dominant. The difference between two lines can be due to the strain or lattice parameter difference in solid solution and pure elemental form.

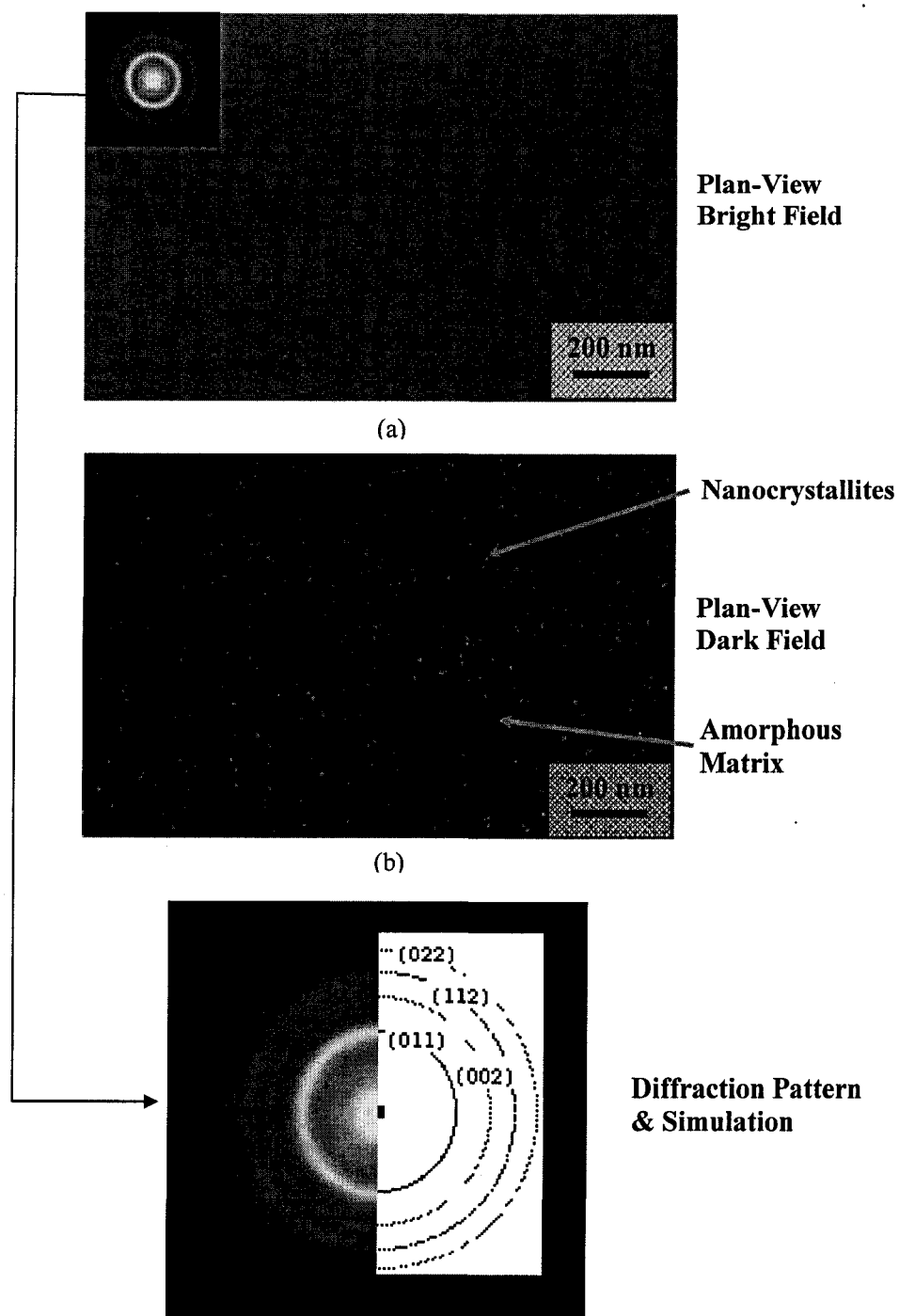


Figure 5.13: Plan-view bright field (a), plan-view dark field (b) and diffraction pattern (c) of the Ni-44at.%Mo film. We can see that the BCC nanocrystallites are distributed in an amorphous matrix.

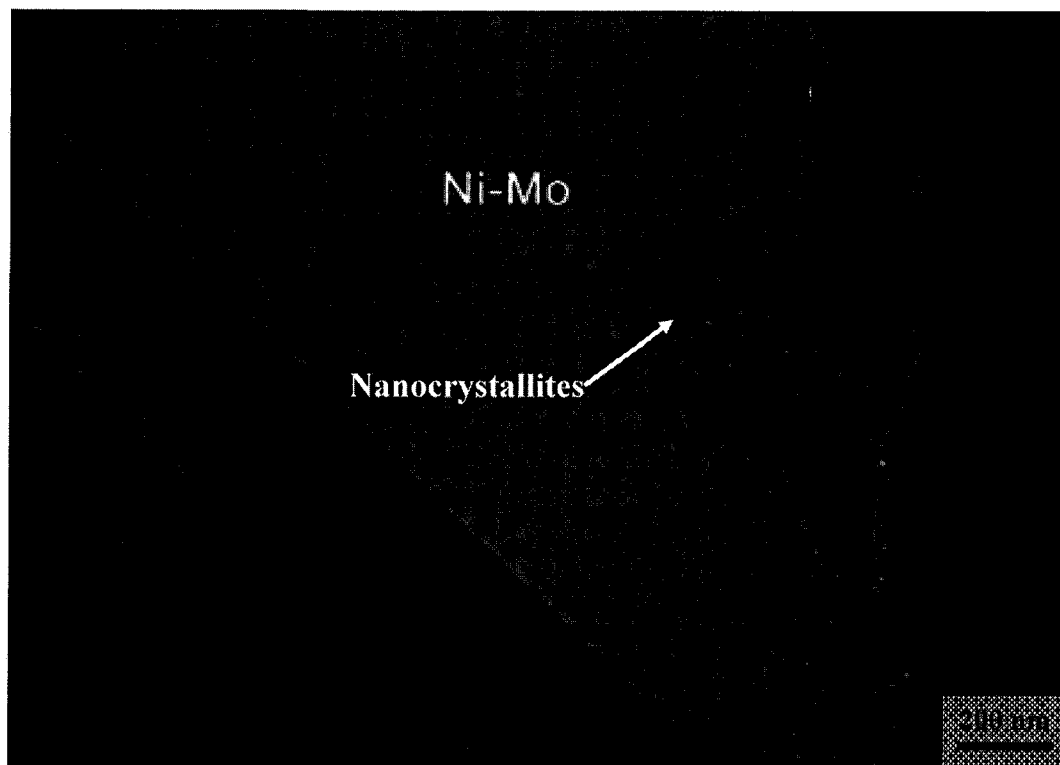
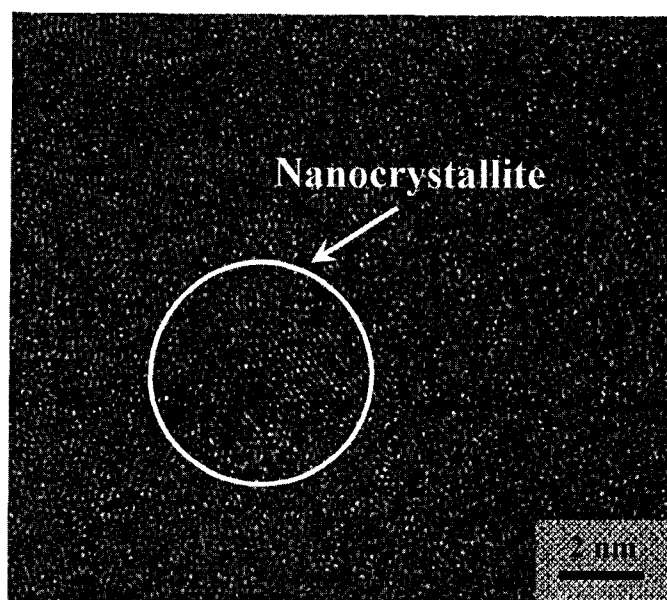
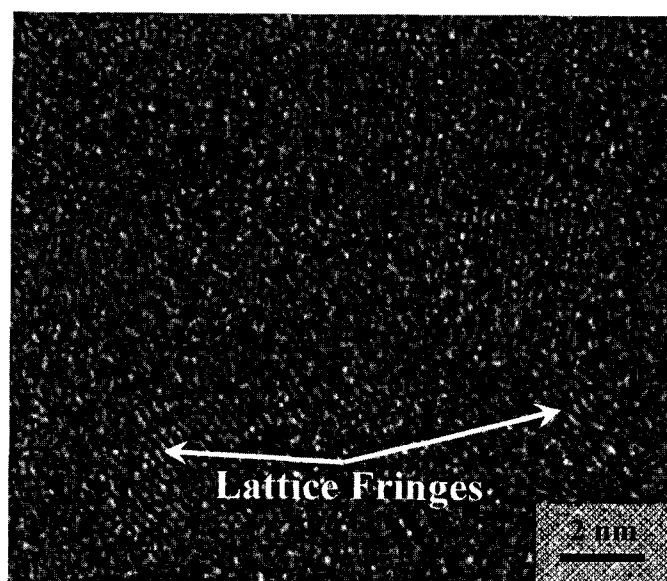


Figure 5.14: Cross-sectional dark field image of the Ni-44at.%Mo film. We can see from this image that the nanocrystallites are present and densely distributed through the thickness as well.



(a)



(b)

Figure 5.15: High resolution dark field TEM images of the Ni-44at.%Mo film at both plan- (a) and cross-sectional (b) views. The nanocrystallites and lattice fringes are shown on the images.

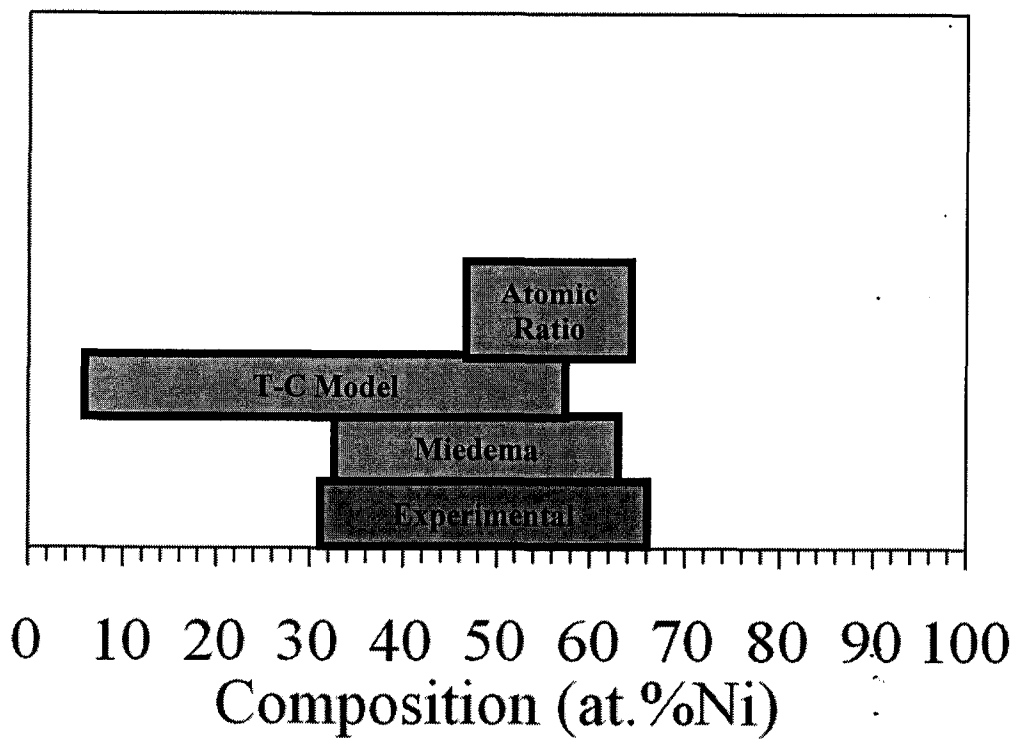


Figure 5.16: Schematic illustration of the results of different models for the prediction of the range of amorphous formation in Ni-Mo. The experimental range has been shown as well for comparison purposes. It can be seen that the closest prediction model to our experimental results is Miedema's model.

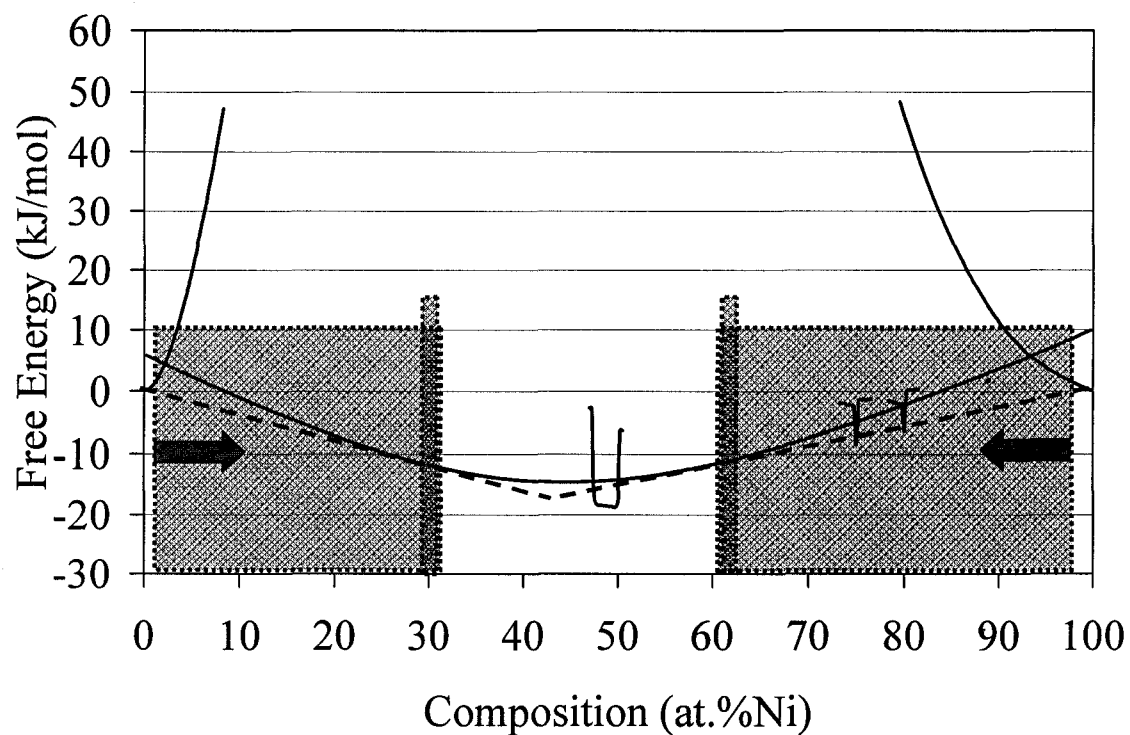
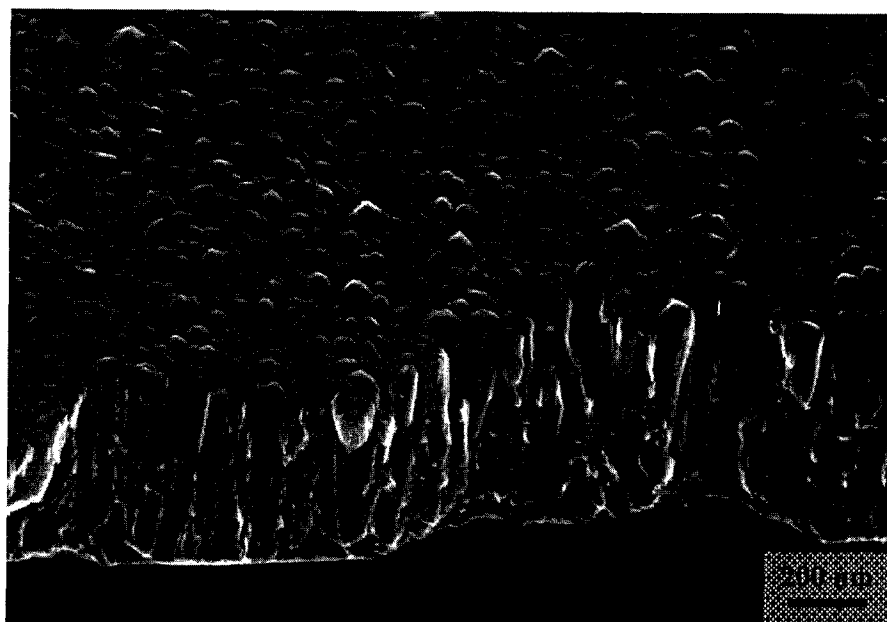
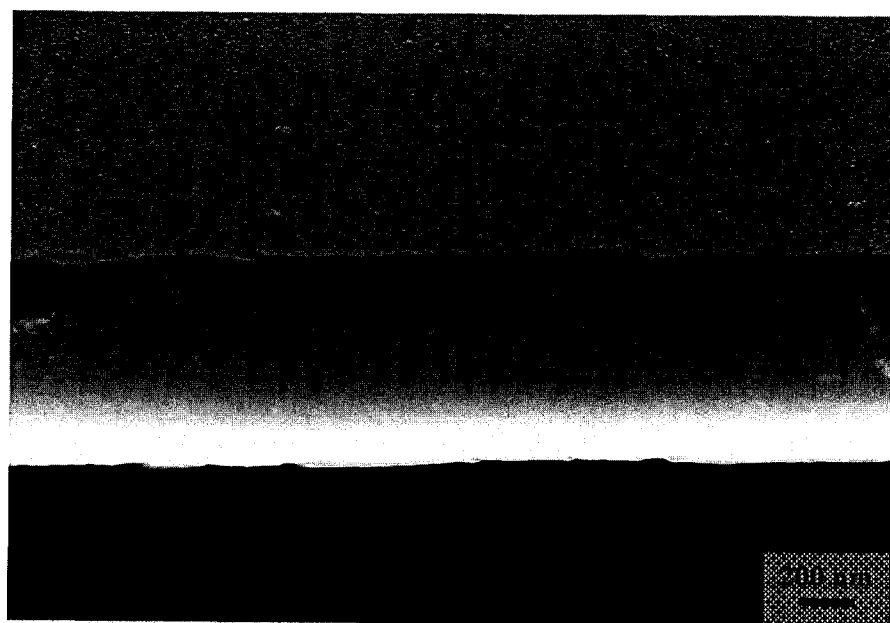


Figure 5.17: Schematic illustration of the kinetic effects on the prediction range of amorphous formation for Ni-Mo using Miedema's model. We can see that the two phase regions (light-gray squares) are narrowed (dark-gray squared) and pushed toward the center due to kinetic of sputtering. Also, the intermetallic phases predicted by the model were not kinetically accessible.

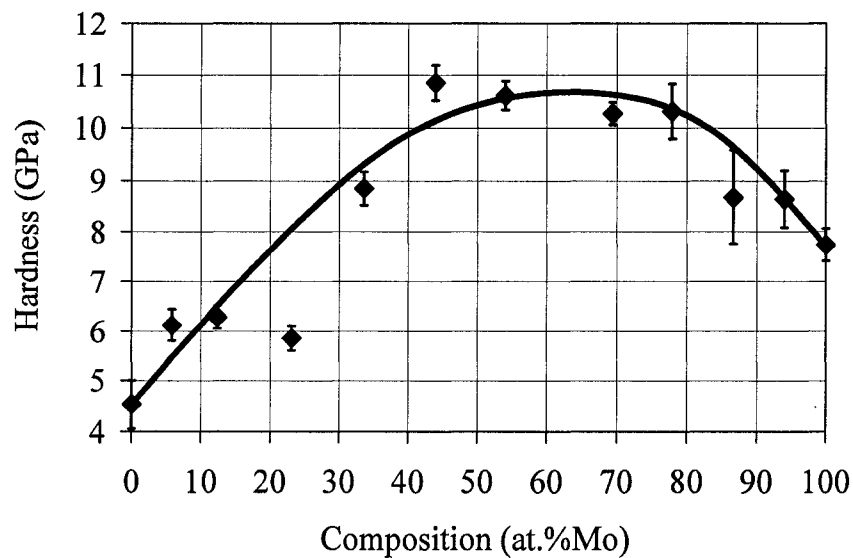


(a)

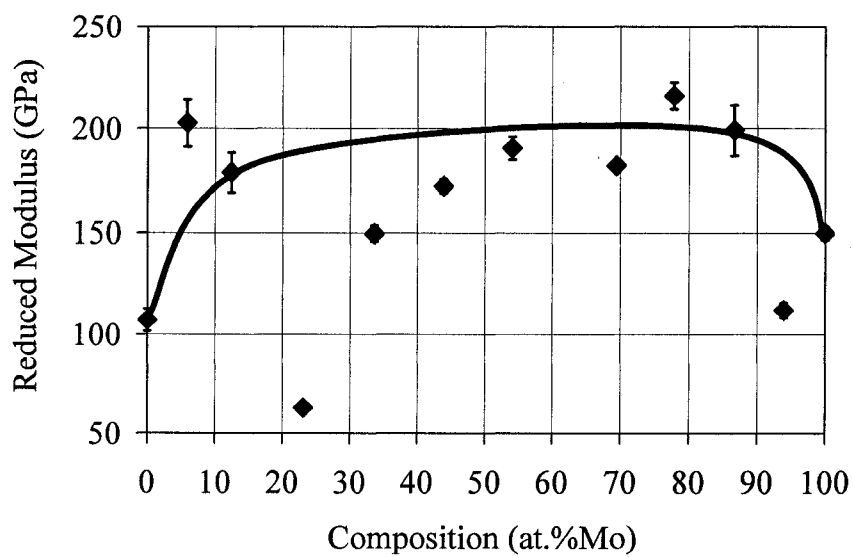


(b)

Figure 5.18: High-angle cross-sectional SEM images of pure Ni (a) and Ni-44at.%Mo (b) films. We can observe the competitive grain growth in pure Ni only.

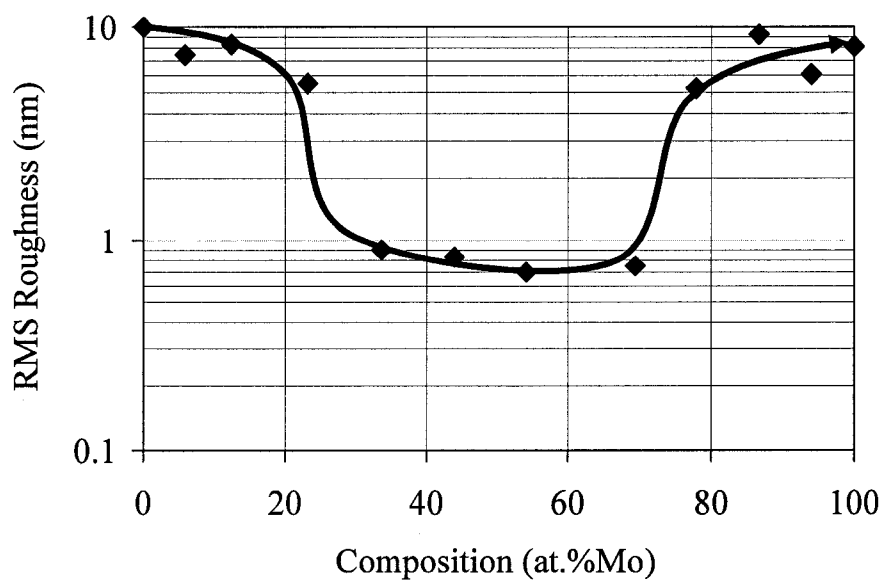


(a)

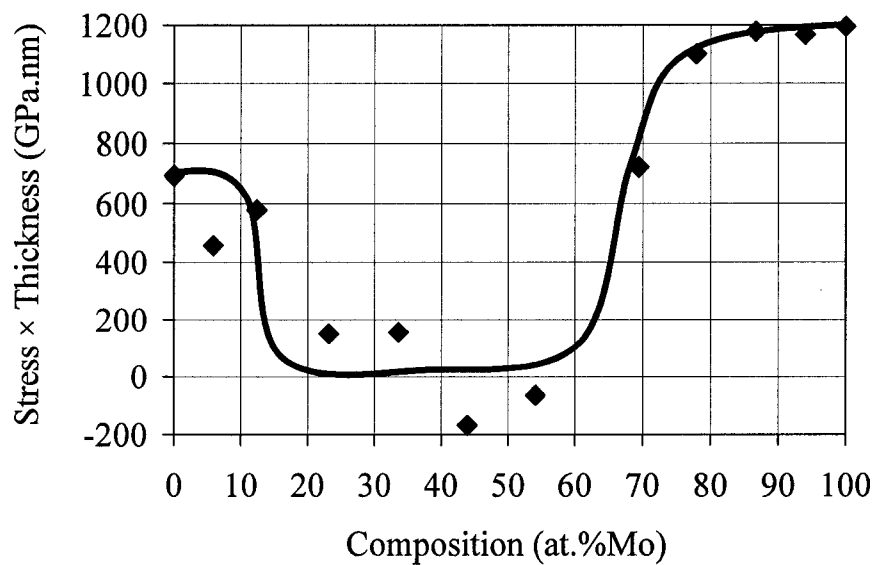


(b)

Figure 5.19: Nanoindentation results of Ni-Mo films: (a) nanohardness and (b) reduced modulus. We can see from these graphs that the hardness and modulus of the films are very high for the middle range of composition. Each datapoint is the average of 25 measurements. The lines are just to guide the eyes.



(a)



(b)

Figure 5.20: Physical properties of Ni-Mo films: (a) surface roughness and (b) intrinsic stress. We can see from these graphs that the surface of the films is very smooth and the films are almost free of stress for the middle range of composition (34at.%<Mo<69at.%). Each datapoint is the average of at least 3 measurements and the errorbars are in the size of symbols. The lines are just to guide the eyes.

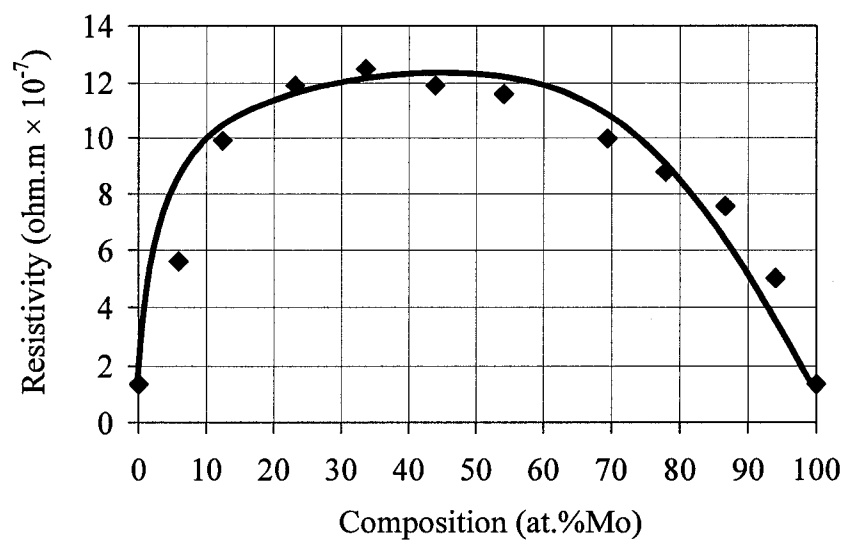


Figure 5.21: Resistivity data for the Ni-Mo films. We can see from the data that the conductivity is lower for the middle range but still in the range for metals. Each datapoint is the average of at least 3 measurements and the errorbars are in the size of symbols. The lines are just to guide the eyes.

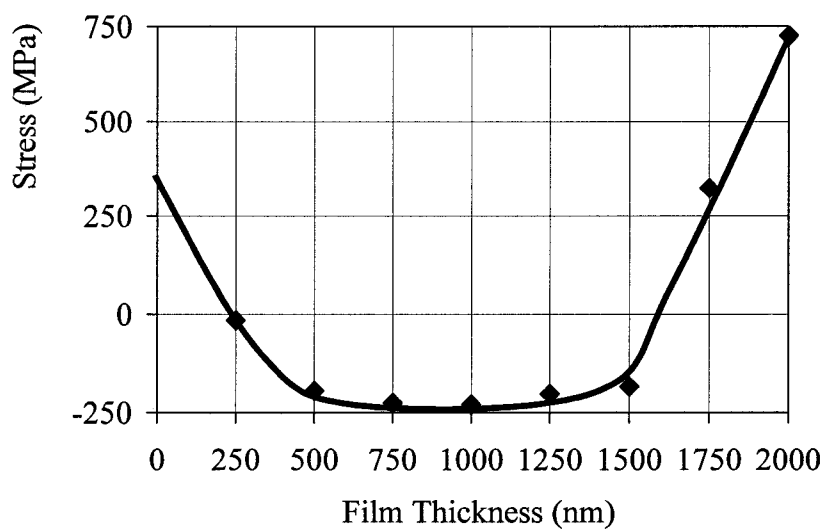


Figure 5.22: Effect of thickness on the intrinsic stress of Ni-44at.%Mo film. It can be observed that the stress is compressive for all of the thicknesses but showing a trend towards the positive stresses. Each datapoint is the average of at least 5 measurements and the errorbars are in the size of symbols. The line is just to guide the eyes.

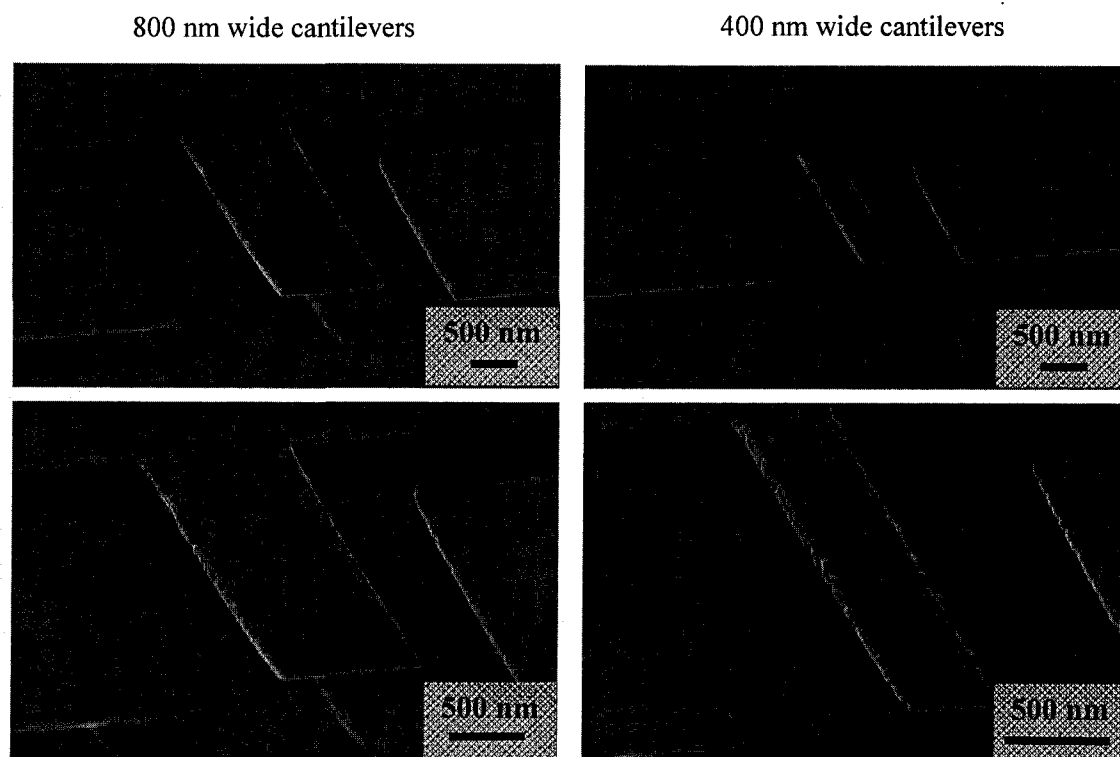


Figure 5.23: High-angle SEM images of the 50 nm thick Ni-44at.%Mo cantilevers having different lengths (400 nm and 800 nm wide).

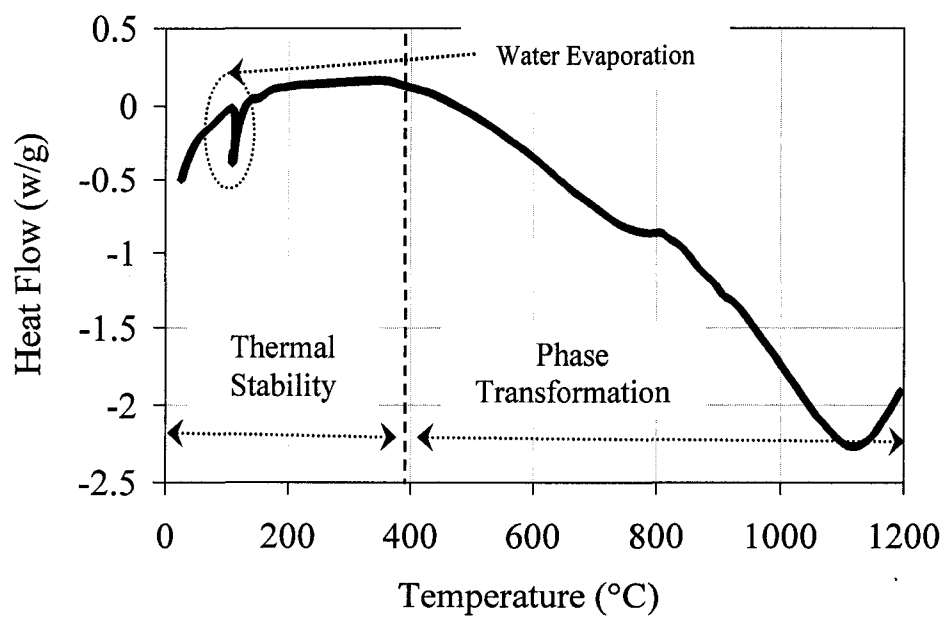


Figure 5.24: Differential scanning calorimetry (DSC) curve for the Ni-44at.%Mo film. We can see that the film is stable even at high temperatures in the order of 400 °C in argon atmosphere and used scanning rate (10 °C/min).

CHAPTER SIX: CONCLUSIONS AND RECOMMENDATIONS

6.1 Summary and Conclusions

Since competitive grain growth is considered mainly as the origin of high surface roughness and intrinsic stresses in metallic films, we designed the microstructure so that this type of growth was eliminated and a film with a very low stress and surface roughness was obtained. By the selection of right metallic elements (Ni and Mo) and stoichiometry, therefore, the polycrystalline microstructure could be substituted with a nanocomposite structure consisting of a nanocrystalline phase uniformly dispersed in an amorphous phase. In this way, the hardness and modulus increased while surface roughness and intrinsic stresses decreased dramatically.

One micrometer thick Ni-Mo films were fabricated by room-temperature co-sputtering from pure Ni and Mo targets to systematically study the microstructure and properties. The films with different compositions were synthesized from pure Ni to pure Mo by changing the Mo content in the binary alloy. The films were characterized using the conventional characterization techniques such as SEM, AFM, XRD and TEM and their physical properties were measured using nanoindentation and other methods for the measurement of thin film properties. From this investigation it was shown that from pure Ni to Ni-23at.%Mo, polycrystalline films with FCC crystal structure exist that grow columnar from the substrate. From pure Mo to Mo-22at.%Ni, on the other hand, the same competitive grain growth mode as the first region was observed; however, the crystal structure was found to be BCC. For the composition range between these two regions (34at.%<Mo<69at.%), our investigation resulted in a unique nanocomposite microstructure of Mo-rich nanocrystallites randomly and densely dispersed in a Ni-rich amorphous matrix. The Ni-44at.%Mo film had the optimum properties among all. This stress-free film showed an ultra-high nanoindentation hardness of 11 GPa and an order of magnitude reduction in surface roughness (0.8 nm) compared to those of pure Ni (4.5

GPa and 10 nm) and pure Mo (7.5 GPa and 8 nm), while maintaining the resistivity in metallic range. They were also stable at elevated temperatures in the order of 400°C (in argon environment).

As a proof-of-concept, we synthesized free-standing single-anchored 50 nm thick, 400-800 nm wide and 1-6 μm long cantilevers from Ni-44at.%Mo film (with optimum properties). To our knowledge, these are the smallest single-anchored metallic cantilevers fabricated so far which are ultra-hard, very smooth and almost free of stress. As a further step, we did a detailed study on the prediction of the range of amorphous formation in these films according to the different existing models. We found that the Miedema's thermodynamic model is the most successful one among all and predicts the amorphous formation range of Ni-38at.%Mo to Ni-68at.%Mo, which is in a good agreement with the amorphous range obtained from our experimental data (Ni-34at.%Mo to Ni-69at.%Mo).

6.2 Future Work

The future work of this research is going to be mainly focused on the following four subjects:

1. More detailed microstructure and phase studies:

More TEM and XRD analysis can be performed for the full range of compositions. The current TEM images and analysis were carried out for Ni-44at.%Mo, only. So, it is worth doing TEM for other compositions as well to verify the microstructure for all of the films. The XRD results and simulation of the peaks will be helpful in this study.

2. Mechanical testing:

As we discussed in the Introduction part, mechanical behaviour of thin films, especially the metallic films, plays an important role in their application to the

NEMS devices. We have measured the hardness and reduced modulus of the films from nanoindentation test. It should be a good idea to test the films for other mechanical properties such as ductility and both yield and ultimate strength since these properties are related to the resistance to fracture and plastic deformation when the film is under stress. Also, we recommend doing other mechanical tests on the films as well such as fatigue test, wear test and creep test since these tests can reveal the reliability of the films and fabricated devices when used as structural in-contact components in MEMS/NEMS applications.

3. Study the effect of thickness on physical properties:

It is well-known that thickness has a significant effect on stress state and surface roughness in polycrystalline films having columnar growth. We suggest confirming this issue for the polycrystalline regions of our films and investigating systematically the effect of thickness on the physical properties (hardness, modulus, roughness and stress) of the Ni-Mo films for the full range of composition. We have already confirmed that the state of stress is compressive for Ni-44at.%Mo when the thickness changes from 250 nm to 15000 nm. Also, understanding and modeling of the mechanism of thin film growth and stresses in the nanocomposite range can be interesting.

4. More thermal stability tests are needed:

We studied the thermal stability of the Ni-44at.%Mo film with one heating rate only. We recommend doing this test for all of the compositions and with different heating rates on freshly fabricated films using DSC. In this way, the glass transition temperature of the nanocomposite films is obtained as well. Also, phase identification using XRD and TEM after each phase transformation is recommended.

5. The proof-of-concept exists now:

Now, we have the proof-of-concept for this alloy (Ni-Mo). This alloy, therefore, can be used in different MEMS/NEMS applications wherever high conductivity is needed together with low surface roughness and high hardness. This alloy and the interpretation of the results can also be used for the design of other alloys such as Ni-W to increase the hardness and modulus to be fitted to different applications.

APPENDIX A: APPLICATION AND COMMERCIALIZATION PLAN

In previous chapters, we talked in details about the characteristics and different properties of Ni-Mo thin films we synthesized. Here we propose some potential applications for our alloy together with a cost estimation for the fabrication of cantilevers. Micro- and nano-electro mechanical elements can be used in potential applications such as biomedical chips, microfluidic chips, atomic force microscopy, etc. In some of these applications, the dynamic of the MEMS/NEMS structural components in liquid environments-such as blood in human body, oil in petroleum industries and other liquids in AFM applications-is extremely important. Single-clamped cantilevers as building blocks of the MEMS/NEMS devices are now the center of research in the area of micro and nanotechnology for their behavior in fluids. As a good example, in the petroleum industry measurement of the density and viscosity of petroleum reservoir fluids is required to determine the value of the produced fluid and production strategy. These thermo-physical properties are also useful for the design of separators and process equipment and to control production processes. To measure the density and viscosity of petroleum fluids, we require a transducer that can operate up to reservoir conditions and provide results with high accuracy. In the following section, we describe the basics for measurements of both density and viscosity of fluids in which a cantilever is immersed at the desired operating conditions with the application to oil industry.

A.1. Measurement of Liquid Properties Using the Cantilevers

In petroleum industry, we require to measure the thermo-physical properties of hydrocarbon reservoir fluids to determine flow in porous media and economically design the separation, treating and metering systems. The financial analysis that determines the potential for commercial benefits from extraction of naturally occurring hydrocarbon resources is obtained from the knowledge of the reservoir permeability, size and shape and the fluid thermo-physical properties. Any uncertainties in viscosity, density and phase behaviour of the petroleum fluid impact the financial analysis. To a

first approximation, measurement of density provides an estimate of the commercial value of the produced fluid while viscosity is an indicator of the ease, with which the fluid can be extracted from the reservoir. Viscosity is the single most important property to be measured [108].

A complete reservoir typically consists of a group of fluid-bearing layers separated by impermeable shells. The physical properties of the fluids can be determined from measurements performed on a sample extracted from each layer (usually referred to as a zone). The extraction is usually performed after the borehole has been drilled but before the production system, consisting of metal tubes surrounded by cement, is installed. From samples collected down-hole, all physical properties of the fluid can be determined in a laboratory at reservoir temperature and pressure. These measurements are combined with knowledge of the permeability and characteristics of the reservoir to perform analyses concerning the development of that petroleum reservoir. In the financial analysis, the thermo-physical properties and their uncertainties are usually considered to be lower in priority than the other items. However, uncertainties in the thermo-physical properties that arise from the operating conditions and sampling techniques can be significant and may be reduced by precise direct measurement. In general, measurements of density and viscosity with uncertainties of about $\pm 1\%$ and $\pm 10\%$, respectively, are considered adequate for value and extraction calculations with sufficient accuracy. Thus, methods that can provide in situ measurements of fluid density and viscosity with these uncertainties at reservoir conditions are desirable. In this way, we can reduce the time required for analysis and the systematic errors that arise from variations in chemical composition caused by transferring the fluids from one container to another and subsequent transportation.

There are numerous methods by which the density and viscosity of liquids can be measured. These methods have been reviewed by Johnson *et al.* [109]. Vibrating

objects including the vibrating wire and torsional viscometers were analyzed by Wagner and Kleinrahm [110] and Kuramoto *et al.* [111] for determining liquid densities. Other methods such as a vibrating tube [112] have been proposed to measure the viscosity. Also, some techniques other than a vibrating wire have been applied to measure both viscosity and density. We can refer to those methods that utilize ultrasonic plate waves [113] and bubble-rise speed [114] as examples in this category. Of the numerous methods that have been reported to measure density and viscosity, the most relevant to the transducer discussed above for our application are those that utilize a vibrating object of defined geometry and are fabricated using the microfabrication routes. To our knowledge, the instrument reported by Woodward [115] is the earliest example of a vibrating object that is conceptually similar to the device described here. They connected a 0.25 mm thick steel disk with a diameter of 5 mm to a clamp. The disk was forced to vibrate, and measurements of resonance were used to determine the product of the density and viscosity. Andrews and Harris [116] reported a transducer with two parallel plates, each supported by beams, that were oscillated normal to each other to determine the viscosity of gases. Martin *et al.* [117] used a plate wave resonator, fabricated on a silicon nitride membrane, to determine density. The ultrasonic plate wave resonator reported in Ref. 113 used a MEMS fabricated on a silicon carbide substrate. In addition to these devices, there are many other applications of cantilever beams developed from the devices used in atomic force microscopy [3] to the measurement of density and viscosity [118 - 122]. The width and length of the cantilevers vary from 2 to 200 μm with a thickness of order 1-3 μm . The instruments described in these references used a cantilever, exposed to air, to excite and detect the motion of a 50 μm diameter silica sphere immersed in a fluid. The sphere was connected to the cantilever by a 50 μm diameter silica rod. Cantilever beams have also been used to study the flow rates [123], measure the mechanical properties of electroplated gold films [124], determine Young's modulus [125] and form chemical [126, 127] and biochemical [128 - 130] sensors [131]. For the chemical and biochemical

sensors, the species is adsorbed onto the functionalized surface of the cantilever and is detected through either variation in resonance frequency due to an added mass or deflection of the beam arising from changes in surface stress [132, 133].

Choosing an appropriate sensor system for a specific application requires a good knowledge of design, implementation and fabrication method. Shieh *et al.* [134] have described systematic methods to select the most appropriate sensor for a particular application including devices that are based on coupled electromechanical phenomena. The essence of their approach relies on matching the desired sensor operating characteristics with the requirements of the desired applications. These philosophical processes are even more crucial when no off-the-shelf commercial sensor is available. In this case, a sensor must be developed by carefully matching the requirements to the potential characteristics of the sensor. The sensor we need for our specific application in petroleum industry, should be able to operate at reservoir conditions with accuracy in measurement of density and viscosity of about $\pm 1\%$ and $\pm 10\%$, respectively, that are adequate for calculations concerning the extraction of petroleum reservoir. Typically, the reservoir and production system have temperatures less than 473 K at pressures below 200 MPa [108]. In transducers that operate in the bore-hole, robustness is a superior priority to accuracy in the design process. The design, fabrication, and application of MEMS sensors has been discussed by Judy [135] while Werner and Fahrner [136] have reviewed devices, fabricated from silicon, that were specifically intended for operation at high temperature and in harsh environments similar to those found in petroleum reservoirs. As we found from our experimental results, Ni-Mo nanocomposite cantilevers with high hardness of 11 GPa and stability at temperatures below 400°C can be suitable candidates for this application.

To develop a method for the in situ and simultaneous measurement of density and viscosity, we can choose to construct a vibrating object. The transducer is then going to

be similar to a cantilever; i.e., a rectangular plate connected to a support along its edge. The density and viscosity of the fluid, in which the cantilever is immersed, can be determined from measurement of its frequency in motion. The design of the edge-supported vibrating plate densimeter/viscometer that will be described here is based on a magnetic field sensor originally reported by Donzier *et al.* [137]. A physical description of the motion of the cantilever in a fluid, which is used to obtain density and viscosity, requires a geometrically defined structure of known dimensions. When the sensor is formed by the methods of MEMS/NEMS, this requirement necessarily precludes the use of curved surfaces [108].

When the MEMS/NEMS fabricated device is placed in a fluid, to a first approximation, its resonance frequency (f_r) and quality factor ($Q = f_r/2g$) decrease with increasing density and viscosity, respectively. To define the parameter g , we have to determine the frequencies ($f_r - g$) and ($f_r + g$) above and below the resonance frequency (f_r) at which the measured amplitude is equal to $A_{max}/2^{1/2}$ where A_{max} is the maximum amplitude at f_r . The general effect of the fluid on the cantilever can be understood by two approximations. First, the resonance frequency decreases with increasing density because of added mass. Second, Q decreases as the viscosity increases owing to the shearing motion at the tip of the cantilever. Indeed, the methods of MEMS/NEMS we are dealing with here provide a means of constructing a densimeter that has a resonance frequency sensitive to the added mass of fluid in which it is immersed. This arises because the cantilever has a large surface-to-volume ratio.

Typically, petroleum reservoir fluids have densities in the range of 300 to 1300 kg.m⁻³ and viscosities between 0.05 to 1000 mPas. For Newtonian hydrocarbon liquids (fluids that are at a pressure of 0.1 MPa), the density is within the range of 700 to 1000 kg.m⁻³ while the viscosity is between 0.5 and 100 mPas. Newtonian fluids of known viscosities and densities, that include at least the ranges defined for hydrocarbon liquids, are

required for the laboratory evaluation of proposed in situ measurement techniques and calibration of viscometers and densimeters as a function of both temperature and pressure. Here, we are concerned with fluids that are Newtonian so that their viscosity is independent of the rate of shear. Non-Newtonian fluids can also be encountered in the production of petroleum, for example, drilling lubricants with additives such as sodium bentonite that increase the density. A transducer suitable for operation in both Newtonian and non-Newtonian fluids is hard to achieve.

A.1.1. Theory

Lindolm *et al.* [138] have presented theoretical descriptions of the elastic vibration of cantilever plates, but they did not provide working equations suitable for the plate in the application we are discussing here. However, some models have been proposed for the response of a cantilever beam immersed directly in a fluid [139-142]. The added mass model for the flexural response is based on an expression reported by Lindolm *et al.* [138] and has been extended to also include torsional oscillation. Cantilever beams, exposed to air, have also been used to actuate and detect the motion of a sphere immersed in a fluid. The response of the coupled cantilever and sphere has been interpreted with adaptations of the existing expressions for the oscillation of a sphere immersed in a fluid. Cumberbatch and co-workers presented a model for an elastic solid plate clamped on two opposite sides vibrating in a fluid to describe a commercially available densimeter [143].

To model the response of the edge-supported plate oscillating while immersed in a fluid, we can adopt an approach similar to that described in Refs 108 and 143 and model the edge-supported plate by decoupling the effects of viscosity and density so that the density is determined solely from the resonance frequency. We can also introduce another independent equation for the product of viscosity and density. Because of the secondary emphasis placed on accuracy during the design, we anticipate

the results we obtain with the assumptions and approximations we make will be adequate for the target accuracy.

The cantilever can be modeled as a one-dimensional beam (shown in Fig. A.1) supported at one end $y = z = 0$. The transverse displacement of the cantilever normal to the (x, z) plane is denoted, as shown in Fig. A.1, by

$$y = q(x, z, t) \quad (\text{A.1})$$

We assume that the longitudinal strain varies linearly across the cantilever's width and that the bending moment at any cross section is proportional to the local radius of curvature. We will consider only the mode of motion independent of x and will also ignore cantilever edge effects. The displacement (q) is governed by the Euler-Bernoulli bending theory of thin plates so that

$$F = \rho_s d \frac{\partial^2 q}{\partial t^2} + \frac{Ed^3}{12(1-\nu^2)} \nabla^4 q \quad (\text{A.2})$$

where F is the force per unit area applied normal to the cantilever, a denotes the cantilever length and b is the cantilever width. In Eq. (A.2), d is the cantilever's thickness, E is Young's modulus, ν is Poisson's ratio and ρ_s is the density of the cantilever material. We assume that the fluid is incompressible (so that $\nabla \cdot \mathbf{v} = 0$, where $\mathbf{v} = (u, v)$ is the fluid velocity) and that the flow is irrotational. At the supported end $z=0$; this implies that the oscillating cantilever has neither deflection nor bending. At the free end of the cantilever ($z=a$), there is neither bending nor shear force.

The fluid flow must now be determined so that the force per unit area on the cantilever (F) that appears in Eq. (A.2) can be calculated. In general, the fluid flow excited by the cantilever is extremely complicated but we can simply assume that both the cantilever thickness and the amplitude of the cantilever oscillations are small compared to its dimensions. In this way, the so-called "thin aerofoil theory" can be applicable. Essentially, this allows us to assume (a) that flow boundary conditions may be imposed

on $y = 0$ rather than on the actual moving surface of the vibrating cantilever and (b) that the fluid normal velocity component (v) is equal to the rate of change of displacement of the cantilever with respect to time on $y = 0$. This considerably simplifies the potential flow problem that must be solved. With the thin aerofoil theory assumptions, the velocity potential must satisfy the Laplace's equation in addition to the boundary conditions. The solution of Laplace's equation that satisfies the above equations is given and the expression for ρ_f is given by [108]

$$\rho_f = \frac{E v_n^5 d^3}{24(1-v^2)a^5 (2\pi f_{r,f})^2} - \frac{\rho_s d v_n}{2a} \quad (\text{A.3})$$

where ρ_f is the fluid density and $f_{r,f}$ is the resonance frequency of the cantilever immersed in fluid. In vacuum ($\rho_f = 0$) and Eq. (A.3) reduces to

$$f_r(p=0) = (2\pi)^{-1} \left[\frac{E v_n^4 d^2}{12(1-v^2)a^4 \rho_s} \right]^{1/2} \quad (\text{A.4})$$

for the resonance frequency $f_r(p=0)$. We recall that in Eqs. (A.3) and (A.4), a is the cantilever length and d is the cantilever thickness. Both Eqs. (A.3) and (A.4) require values of Young's modulus (E), Poisson's ratio (v) and density of the material (ρ_s). Finally, it should be noted that a similar analysis can be carried out if, instead of the pinned condition $\partial^2 q / \partial z^2 = 0$ at $z = 0$, a "clamped" condition $\partial q / \partial z = 0$ is used. The only difference to the end result is that an additional factor of 2 is present in the right-hand side of Eq. (A.3). The nature of sensor makes it hard to determine which of these two conditions is more appropriate. The best results are obtained when a combination of the two conditions is used.

With E , s , and r_s Eq. (A.4) gives $f_r(p=0)$ and Eq. (A.3) is used to estimate the resonance frequency when the cantilever is immersed in liquids. There are other aspects of the MEMS/NEMS design, fabrication, packaging and operation that can also contribute to the differences between the theoretical and observed resonance frequency.

These effects include the following: (1) surface roughness, (2) separation from stationary objects, (3) inertial response of the support and (4) assumptions used to obtain Eq. (A.3). Each of these will be discussed briefly below.

Equation (A.3) was derived assuming that the fluid-cantilever interface is perfectly smooth. In practice, this means a surface roughness much less than the viscous penetration depth, i.e. it is optically flat. According to our experimental results, the surface roughness of our Ni-Mo nanocomposite films is less than 1 nm and this assumption is quite valid. When the surface is rough, the fluid motion caused by the oscillation is more complicated than for a smooth surface and a range of additional mechanisms may occur that couple liquid motion and acoustic waves. Jain and Grimes [144] have considered (both experimentally and theoretically) the effect of surface roughness on liquid property measurements performed with mechanical oscillators. Their work suggests that, when the dimensions of the molecule are much less than those of the surface roughness, molecules are trapped on the surface and they act as both an additional mass and a viscous load. Thus, it may be possible to alter the response of an oscillator immersed in a fluid by engineering a specific roughness as we did with Ni-Mo. The dimensions of the molecules are of the order of 10^{-9} m and the surface roughness of Ni-Mo nanocomposite thin films are of the same order. The use of the assumptions, we made for the cantilever's motion and bending, forces the structure that holds the cantilever to recoil in response to the cantilever's motion. The cantilever's resonance frequency is thus coupled to the support. Increasing the mass of the cantilever's support reduces the coupling effect, which may result in a systematic error in density. Finite element analyses suggest using either the $n = 2$ mode $f_r(p = 0) \sim 27.5$ kHz (for which one side of the plate bends up while the other bends down) or the $n = 3$ mode $f_r(p = 0) \sim 70.3$ kHz (where the center of the plate moves upward while the sides move downward) might reduce this potential source of error. Since these motions result in insignificant movement of the center of mass, the structure supporting the plate does

not recoil so that the sensitivity of the tube's resonance frequency to the support is reduced. Preliminary investigations of the $n = 2$ and $n = 3$ modes provide promising results for density [108].

Models have been reported in the literature to obtain viscosity from the resonance frequency of a cantilever [115]. Here, we assume that the fundamental bending mode of the cantilever (the flexural mode) is simple harmonic and that the plate is immersed in an unbounded Newtonian fluid of viscosity, η_f , and density, ρ_f . The resonance quality factor, Q , is given by

$$Q^2 \propto (2\pi f_{r,f})^{-3} \eta_f \rho_f \quad (\text{A.5})$$

at the resonance frequency (f_r). We note parenthetically that a visco-elastic fluid will alter the elastic restoring force. Including $Q = f_r/2g$ at $p = 0$, the working equation for the fluid viscosity is given by

$$\eta_f = \frac{1}{\rho_f f_{r,f}^3} \left[\frac{2g_f}{f_{r,f}} - \frac{2g(p=0)}{f_r(p=0)} \right]^2 \quad (\text{A.6})$$

where $f_r(p=0)$ is the resonance frequency in vacuum; g_f is the resonance half-line width in the fluid, $g(p=0)$ in vacuum; and ρ_f is the fluid density obtained from Eq. A.3.

A.2. Cost Estimate of Cantilever's Fabrication

In this section, we will do a cost estimate for the fabrication of a Ni-Mo single-anchored cantilever according to our process flowchart (Section 4.4) and the available rates in the market [145]. It should be noted that the cost of materials characterization has not been included in this analysis. Also, it might be necessary to use a stack of cantilevers for different applications; the adjustments for the total cost should be made then. In the following table, the details of cost analysis are shown.

Table A.1: The details of cost estimate for the fabrication of a Ni-Mo single cantilever. If a stack of cantilevers is needed, the total cost should be considered. The analysis is based on the charge rates for industries. The prices are in Canadian Dollar.

Materials/Process	Material/Process Rate (\$/hour)	Time Required for the Process (hour)	Total Cost/Process (\$)
Silicon wafer	25	-	25
Wafer cleaning	110	0.5	55
Wafer oxidation	30	1	30
Dicing	30	0.5	15
Photoresist spinning	60	1	60
E-beam lithography	150	1	150
Wetdeck for developing	110	0.5	55
RIE	60	0.5	30
Sputtering	60	4	240
Release	150	0.5	75
Washing and drying	100	1	100
Total	-	10.5	835

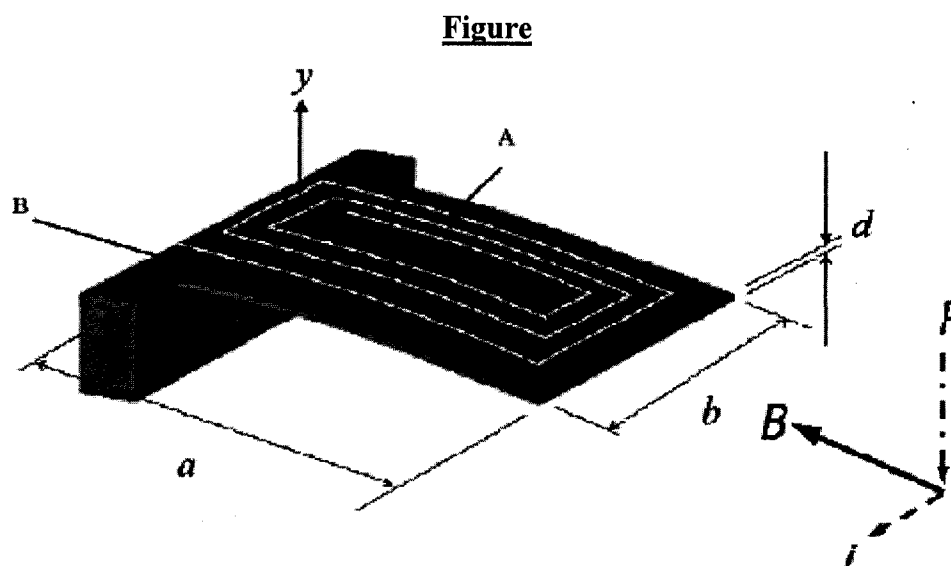


Figure A.1: Isometric projection of a NEMS cantilever of length a , width b , and thickness d illustrating the relative positions of the applied magnetic flux B , the direction of the current i through the coil **A** and the resulting force F creating a motion in the y plane detected by the Wheatstone bridge **B** [108].

References

1. M. Ohring, *Materials Science of Thin Films*, Academic Press, San Diego, USA, 1992.
2. Z. Lee, C. Ophus, L. M. Fischer, N. Nelson-Fitzpatrick, K.L. Westra, S. Evoy, V. Radmilovic, U. Dahmen and D. Mitlin, "Metallic NEMS components fabricated from nanocomposite Al-Mo films", *Nanotechnology* **17** (2006) 3063–3070.
3. G. Binnig, C. F. Quate and C. Gerber, "Atomic force microscope", *Phys. Rev. Lett.* **56** (1986) 930–933.
4. D. Rugar and P. Hansma, "Atomic force microscopy", *Phys. Today* **43** (1990) 23–30.
5. B. Ilic, H. G. Craighead, S. Krylov, W. Senaratne, C. Ober and P. A. Neuzil, "Attogram detection using nanoelectromechanical oscillators ", *J. Appl. Phys.* **95** (2004) 3694-3703.
6. H. D. Tong, F. C. Gielens, J. G. E. Gardeniers, H. V. Jansen, J. W. Berenschot, M. J. de Boer, J. H. de Boer, C. J. M. van Rijn and M. C. Elwenspoek, "Microsieve supporting palladium-silver alloy membrane and application to hydrogen separation ", *J. Microelectromech. Syst.* **14** (2005) 113-124.

-
7. M. Gupta, V. K. Rathi, R. Thangaraj, O. P. Agnihotri and K. S. Chari, "The preparation, properties and applications of silicon-nitride thin-films deposited by plasma-enhanced chemical vapour-deposition", *Thin Solid Films* **204** (1991) 77-106.
 8. M. M. Farooqui and A. G. R. Evans, "Silicon sensors with integral tips for atomic force microscopy: A novel single-mask fabrication process", *J. Micromech. Microeng.* **1** (1993) 8-12.
 9. A. Folch, M. S. Wrighton and M. A. Schmidt, "Microfabrication of oxidation-sharpened silicon tips on silicon nitride cantilevers for atomic force microscopy", *J. Microelectromech. Syst.* **6** (1997) 303-306.
 10. M. Hebbachi, "Nanoindentation: hardness and phase transition in silicon", *Mater. Sci. Eng. A* **387** (2004) 743-748.
 11. A. Chand, M. B. Viani, T. E. Schäffer and P. K. Hansma, "Microfabricated small metal cantilevers with silicon tip for atomic force microscopy", *Journal of Microelectromechanical Systems* **9** (2000) 112-116.
 12. J. J. Gill, D. T. Chang, L. A. Momoda and G. P. Carman, "Manufacturing issues of thin film NiTi microwrapper", *Sens. Actuators A* **93** (2001) 148-156.
 13. A. Inoue and K. Hashimoto (Eds.), *Amorphous and Nanocrystalline Materials: Preparation, Properties, and Applications*, Springer, Berlin, Germany, 2001.

-
14. F. R. de Boer, R. Boom, W. C. M. Mattens and A. R. Miedema, *Cohesion in Metals-Transition Metal Alloys*, Elsevier Scientific Pub. Co., New York, USA, 1988.
 15. T. Egami and Y. Waseda, "Atomic size effect on the formability of metallic glasses", *J. Non-Cryst. Solids* **64** (1984) 113-134.
 16. L. Fachun, L. Limei, H. Zhigao, G. Rongquan and Q. Yan, "Effect of thickness on the structure, morphology and optical properties of sputter deposited Nb₂O₅ films", *Appl. Surf. Sci.* **253** (2006) 1801-1805.
 17. M. Aguilar, P. Quintana and A. I. Oliva, "Thickness-stress relations in aluminum thin films ", *Mater. Manuf. Processes* **17** (2002) 57-65.
 18. Hiroaki Okamoto, *Phase Diagrams for Binary Alloys*, ASM International, Ohio, USA, 2000.
 19. T. B. Massalski T B (Ed), *Binary Alloy Phase Diagrams*, Vol. 2, ASM International, Materials Park, Ohio, 2nd Edition, 1990.
 20. A. R. Miedema, F. de Chatel and F. R. de Boer, "Cohesion in alloys-fundamentals of a semi-empirical model ", *Physica B* **100** (1980) 1-28.
 21. R. A. Mirshams and P. Parakala, "Nanoindentation of nanocrystalline Ni with geometrically different indenters", *Mater. Sci. Eng. A* **372** (2004) 252-260.

-
22. T. Du, A. Vijayakumar, K. B. Sandaram and V. Desai, "Chemical mechanical polishing of nickel for applications to MEMS devices ", *Microelectron. Eng.* **75** (2004) 234-241.
23. K. Kataoka, S. Kawamura, T. Itoh, K. Ishikawa, H. Honma and T. Suga, "Electroplating Ni micro-cantilevers for low contact-force IC probing", *Sens. Actuators A* **103** (2003) 116-121.
24. W. H. Teh, J. K. Luo, M. A. Graham, A. Pavlov and C. G. Smith, "Near-zero curvature fabrication of miniaturized micromechanical Ni switches using electron beam cross-linked PMMA", *J. Micromech. Microeng.* **13** (2003) 591-598.
25. D. E. Brown, M. N. Mahmood, M. C. M. Man and A. K. Turner, "Preparation and characterization of low overvoltage transition metal alloy electrocatalysts for hydrogen evolution in alkaline solutions", *Electrochem. Acta* **29** (1984) 1551-1556.
26. M. L. Trudeau, J. Y. Huot and R. Schulz, "Mechanically alloyed nanocrystalline Ni-Mo powders: A new technique for producing active electrodes for catalysis", *Appl. Phys. Lett.* **58** (1991) 2764-2766.
27. A. Kawashima, E. Akiyama, H. Habazaki and K. Hashimoto, "Characterization of sputter-deposited Ni-Mo and Ni-W alloy electrocatalysts for hydrogen evolution in alkaline solution", *Mater. Sci. Eng. A* **226-228** (1997) 905-909.
28. A. Inoue and K. Hashimoto (Eds.), *Amorphous and Nano-crystalline Materials*, Springer, Berlin, Germany, 2001.

-
29. R. Schulz, J. Y. Huot, M. L. Trudeau, L. Dignard-Bailey and Z. H. Yan, "Nanocrystalline Ni-Mo alloys and their application in electrocatalysis", *J. Mater. Res.* **9** (1994) 2998-3008.
30. B. Zhao, F. Zeng and F. Pan, "Formation of metastable alloy film in the Ni-Mo binary system by ion-beam-assisted deposition", *Appl. Phys. A* **77** (2003) 523-528.
31. W. Zhang, X. S. Zhang, D. H. Yang and Q. J. Xue, "Sliding wear study of ion-beam mixing Ni-Mo multilayer films on steel", *Wear* **197** (1996) 228-232.
32. C. V. Thompson, "Structure evolution during processing of polycrystalline films", *Annu. Rev. Mater. Sci.* **30** (2000) 159-190.
33. A. W. Neumann and J. K. Spelt (eds.), *Advanced Surface Thermodynamics*, Marcel Dekker, New York, USA, 1996.
34. D. A. Porter, *Phase Transformation in Metals and Alloys*, Chapman and Hall, London, UK, 1992.
35. W. D. Nix and B. M. Clemens, "Crystallites coalescence: a mechanism for intrinsic tensile stresses in thin films", *J. Mater. Res.* **14** (1999) 3467-3473.
36. R. W. Hoffman, "Stresses in thin films: the relevance of grain boundaries and impurities", *Thin Solid Films* **34** (1976) 185-190.

-
37. W. D. Nix and B. M. Clemens, "Stress distributions and thin film mechanical properties", *Surf. Interface Anal.* **3** (1981) 62-66.
38. R. Abermann, "Measurements of the intrinsic stresses in thin metal films", *Vacuum* **41** (1990) 1279-1282.
39. M. D. Thouless, "Modeling the development and relaxation of stresses in films", *Annu. Rev. Mater. Sci.* **25** (1995) 69-96.
40. A. van der Drift, "Evolutionary selection, a principle governing growth orientation in vapor-deposited layers", *Philips Res. Repts.* **22** (1967) 267-288.
41. R. P. U. Karunasiri, R. Bruisma and J. Rudnick, "Thin-film growth and shadow instability", *Phys. Rev. Lett.* **62** (1989) 788-791.
42. J. Krug, "Origins of scale invariance in growth processes", *Adv. Phys.* **46** (1997) 139-282.
43. D. J. Srolovitz, "Grain growth phenomena in films: A Monte Carlo approach", *J. Vac. Sci. Technol. A* **4** (1986) 2925-2931.
44. C. Streng, K. Samwer and S. G. Mayr, "Surface smoothing and pattern formation in the transient region of compositionally modulated amorphous metallic alloy films: Experiment versus theory", *Phys. Rev. B* **73** (2006) 1041071-1041075.

-
45. S. Vauth, C. Streng, S. G. Mayr and K. Samwer, "Growth of vapor-deposited amorphous $Zr_{65}Al_{7.5}Cu_{27.5}$ films under oblique particle incidence investigated by experiment and simulation", *Phys. Rev. B* **68** (2003) 2054251-2054258.
46. S. G. Mayr, M. Moske and K. Samwer, "Identification of key parameters by comparing experimental and simulated growth of vapour-deposited amorphous $Zr_{65}Al_{7.5}Cu_{27.5}$ films", *Phys. Rev. B* **60** (1999) 16950-16955.
47. M. Raible, S. J. Linz and P. Hanggi, "Amorphous thin-film growth: Minimal Deposition equation", *Phys. Rev. E* **62** (2000) 1691-1705.
48. M. Raible, S. G. Mayr, S. J. Linz, M. Moske, P. Hanggi and K. Samwer, "Amorphous thin-film growth: Theory compared with experiment", *Europhys. Lett.* **50** (2000) 61-67.
49. M. Raible, S. J. Linz and P. Hanggi, "Amorphous thin film growth-Effects of density inhomogeneities", *Phys. Rev. E* **64** (2001) 0315061-03150611.
50. B. Reinker, M. Moske and K. Samwer, "Kinetic roughening of amorphous $Zr_{65}Al_{7.5}Cu_{27.5}$ films investigated *in situ* with scanning tunnelling microscopy", *Phys. Rev. B* **56** (1997) 9887-9893.
51. S. G. Mayr and K. Samwer, "Model for intrinsic stress formation in amorphous thin films", *Phys. Rev. Lett.* **87** (2001) 0361051-0361054.

-
52. L. B. Freund and S. Suresh, *Thin Film Materials: Stress, Defect Formation and Surface Evolution*, Cambridge University Press, Cambridge, England, 2003.
53. Y. Pauleau, "Generation and evolution of residual stresses in physical vapour-deposited thin films", *Vacuum* **61** (2001) 175-181.
54. P. R. Guduru, E. Chason and L. B. Freund, "Mechanics of compressive stress evolution during thin film growth", *J. Mech. Phys. Solids* **51** (2003) 2127-2148.
55. R. Abermann and R. Koch, "The internal stress in thin silver, copper and gold films", *Thin Solid Films* **129** (1985) 71-78.
56. R. Koch and R. Abermann, "Microstructural changes in vapor-deposited silver, copper and gold films investigated by internal stress measurements", *Thin Solid Films* **140** (1986) 217-226.
57. R. C. Cammarata, T. M. Trimble and D. J. Srolovitz, "Surface stress model for intrinsic stresses in thin films", *J. Mater. Res.* **15** (2000) 2468-2474.
58. L. B. Freund and E. Chason, "Model for stress generated upon contact of neighbouring islands on the surface of a substrate", *J. Appl. Phys.* **89** (2001) 4866-4873.
59. R. W. Hoffman, "Stress distributions and thin film mechanical properties", *Surf. Interface Anal.* **3** (1981) 62-66.

-
60. A. L. Shull and F. Spaepen, "Measurements of stress during vapour deposition of copper and silver thin films and multilayers", *J. Appl. Phys.* **80** (1996) 6243-6256.
61. G. Hass and R. E. Thun (Eds.), *Physics of Thin Films*, Academic Press, New York, Volume 3, 1966, 211-274.
62. R.W. Hertzberg, *Deformation and Fracture Mechanics of Engineering Materials*, John Wiley, New York, 1996.
63. F. A. Doljack and R. W. Hoffman, "The origins of stress in thin nickel films", *Thin Solid Films* **12** (1972) 71-74.
64. E. Chason, B. W. Sheldon, L. B. Freund, J. A. Floro and S. J. Hearne, "Origin of compressive residual stress in polycrystalline thin films", *Phys. Rev. Lett.* **88** (2002) 1561031-1561034.
65. B. W. Sheldon, A. Ditkowski, R. Beresford, E. Chason and J. Rankin, "Intrinsic compressive stress in polycrystalline films with negligible grain boundary diffusion", *J. Appl. Phys.* **94** (2003) 948-957.
66. P. Chaudhari, "Grain growth and stress relief in thin films", *J. Vac. Sci. Technol.* **9** (1972) 520-522.
67. M. Moske and K. Samwer, "The origin of internal stresses in amorphous transition metal alloy films", *Z. Phys. B-Cond. Mater.* **77** (1989) 3-9.

-
68. J. W. Cahn, "Surface stress and the chemical equilibrium of small crystals-I. The case of the isotropic surface", *Acta Metall.* **28** (1980) 1333-1338.
69. R. C. Cammarata, "Surface and interface stress effects in thin films", *Prog. Surf. Sci.* **46** (1994) 1-38.
70. H. Ibach, "The role of surface stress in reconstruction, epitaxial growth and stabilization of mesoscopic structures", *Surf. Sci. Rep.* **29** (1997) 193-263.
71. U. Geyer, U. von Hülse and H. Kopt, "Internal interfaces and intrinsic stress in thin amorphous Cu-Ti and Co-Tb films", *J. Appl. Phys.* **83** (1998) 3065-3070.
72. G. E. Dieter, *Mechanical Metallurgy*, McGraw-Hill, Boston, USA, 1986.
73. T. H. Courtney, *Mechanical Behaviour of Materials*, McGraw-Hill, Boston, USA, 2000.
74. L. H. Van Vlack, *Elements of Materials Science and Engineering*, Addison-Wesley Pub. Co., MA, USA, 1985.
75. S. H. Avner, *Introduction to Physical Metallurgy*, McGraw-Hill, New York, USA, 1974.
76. N. P. Kovalenko, Y. P. Krasny and U. Krey, *Physics of Amorphous Metals*, Wiley-VCH, Berlin, Germany, 2001.

-
77. D. Srolovitz, V. Vitek and T. Egami, "An atomistic study of deformation of amorphous metals", *Acta Metall.* **31** (1983) 335-352.
78. H. Mizubayashi, T. Okamoto, K. Koyama and M. Horiuchi, "Dynamic anelastic response of amorphous alloys suggesting collective motions of many atoms", *Acta Mater.* **46** (1998) 1257-1264.
79. H. Mizubayashi, T. Usui and M. Tanimoto, "Anomalous elastic response of amorphous alloys suggesting collective motions of many atoms", *Mater. Sci. Eng. A* **370** (2004) 260-263.
80. A. Inoue, "Stabilization of metallic supercooled liquid and bulk amorphous alloys", *Acta Mater.* **48** (2000) 279-306.
81. A. Inoue, "Preparation and novel properties of nanocrystalline and nanoquasicrystalline alloys", *Nanostruct. Mater.* **6** (1995) 53-64.
82. R. B. Schwartz and W. L. Johnson, "Formation of an amorphous alloy by solid-state reaction of the pure polycrystalline metals", *Phys. Rev. Lett.* **51** (1983) 415-418.
83. K. Samwer, "Amorphization in solid metallic systems", *Phys. Rep.* **161** (1988) 1-41.
84. S. H. Whang, "New prediction of glass-forming ability in binary alloys using a temperature-composition map", *Mater. Sci. Eng.* **57** (1983) 87-95.

-
85. S. H. Whang, "Glass forming ability for binary alloy systems by modified T-C map in relation to phase diagram", *J. Non-Cryst. Solids* **61 & 62** (1984) 841-846.
86. S. H. Liou and C. L. Chien, "Composition range of binary amorphous alloys", *Phys. Rev. B* **35** (1987) 2443-2447.
87. G. J. Van der Kolk, A. R. Miedema and A. K. Niessen, "On the composition range of amorphous binary transition metal alloys", *J. Less-Common Met.* **145** (1988) 1-17.
88. W. Hume-Rothery and H. M. Powell, "On the theory of super-lattice structures in alloys", *Z. Krist.* **91** (1935) 23-47.
89. A. K. Niessen, F. R. de Boer, R. Boom, P. F. de Chatel, W. C. M. Mattens and A. R. Miedema, "Model predictions for the enthalpy of formation of transition metal alloys", *CALPHAD* **7** (1983) 51-70.
90. M. Marcus and D. Turnbull, "On the correlation between glass-forming tendency and liquidus temperature in metallic alloys", *Mater. Sci. Eng.* **23** (1976) 211-214.
91. R. Coehoorn, G. J. Van der Kolk, J. J. Van der Broek, T. Minemura and A. R. Miedema, "Thermodynamics of the stability of amorphous alloys of two transition metals", *J. Less-Common Met.* **140** (1988) 307-316.
92. N. Saunders and A. P. Miodownik, "The use of free energy vs composition curves in the prediction of phase formation in codeposited alloy thin films", *CALPHAD* **9** (1985) 283-290.

-
93. N. Saunders and A. P. Miodownik, "Thermodynamic aspects of amorphous phase formation", *J. Mater. Res.* **1** (1986) 38-45.
94. R. Bormann, F. Gartner, K. Zoltzer and R. Busch, "Application of the CALPHAD method for the prediction of amorphous phase formation ", *J. Less-Common Met.* **145** (1988) 19-29.
95. J. M. Lopez, J. L. Alonso and L. J. Gallego, "Determination of the glass-forming concentration range in binary alloys from a semiempirical theory: application to zr-based alloys", *Phys. Rev. B* **36** (1987) 3716-3722.
96. K. Zuo, S. Xia and J. Zhuo, "Structure evolution and thermodynamics analysis of MoSi₂ during mechanical alloying ", *Mater. Sci. Eng. A* **445-446** (2007) 48-53.
97. A. W. Weeber, "Application of the Miedema model to formation enthalpies and crystallisation temperatures of amorphous alloys", *J. Phys. F: Met. Phys.* **17** (1987) 809-813.
98. A. R. Miedema, F. R. de Boer and R. Boom, "Model predictions for the enthalpy of formation of transition metal alloys", *CALPHAD* **1** (1977) 341-359.
99. A. K. Niessen and A. R. Miedema, "Enthalpies of formation of liquid and solid binary alloys based on 3d metals ", *Physica B* **151** (1988) 401-432.

-
100. A. C. Dunham and F. C. F. Wilkinson, "Accuracy, precision and detection limits of energy-dispersive electron-microprobe analyses of silicates", *X-Ray Spectrom.* **7** (1978) 50-56.
101. A. D. Romig, M. T. Dugger and J. P. McWhorter, "Materials issues in microelectromechanical devices: science, engineering, manufacturability and reliability", *Acta Mater.* **51** (2003) 5837-5866.
102. K. S. Birdi, *Scanning Probe Microscopes: Applications in Science and Technology*, CRC Press, UK, 2003.
103. Y. Iijima and T. Tazawa, "Application of total reflection X-ray photoelectron spectroscopy to boron and phosphorus on Si wafer surface measurement", *Spectrochim. Acta B* **59** (2004) 1273-1276.
104. W. C. Oliver and G. M. Pharr, "Measurement of hardness and elastic modulus by instrumented indentation: Advances in understanding and refinements to methodology", *J. Mater. Res.* **19** (2004) 3-20.
105. H. P. Klug and L. E. Alexander, *X-ray Diffraction Procedures for Polycrystalline and Amorphous Materials*, John Wiley & Sons, New York, USA, 2nd Edition, 1974.
106. M. Birkhloz, P. F. Fewater and C. Genzel, *Thin Film Analysis by X-Ray Scattering*, Wiley-VCH, Germany, 2006.

-
107. K. B. Yoder, A. A. Elmustafa, J. C. Lin, R. A. Hoffman and D. S. Stone, "Activation analysis of deformation in evaporated molybdenum thin films", *J. Phys. D* **36** (2003) 884-895.
108. A. R. H. Goodwin, E. P. Donzier and O. enberghe, "A Vibrating Edge Supported Plate, Fabricated by the Methods of Micro Electro Mechanical System for the Simultaneous Measurement of Density and Viscosity: Results for Methylbenzene and Octane at Temperatures between (323 and 423) K and Pressures in the Range (0.1 to 68) MPa", *J. Chem. Eng. Data* **51** (2006) 190-208.
109. J. F. Johnson, J. R. Martin and R. S. Porter, *Physical Methods of Chemistry, Part VI*, Eds.: A. L. Weissberger and B. W. Rossiter, Interscience, New York, USA, 1977.
110. W. Wagner¹ and R. Kleinrahm, "Densimeters for very accurate density measurements of fluids over large ranges of temperature, pressure, and density", *Metrologia* **41** (2004) S24-S39.
111. N. Kuramoto, K. Fujii and A. Waseda, "Accurate density measurements of reference liquids by a magnetic suspension balance", *Metrologia* **41** (2004) S84-S94.
112. A. L. Romoscanu, M. B. Sayir, K. Hausler and C. Servais, "High-frequency probe for the measurement of the complex viscosity of liquids", *Meas. Sci. Technol.* **14** (2003) 451-462.
113. B. A. Martin, S. W. Wenzel and R. M. White, "Viscosity and density sensing with ultrasonic plate waves", *Sens. Actuators A* 21-23 (1990) 704-708.

-
114. K. K. Li, A. Schneider and R. L. Abraham, "Instrument for the remote determination of viscosity and density in hostile environments", *Rev. Sci. Instrum.* **63** (1992) 4192-4195.
115. J. G. Woodward, "A vibrating plates viscometer", *J. Acoust. Soc. Am.* **25** (1953) 147-151.
116. M. K. Andrews, P. D. Harris, "Damping and a gas viscosity measurements using a microstructure", *Sens. Actuators A* **49** (1995) 103-108.
117. S. J. Martin, M. A. Butler, J. J. Spates, M. A. Mitchell and W. K. Schubert, "Flexural plate wave resonator excited with Lorentz forces", *J. Appl. Phys.* **83** (1998) 4589-4601.
118. S. Weigert, M. Dreier and M. Hegner, "Frequency shifts of cantilevers vibrating in various media", *Appl. Phys. Lett.* **69** (1996) 2834-2836.
119. P. L. Oden, G. Y. Chen, R. A. Steele, R. J. Warmack and T. Thundat, "Viscous drag measurements utilizing microfabricated cantilevers", *Appl. Phys. Lett.* **68** (1996) 3814-3816.
120. S. Kirstein, M. Mertesdorf and M. Schonhoff, "The influence of a viscous fluid on the vibration dynamics of scanning near-field optical microscopy fiber probes and atomic force microscopy cantilevers", *J. Appl. Phys.* **84** (1998) 1782-1790.

-
121. N. Ahmed, D. F. Nino and V. T. Moy, "Measurement of solution viscosity by atomic force microscopy", *Rev. Sci. Instrum.* **72** (2001) 2731-2734.
122. A. Maali, C. Hurth, R. Boisgard, C. Jai, T. Cohen-Bouhacina and J. P. Aime, "Hydrodynamics of oscillating atomic force microscopy cantilevers in viscous fluids", *J. Appl. Phys.* **97** (2005) 074907-1, 074907-6.
123. Y. Su, A. G. R. Evans and A. Brunnschweiler, "Micromachined silicon cantilever paddles with piezoresistive readout for flow sensing", *J. Micromech. Microeng.* **6** (1996) 69-72.
124. C. W. Baek, Y. K. Kim, Y. Ahn and Y. H. Kim, "Measurement of the mechanical properties of electroplated gold thin films using micromachined beam structures. *Sens. Actuators A* **117** (2005) 17-27.
125. L. Klesewetter, J. M. Zhang, D. Houdeau and A. Steckenbom, "Determination of Young's moduli of micromechanical thin films using the resonance method", *Sens. Actuators A* **35** (1992) 153-159.
126. M. K. Baller, H. P. Lang, J. Fritz, C. Gerber, J. K. Gimzewski, U. Drechsler, H. Rothuizen, M. Despont, P. Vettiger, F. M. Battiston, J. P. Ramseyer, P. Fornaro, E. Meyer and H. J. Guntherodt, "A cantilever array-based artificial nose", *Ultramicroscopy* **82** (2000) 1-9.

-
127. B. Rogers, L. Manning, M. Jones, T. Sulchek, K. Murray, B. Beneschott, J. D. Adams, H. Cavazos and S. C. Minne, "Mercury vapour detection with a self-sensing, resonating piezoelectric cantilever", *Rev. Sci. Instrum.* **74** (2003) 4899-4901.
128. A. M. Moulin, S. J. O'Shea and M. E. Welland, "Microcantilever-based biosensors", *Ultramicroscopy* **82** (2000) 23-31.
129. R. Raiteri, M. Grattarola, H. J. Butt and P. Skladal, "Micromechanical cantilever-based biosensors", *Sens. Actuators B* **79** (2001) 115-126.
130. N. Jalili and K. A. Laxminarayana, "A review of atomic force microscopy imaging systems: application to molecular metrology and biological sciences", *Mechatronics* **14** (2004) 907-945.
131. C. Hagleitner, A. Hierlemann, D. Lange, A. Kummer, N. Kerness, O. Brand and H. Baltes, "Smart single-chip gas sensor microsystem", *Nature* **414** (2001) 293-296.
132. M. Godin, V. Tabard-Cossa, P. Grutter and P. Williams, "Quantitative surface stress measurements using a microcantilever", *Appl. Phys. Lett.* **79** (2001) 551-553.
133. J. E. Sader, "Surface stress induced deflections of cantilever plates with applications to the atomic force microscope: rectangular plates", *J. Appl. Phys.* **89** (2001) 2911-2921.
134. J. Shieh, J. E. Huber, N. Fleck and M. F. Ashby, "The selection of sensors", *Prog. Mater. Sci.* **46** (2001) 461-504.

-
135. J. W. Judy, "Microelectromechanical systems (MEMS): fabrication, design and applications", *Smart Mater. Struct.* **10** (2001) 1115-1134.
136. M. R. Werner and W. R. Fahrner, "Review on materials, microsensors, systems, and devices for high-temperature and harsh-environment applications", *IEEE Trans. Ind. Electr.* **48** (2001) 249-257.
137. E. Donzier, O. Lefort, S. Spirkovitch and F. Baillieu, "Integrated magnetic field sensor", *Sens. Actuators A* **25-27** (1991) 357-361.
138. U. S. Lindholm, D. D. Kana, W. H. Chu and H. N. Abramson, "Elastic vibrations characteristics of cantilever plates in water", *J. Ship Res.* **9** (1965) 11-36.
139. J. E. Sadar, "Frequency response of cantilever beams immersed in viscous fluids with applications to the atomic force microscope", *J. Appl. Phys.* **84**(1998) 64-76.
140. T. P. Chang and M. F. Liu, "On the natural frequency of a rectangular isotropic plate in contact with fluid", *J. Sound Vib.* **236** (2000) 547-553.
141. D. W. Dareinga, T. Thundat, S. Jeon and M. Nicholson, "Modal analysis of microcantilever sensors with environmental damping", *J. Appl. Phys.* **97** (2005) 084902
142. J. W. M. Chon, P. Mulvaney and J. E. Sadar, "Experimental validation of theoretical models for the frequency response of atomic force microscope cantilever beams immersed in fluids", *J. Appl. Phys.* **87** (2000) 3978-3988.

143. E. Cumberbatch and G. Wilks, "An analysis of a vibrating element densitometer", *Math. Eng. Ind.* **1** (1987) 47-66.

144. M. K. Jain and C. A. Grimes, "Effect of surface roughness on liquid property measurements using mechanically oscillating sensors", *Sens. Actuators A* **100** (2002) 63-69.

145 Nanofab, *Nanofab Rates*, URL: <http://www.nanofab.ualberta.ca>, accessed July 2007, University of Alberta, Edmonton, Canada.